UNIVERSITÀ
DI PAVIA

SCUOLA DI ALTA FORMAZIONE DOTTORALE

MACRO-AREA SCIENZE E TECNOLOGIE

Dottorato di Ricerca in Scienze della Terra e dell'ambiente

Simone Zana

A versatile workflow for building 3D hydrogeological models combining subsurface and groundwater flow modelling: a case study from southern Sardinia (Italy)

Anno Accademico 2024-2025

Ciclo 37

Coordinatore

Prof. Andrea Mondoni

Supervisore

Matteo Maino

Co-supervisore

Dott. Fabio Canova

Table of contents

Abstract

This research project aims to develop a basin-scaled 3D numerical groundwater flow model developed with “ModelMuse” using as base a 3D hydrogeological model developed with Petrel E&P (Petrel 2021©). A relevant and innovative aspect of the project is the use of Petrel 2021© geological modelling tools in the field of applied hydrogeology to improve the details of both hydrogeological and numerical groundwater flow models, and their predictive capabilities. The study area is located in South Sardinia (Campidano Plain), where previous hydrogeological and modelling studies were available. The hydrogeological model was developed by digitalising and interpreting the facies in the available borehole logs. A 3D grid was subsequently created, including the main hydrogeological surfaces and performing geostatistical modelling of the borehole log facies and hydraulic conductivity based on grain size percentages. These groundwater flow model simulations, under various groundwater head scenarios, established the boundary conditions and conductivity values needed to determine the hydrogeological balance of the study area. The probabilistic approach has produced a highly detailed model able to adequately represent the natural hydrogeological phenomena and the anthropic stresses in places in the underground.

Scope of Work

The aim of the research project is to develop a 3D numerical groundwater flow model at the basin scale using the software 'Petrel E&P' to develop the hydrogeological model and 'ModelMuse' to develop a numerical flow model. This model allows to quantify the hydrogeological balance and manage water withdrawals. An innovative aspect of the project is the environmental use of numerical tools developed in the E&P field, to improve the detail of hydro-stratigraphic models and numerical groundwater flow models, thus improving their predictive capabilities. The study area is in the south of Sardinia (Campidano plain), where there were already 5 sites of interest and subject to previous hydrogeological and modelling studies. The work was developed by following these steps i) digitalization and interpretation of facies in the available stratigraphic logs; ii) creation of a 3D grid including the main hydro-stratigraphic surfaces and geostatistical simulation (facies, hydraulic conductivity) iii) creation of numerical flow model and calibration simulation to assess boundary condition; iv) particle tracking simulation.

1. Introduction

Shallow clastic granular sediments overlying the bedrock host key groundwater resources. Urban concentration and industrial clusters lead to an increasing pressure on these aquifers in terms of both abstraction and environmental alteration (Cidu et al., 2009; Lee et al., 2010; Biddau and Cidu, 2016; Tiwari et al., 2019; Li et al., 2021). Groundwater resource management needs to be assessed from a quantitative perspective using numerical flow models. The use of groundwater modelling has become prevalent in the field of environmental sciences where all stakeholders (e.g. academic and research organizations, public administration, Industry and Farming) aim to streamline the use of aquifer resources (Kinzelbach, 1986; Chiang, 2005; Barazzuoli et al., 2008; Singh, 2014; Ghiglieri et al., 2016). However, these clastic aquifers often show intricate three-dimensional combination of interlayered gravel, sand, silt and clay, resulting in heterogeneous and anisotropic hydraulic properties (e.g. hydraulic conductivity, k) becoming difficult to predict (Smaoui et al.,2012; Lal and Datta, 2020). Therefore, stratigraphic characterisation is necessary to implement realistic numerical groundwater flow modelling in natural settings and to allow sustainable exploitation of water resources (Hudon-Gagnon et al., 2015; Mukherjee et al., 2007; El-Azhari et al., 2024; Chicco and Mandrone, 2022; Chicco et al., 2023). However, the construction of 3D hydrogeological models for clastic aquifers remainsbecause of the difficulty of collecting large amounts of hydrostratigraphic information (Wu et al., 2011) despite their significant development advances in recent years. Two primary approaches have been traditionally used for developing conceptual models: (i) the consensus model approach (Brassington et al., 2010; Enemark et al., 2019) and (ii) the multi-model approach

(Enemark et al., 2019; Neuman and Wierenga, 2003). The construction of conceptual models depends on available geological and hydrogeological data such as field observations (Klingbeil et al., 1999; Weissmann et al., 1999), geophysics (Heinz and Aigner, 2003; Pugin et al., 2014), borehole analysis and the definition of a depositional model providing a conceptual architecture of the sedimentary stratigraphic system (Ghiglieri et al., 2016; Di Salvo et al., 2012; Irace et al., 2010). In case of scarce data availability, the multi-model approach represents the best solution, since it can interpret the hydrogeological functioning of the aquifer system in different ways (Enemark et al., 2019; Neuman and Wierenga, 2003; Anderson et al., 2015; Beven, 2002; Refsgaard et al., 2006). However, in recent years, the use of probabilistic approaches has significantly increased in the field of hydrogeological modelling, particularly when data are sparsely distributed in the study area (Madsen et al., 2022; Barfod et al., 2018; Gong et al., 2021; Madsen et al., 2021; Stafleu et al., 2011; Vilhelmsen et al., 2019; Zhao et al., 2021).

In this thesis, the case study presented, Capoterra Plain, Sardinia, Italy, is focused on a coastal aquifer, made up of marine and alluvial sediments. Groundwater management is demanded to numerical flow models, the usefulness of which strongly depends on the accuracy of hydrogeological information (Mackay et al., 1985; Macdonald et al., 2005). The project development approach began with the analysis of all available data within the regional geological context to define the stratigraphic framework. This served as the foundation for a 3D hydrogeological model, constructed through geostatistical modeling and implemented using Petrel©. Subsequently, numerical flow models were developed using ModelMuse. The choice of ModelMuse, in combination with Petrel, was driven by their compatibility in grid structure and indexing. The innovative aspect of this project lies in applying numerical tools initially developed for the exploration and production (E&P) field to environmental studies. The hydrogeological model developed with Petrel overcomes limitations common in other modeling software, especially in representing grain size and hydraulic conductivity distributions. Traditional models often assume homogeneous grain size facies and hydraulic conductivity, which can lead to oversimplifications. In contrast, Petrel's algorithms enable the reconstruction of a detailed hydrogeological model that maintains heterogeneous distributions of grain size and hydraulic conductivity, derived from borehole data at specific depths. This approach results in a more accurate hydrogeological model that better reflects the complexity of the aquifer system. The probabilistic approach used to populate this hydrogeological model offers a more accurate representation of the aquifer system than deterministic methods. By incorporating hydrogeological parameters into the model, this probabilistic method captures the aquifer's natural variability in parameters like grain size and hydraulic conductivity distributions. Consequently, the model better reflects the aquifer system's

heterogeneity, providing a more reliable and comprehensive understanding of subsurface conditions than a purely deterministic approach, which may oversimplify these complexities.

2. Geological and geographical settings

The Campidano Plain is the largest flat area in the Sardinia region. Geologically, it is a graben with an NNW-SSE trend, stretching from the Oristano Gulf to the Cagliari Gulf (around 100 km in length and approximately 20 km in width). The highest elevations within the Campidano Plain are found in the Sulcis-Inglesiente-Arburese block in the western part, where altitudes exceed 1,000 meters, while the eastern part features hills reaching up to 400 meters.

The Campidano Graben underwent the most important geodynamic evolution of Sardinia during Plio-Pleistocene time.

Since the nineteenth century this area has been recognised as a tectonic trough (Lamarmora, 1857). While geomorphological and stratigraphical studies, conducted by numerous authors, generally agree that the Campidano trough is of recent origin (Moretti, 1953; Pomesano Cherchi, 1967; Maxia et al., 1970), other authors have suggested that the Campidano syncline was modelled before the Permian succession (Cavinato, 1939). Thanks to the presence of several wells drilled for hydrocarbon exploration (reaching depths of about 2000 m) and hydrogeological research, it has been possible to obtain data regarding the subsurface stratigraphy of the Campidano graben. Various papers have described this stratigraphic information (Pecorini and Pomesano Cherchi, 1969; Cherchi and Murru, 1985; Frau, 1994).

The hydrology of the area is dominated by streams flowing through the northeastern and western sectors. The main rivers are the Flumini Mannu, Rio Santa Lucia, Rio Cixerri and Rio San Gerolamo. While Flumini Mannu is the main watercourse, with a catchment area of 593 km², draining into the Pond of Santa Gilla, Rio Santa Lucia originates from the western reliefs near Capoterra and flows into the Pond of Capoterra, with a watershed basin of 104 km². Rio Cixerri instead, originates from the southern area of Iglesias and extends for 40 km in an east-west direction, draining into the Pond of Santa Gilla. A dam constructed near Genna Is Abis along its course resulted in the creation of Cixerri Lake. On the other hand, Rio San Gerolamo drains a smaller area of 27 km². Both Rio Santa Lucia, Rio Cixerri and Rio San Gerolamo are characterized by a torrential nature, exhibiting strong seasonal variations.

2.1 Climate settings

The climate is Mediterranean, characterized by mild and humid winters and hot and dry summers.

Average rainfall data from 2018 to 2022, recorded by six weather stations located within the study area (Figure 1) were analysed, and a good correlation among the different weather stations' months was found (Figure 2), with some difference in average rainfall values, especially during rainy months, mainly due to different weather stations' elevations. In fact, Uta Santa Lucia and Capoterra Poggio dei Pini are located on the mountain part of the area and show higher average rainfall values with respect to the weather station located in the flood plain.

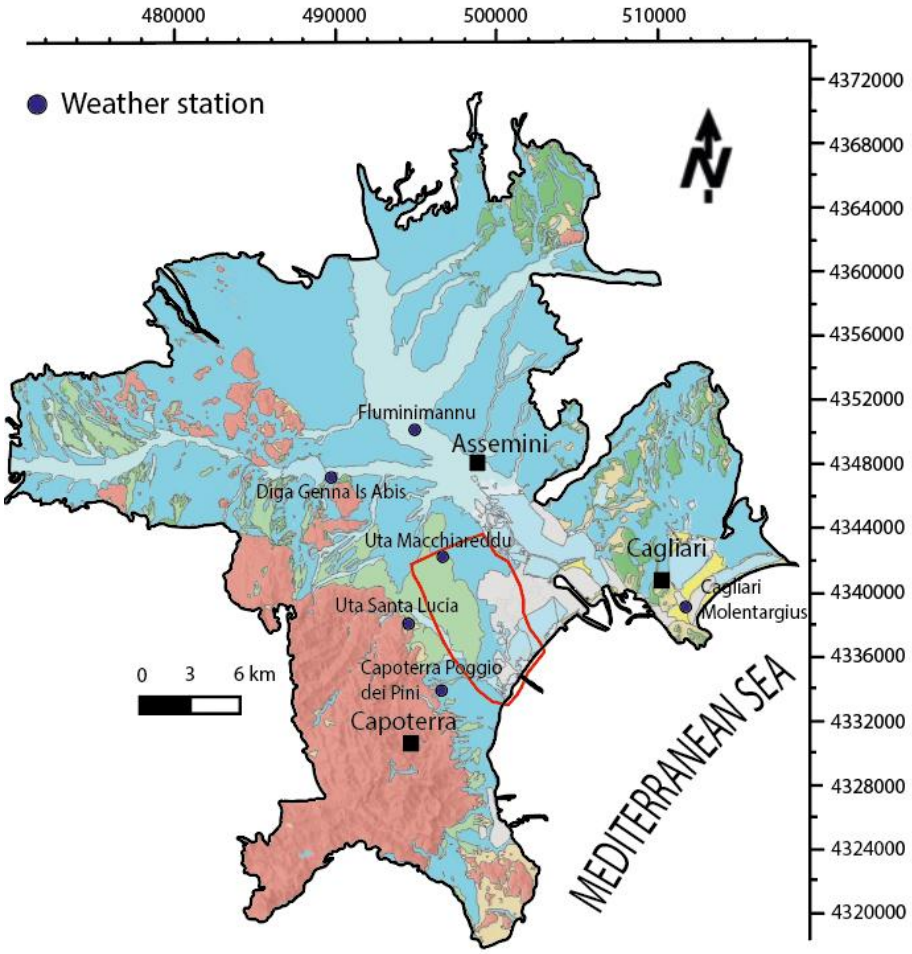

Figure 1. Weather stations distribution in the study area (image obtained from the database Arpas weather department).

Autumn is the wettest time of the year, with November, recording the highest rainfall values, whilst July turned out to be driest.

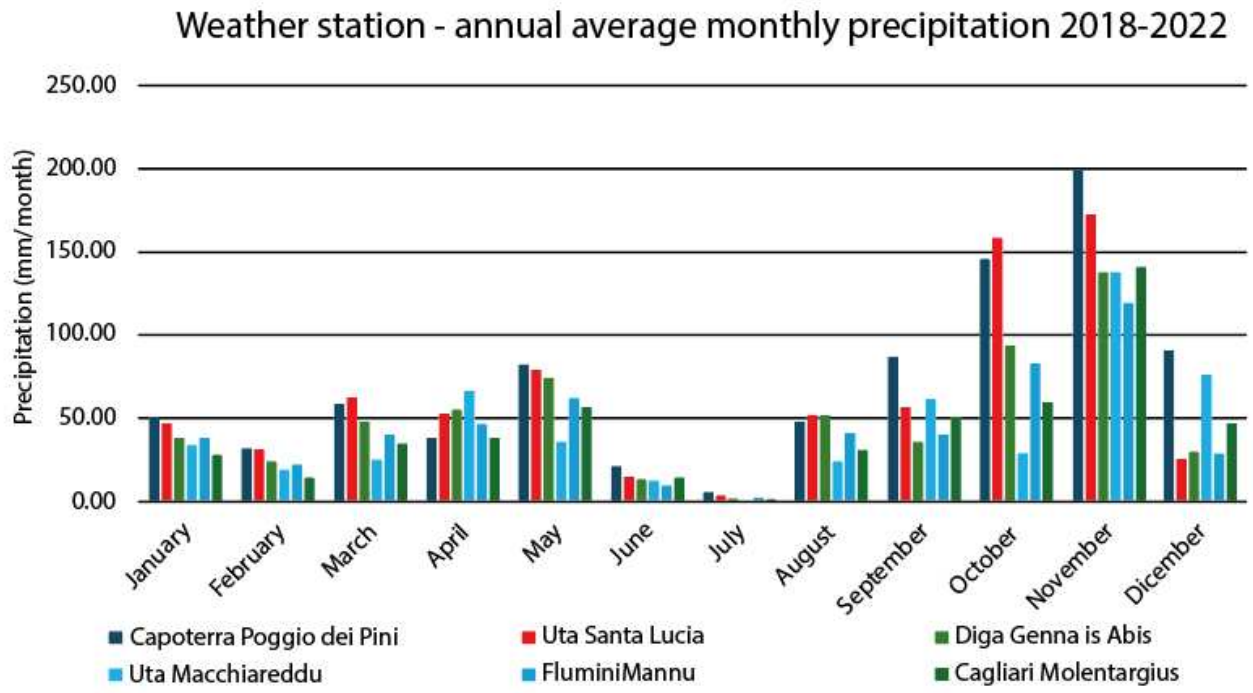

Figure 2 - The graph shows average annual precipitation for the period from 2018 to 2022 (data taken from Arpas website - https://dati-annuali-rete-arpas-2021-arpas.hub.arcgis.com)

Average monthly temperatures and rainfall data are inversely related (figure 3): during summer highest temperature and lowest precipitations are recorded, especially in August, where the temperature reached its maximum. The lowest average temperature is recorded in January, however this does not correspond to the wettest period of the year, which is November, when temperatures are slightly higher.

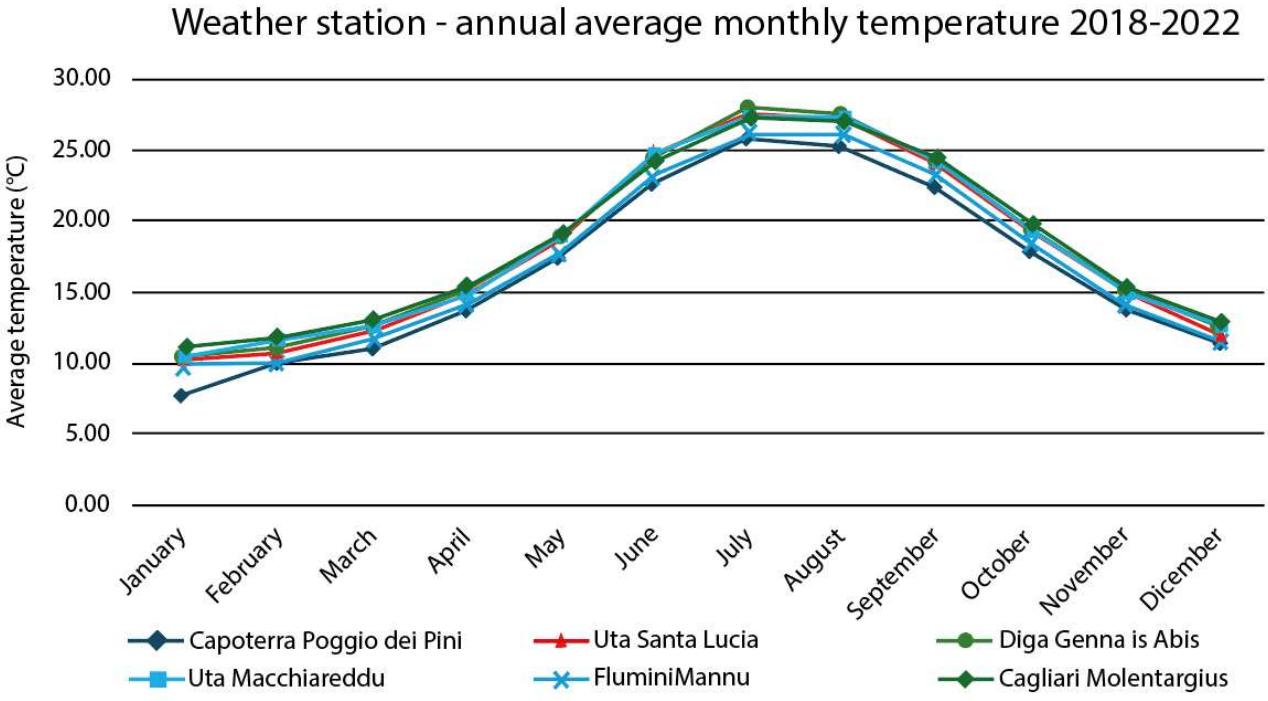

Figure 3 - The graph shows average annual temperature for the period from 2018 to 2022 (data taken from Arpas website - https://dati-annuali-rete-arpas-2021-arpas.hub.arcgis.com)

2.2 Regional geological Setting

The rocks of Sardinia preserve a record of the island's geological evolution throughout the entire Phanerozoic eon (Arthaud & Matte, 1977; Matte, 1981; Carmignani et al., 2001; 2004; 2016; von Raumer & Stampfli, 2003; 2008). Born as a passive margin of the Gondwana continent, Sardinia records the opening of the Rheic ocean, followed by the Variscan orogeny and the reorganisation of Pangea up until the Permian period (Cassinis et al., 2003; Di Vincenzo et al., 2004; Gaggero et al., 2017; Ronchi et al., 2008; Casini et al., 2010; 2012; 2013; 2015; Carosi et al., 2012; Cocco et al., 2018). During the Mesozoic, the islands primarily acted as a passive margin of the Tethys Ocean and was marginally involved in the Alpine orogenic phase (Stori et al., 2023). The post-Alpine evolution is marked by the opening of the Liguro-Provençal and Thyrrenian basins (Oligocene-Miocene), driving the drift of the Corsica-Sardinia block from the European margin to the present-day location (Alvarez, 1972; Cherchi & Montadert, 1982; Carmignani et al., 1994; 1995; 2001; 2004; Funedda et al., 2000; Speranza et al., 2002; Oggiano et al., 2009).

The geology of the Sardinia region is briefly described in this paragraph. Based on bibliographic data, general geological features and different tectonic events have affected this region. Based on that premise, the island's geology can be divided into three main geological units:

- Palaeozoic metamorphic basement (Precambrian - Lower Carboniferous);
- Variscan batholith (upper Carboniferous - Permian);
- Post-Variscan covers (upper Carboniferous - Quaternary).

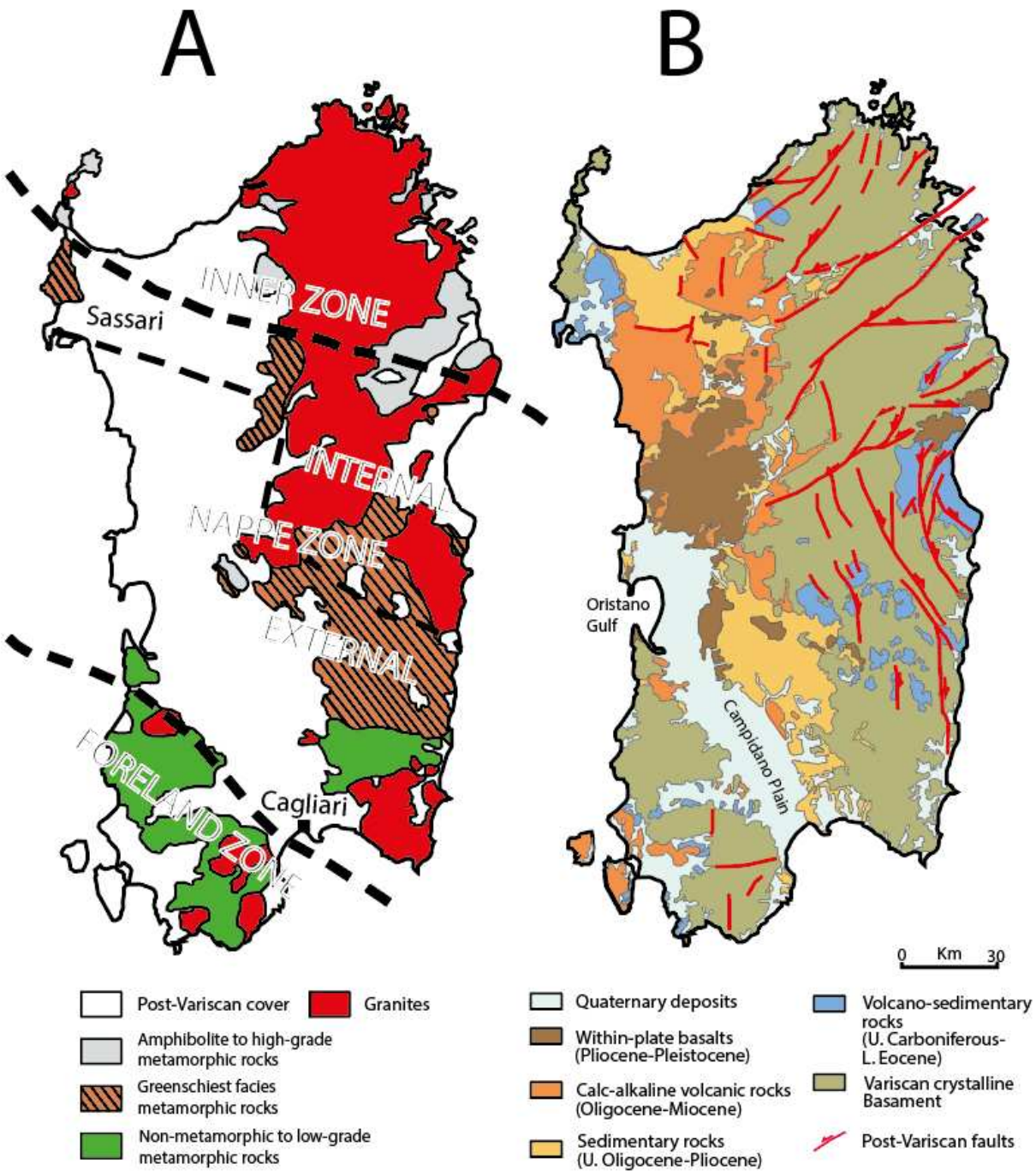

Figure 4. A) Tectono-metamorphic zones of Sardinia region, where the geometry of the Variscan belt shows a decrease in metamorphism and a deformation from north to south, leading to the definition of three distinct structural zones: Inner zone, Nappe zone and Foreland zone (modified by Cocco et al., 2018). B) Geological sketch map of the main geological units and post-variscan features in Sardinia (modified from Oggiano et al., 2009)

2.2.1 Palaeozoic metamorphic basement

The origins of the Variscan orogenic belt are linked to the collision between Laurussia and Gondwana, which occurred between 480 and 250 Ma (Rossi et al., 2009). Most authors agree that the Variscan orogeny evolved through the subduction of oceanic crust and the development of high-pressure conditions during the Silurian, followed by continental collision during the Devonian and early Carboniferous (Carmignani et al., 1994; Rossi et al., 2009).

The geometry of the Variscan belt in Sardinia shows a decrease in metamorphism and deformation from north to south, leading to the definition of three distinct structural zones (Carmignani et al., 1994; figure 4A):

- **Inner zone**: located in the northern part of the island, this zone is characterized by medium- to high-grade metamorphic rocks intruded by late Variscan granites. The Inner zone and the Nappe zone are separated by the Posada-Asinara line, where relics of oceanic crust, such as eclogite and basalts, crop out (Cappelli et al., 1992).
- **Nappe zone**: situated in the southeast and central parts of the island, this zone is affected by greenschist facies metamorphism (Edel et al., 2014) and includes a thick continental arc-related volcanic suite of Middle Ordovician age (Gaggero et al., 2012), interbedded within a thick Palaeozoic metasedimentary succession. Furthermore, this zone is divided into two subzones: the Internal Nappe Zone (central-northern Sardinia), characterised mainly by medium-grade metamorphic rocks, and the External Nappe zone (central-northern Sardinia), characterized by low-grade metamorphic rocks.
- **External Zone**: located in the southwestern part of Sardinia, this zone consists of an unmetamorphosed fold- and thrust- belt (Funedda 2009).

2.2.2 Variscan batholith

The Variscan batholith refers to the granite formations found in Sardinia and Corsica. The Corsica-Sardinia Batholith (C-SB, Orsini, 1976; Rossi and Cocherie, 1991) originated during the late Carboniferous-Permian, can be associated to geothermal uplift, which induced partial melting of the crust and mantle.

The study of the field relationship, U-Pb zircon dating, and petrologic analyses allowed for the subdivision of the C-SB into three magmatic suites (Casini et al., 2015; Rossi and Cocherie, 1991; Ferré and Leake, 2001):

- **U1**: developed in northern Corsica around 340 Ma (Paquette et al., 2003) during N-S shortening. This suite is a calc-alkaline suite (high K/Mg content) and consists of diorites and mafic rocks;
- **U2**: comprising the largest portion of the C-BS (del Moro et al., 1975; Ferré and Leake, 2001), this suite originated between 320-280 Ma, is characterized by a decrease in MgO content within the granitic melts;
- **U3**: represents the last magmatic phase of the C-SB (300-280 ma) and includes post-orogenic plutons emplaced at very shallow structural levels and sub-volcanic complexes, which doesn't crop out in Sardinia (Cocherie et al., 2005).

2.2.3 Post Variscan covers

Despite its location between two orogenic belts (the Pyrenees to the west and the Apennines to the east) and later being bounded by the opening of the Balearic Basin to the west and the Tyrrhenian Basin to the east, the post-Variscan evolution of Sardinia, has always seen the Island acting as a stable block. The region was exposed to transgressions and regressions but was not subject to major tectonic events.

During the Mesozoic era, Sardinia didn't undergo significant tectonic or magmatic activity. Despite the transgressions in the Triassic and Lower Jurassic, Sardinia remained a structural high. In the middle Jurassic (Dogger), the island was subjected to a transgression process, resulting in an unconformable deposition of dolomite and limestone above the Palaeozoic Basement, late Palaeozoic continental deposits, and the Permo-Triassic succession. From the Late Cretaceous through most of the Paleocene, continental conditions persisted in Sardinia.

A new transgression phase occurred during the Lower Eocene, characterized by terrigenous to carbonate deposits with predominant macroforaminifera (Murru and Salvadori, 1990; Carmignani et alii, 2001a; 2001b). Afterwards, a new continental stage occurred during the Middle-Upper Eocene, marked by fluvial and lacustrine deposits, as observed in the Cixerri Formation (Pecorini and Pomesano Cherchi, 1969).

The structural setting of Sardinia during the Upper Oligocene and Lower Miocene is detailed in several works (Pasci, 1997; Oggiano et al., 2009). The northern part of the island is characterised by the presence of strike-slip faults associated with both transpressional and transtensional zones, where pull-apart basins are filled with continental deposits from Upper Oligocene-Aquitanian age, coupled with significant volcanic activity. Two main hypotheses explain this geodynamic evolution:

- According to the first one, it might be an extensional tectonic evolution beginning in the Upper Oligocene, due to the development of a tectonic trough that crossed Sardinia from the Gulf of Cagliari to the Gulf of Asinara (Cherchi and Montadert, 1982; 1984; Casula et al., 2001);
- the second hypothesis suggests that, during the Upper Oligocene-Lower Aquitanian, the Sardinia region functioned as the hinterland of the collision between the Southern European and Adria Margins, which gave rise to the Northern Apennines (Carmignani et al., 1995; Oggiano et al., 2009).

The Aquitanian basins are thus linked to the Apennine collisional evolution, whereas the later Burdigalian basins resulted from the counterclockwise rotation of the Sardinian-Corse block and the related opening of the Balearic basin. This period was also marked by significant volcanic activity, characterized by extensive and thick limestone deposits (Lecca et al., 1997).

During the Pliocene, Sardinia experienced another extensional event, likely associated with the opening of the southern Tyrrhenian basin. The most significant structure resulting from this geodynamic event is the Campidano Graben, extended from the Gulf of Cagliari and the Gulf of Oristano.

2.3 Local geological setting

The study area is covered by sheets No. 556-Assemini, 557-Cagliari, 565-Capoterra, and 566-Pula of the Geological Cartography Project (CARG) by ISPRA on a scale of 1:50,000. The area is characterised by extensive outcrops of Variscan metamorphic complexes and post-Variscan intrusive complexes, dating from the Precambrian-Lower Carboniferous to the Upper Carboniferous–Permian, which together form the Palaeozoic Basement. Additionally, Quaternary cover deposits are present (figure 5).

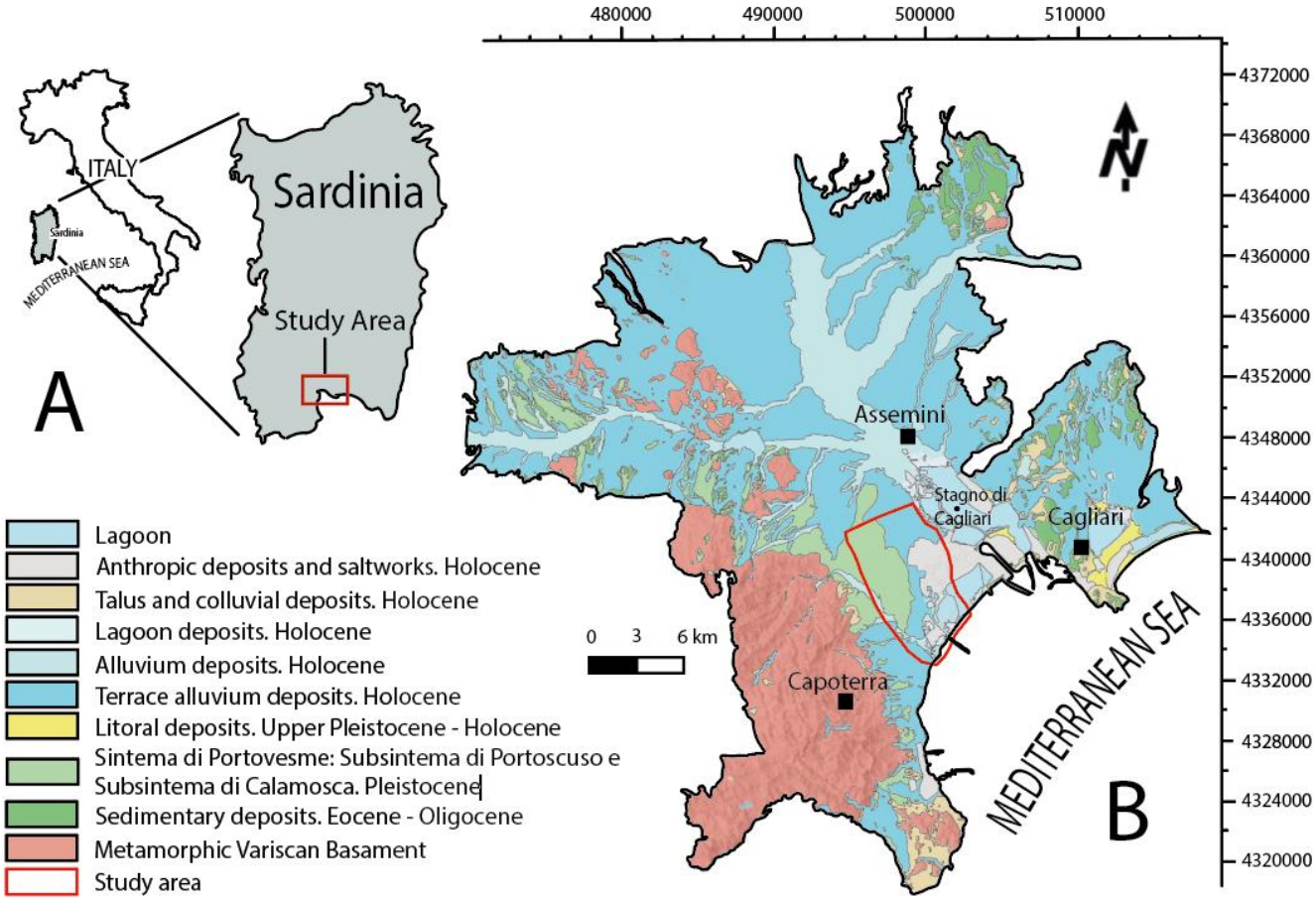

Figure 5. A) Geographical map of the study area; B) Geological map of the southern Campidano plain1. Campidano plain represents the largest flat area of the Sardinia region, where fluvial activity is the main sedimentary deposition system. The metamorphic basement crops out mainly into the mountain area, in the western part of figure. The region outlined by the red box is shown in further detail within Figure 2.

2.3.1 Palaeozoic basement

The **Variscan metamorphic complexes** represent part of the Palaeozoic basement and are represented by the External Nappe Zone and by the Inglesiente-Sulcis external zone.

The **External Nappe Zone** (Unità Tettonica dell'Arburese) outcrops at the northwestern extremity of the study area and is characterized by two formations:

- *Intermediate-acid Metavolcanics* are characterized by dikes of dark grey dacitic-ryodacitic metavolcanics with a porphyritic texture, which contain phenocrysts of plagioclase, quartz and biotite, often replaced by chlorite (Middle Ordovician);
- *San Vito Sandstones* are characterized by irregular alternation, on decametric to metric scales, of medium-fine metarenites, grey micaceous metasiltstones and metasiltstones with planar-parallel, undulating and cross-lamination. Moreover, intercalations of polymictic metamicroconglomerates with predominant sub-rounded quartz clasts and subordinate quartzites (Lower Cambrian-Ordovician) can be seen.

The **external zone of the Iglesiente-Sulcis** is divided by age. In the study area, the succession from the upper Ordovician to the lower Carboniferous post-Sardic unconformity crops out and it is subdivided into:

- *Terrigenous Succession* (lower Carboniferous). This unit crops out in the northwestern part of the study area with the Pala Manna Formation. It is characterized by metarenites, quartzites, rare chloritized basic metavolcanics, metavolcaniclastics, metarenites with volcaniclastic matrix, metasiltstones, and metasiltstones, some of which show traces of bioturbation and rare macroflora fossils (PMNa). It also includes polymictic metaconglomerates with chloritized basic metavolcanics (PMN3), banded quartzites (PMNb), metaepiclastics with scarce acidic metavolcanics in decimetric levels (PMNc), breccias and lidites (PMNd), and metaconglomerates with quartz clasts and metarenites (PMVe) (Lower Carboniferous).
- *Carbonate-Terrigenous Succession* (Silurian-lower Devonian). This succession includes the Mason Porcus Formation and by the Genna Muxerrusi Formation. The former is locally exposed in the western part of the study area, featuring deposits of dark grey metasiltstones, decarbonated fossiliferous marly metasiltstones (containing trilobites, crinoids, gastropods, etc.), and marly metasiltstones (MPSb). This formation also includes nodular and subordinate massive fossiliferous metacarbonates, as well a massive metacarbonates and/or those transformed into skarn (MPSa) (Silurian?-lower Devonian). The Genna Muwerrusi Formation crops out near the structural lineations west of the Capoterra plain. It is characterized by metapelites, metargillites, and black graphitic metasiltstones that are locally fossiliferous with graptolites, with intercalated levels of "lidites" (lower Silurian) (Barca et al., 2005).

The **Late Palaeozoic intrusive and dyke complexes** (upper Carboniferous – lower Permian) represent another part of the Palaeozoic basement and can be divided into:

- **The Permian Magmatic-Hydrothermal Dyke System**: this system is evidenced by the intrusion of acidic, intermediate-basic and hydrothermal dyke, predominantly quartz, within most of the Intrusive Unit (Permian);
- **The Leucomonzogranites at biotite of the Villacidro Intrusive Unit**: this unit crops out in the northwestern part of the study area. The leucomonzogranites are medium to medium-fine grained, pink, ranging from equigranular to moderately inequigranular, with an isotropic texture. The border lithofacies are porphyritic to microgranular, with frequent metric aplopegmatitic lenses (VLDb) (upper Carboniferous-lower Permian).
- **The Santa Barbara Intrusive Unit**: this unit is characterized by biotite and amphibole microgranodiorites, which crops out in the west part of the study area, in contact with the leucomonzogranites of the same formation. The microgranodiorites are coarse-grained, grey-pink, inequigranular with a porphyritic structure (SBBb). Intercalated outcrops microtonalitic masses, ranging from metric to hectometric, sometimes associated with xenoliths of metamorphic basement (SBBa) (upper Carboniferous-lower Permian).

2.3.2 Quaternary deposits

The official cartography does not provide a coherent interpretation of the chronostratigraphy of the various types of Quaternary deposits. In the Pula Sheet, the terraced alluviums are assigned to the Upper Pleistocene. On the contrary, in the Capoterra Sheet, Pleistocene deposits are limited to some isolated outcrops in the foothill areas, while Holocene terraced alluvial deposits predominate in the rest of the plain.

2.3.2.1 Pleistocene deposits

The *Sintema di Portovesme* is composed of marine and continental sediments deposited during the penultimate cold phase of the Pleistocene (Dansgards et al., 1993). The Sintema is delimited at the bottom by a transgression Tirrenian surfaces, with its type locality at Cala Mosca, where littoral deposits crop out (Barca et al., 2005).

The Sintema di Portovesme consists of two subsystems: the *Subsintema di Portoscuso* (PVM_2) which is composed of alluvial deposits and continental debris, and the *Subsintema di Calamosca* (PVM_1), characterized by marine sediments. Generally, between these two, a lower-order angular unconformity or paraconformity is present.

The subsintema di Calamosca crops out in the coastal part of the study area, particularly along the coast of S. Elia (Cala Mosca, Marina Piccola). Cala Mosca represents the type locality of the Tyrrhenian, for which the clastic succession was previously described by earlier authors (Ulzega et

al., 1981). In the western area of Cala Mosca, this sequence lies above a marine erosion platform, represented by cliff-foot and beach conglomerates. These conglomerates are composed of heterometric pebbles, variably worked, derived from Upper Miocene rocks, with subordinate quartz, rhyolitic porphyries, and Palaeozoic metamorphic rocks. The matrix is sandy, sometimes strongly cohesive or cemented, with a thickness ranging between 40 and 80 cm.

In the southern part of Cala Mosca, these deposits are found in the aerial part of a largely occluded cave, where near the base they seal borings made by lithophagid molluscs (Barca et al., 2005). In the upper part of the fill, the borings are sealed by detrital and aeolian-colluvial deposits.

In the easternmost part, along the shoreline, a sequence of beach sandstones with planar or low-angle bidirectional crossbedding is exposed, intercalated with gravels predominantly composed of Miocene limestones, with thicknesses up to 2 meters. Additionally, the coarse beach deposits are preserved under abundant colluvial covers in this area.

Similar deposits are also known at Marina Piccola (Ulzega and Ozer, 1982; Ulzega et al., 1980).

The subsintema di Portoscuso crops out in the coastal part of the study area, in contact with the Holocene deposits and the Palaeozoic basement. It is mainly composed of alluvial deposits and slope deposits. The alluvial deposits predominantly consist of coarse gravels and, more rarely, blocks with subrounded and subangular edges. These gravels form concave cross-bedded structures in some areas of the map, such as Poggio dei Pini and the Azienda Agricola Medda-Obino. The structures are generally flat and of limited amplitude; while fine sediments, such as sandy lenses or layers, are rare. The described alluvial deposits generally resemble to flattened alluvial fans, deposited by watercourses that have incised the Sulcis hills in the area between Capoterra and Pula. To the north, near the slopes, there is an increase in the clast size and the percentage of angular elements due to the quartz nature of the eroding material. While the total thickness can exceed ten metres, it is usually only a few meters. Rivers have led to the formation of escarpments and the erosion of terraces now located alongside the current riverbeds. In the piedmont area, transport processes dominate, dismantling and carrying debris from mountain slopes to the valley.

The detrital deposits are characterized by relatively coarse clasts with angular edges, arranged in both layers and decimetric lenses. These deposits formed at the base of slopes composed of basement rocks, resulting in debris fans and cones that were mostly eroded during postglacial downcutting (Barca et al., 2005, upper Pleistocene).

2.3.2.2 Holocene deposits

Holocene deposits are found in contact with upper Pleistocene deposits and exhibit different characteristics: terraced alluvial deposits, piedmont deposits, alluvial deposits, littoral deposits and anthropic deposits.

The terraced alluvial deposits are characterized by coarse materials with lenses and layers of sands and fine gravels, displaying either concave cross-bedding or massive structure. These deposits are similar to those observed along current riverbeds. They are located alongside the riverbed and are not affected by water flow except during exceptional events. Near the reliefs, valley floor sediments are connected to inclined alluvial fans, such as those souths of Capoterra. In these areas, some gravelly layers are matrix-supported. Rectilinear fluvial erosion scarps are also present in certain locations, indicating phases of valley downcutting followed by the aggradation of coarse sediments.

The Piedmont deposits are located to the east of Capoterra. The deposits, consisting of chaotic accumulation of angular clasts and more generally of limited thickness, are observed to be in contact to the summits of limestone reliefs and, less frequently, to Palaeozoic bedrock outcrops. The most plausible hypothesis is that all these detrital deposits were emplaced due to anthropogenic slope degradation during the protohistoric period, resulting from progressive deforestation practices for agriculture and livestock.

The alluvial deposits are composed of coarse to very coarse gravels with local intercalations of sandy lenses. The stratification varies from planar-parallel to very shallow concave crossbedding, indicating the dynamics of a braided channel system. A sinuous trace of the Riu Santa Lucia is still recognisable, extending towards the Capoterra salt pans, where the final path has recently been dammed to mitigate hydrogeological risk to the developments built along the edge of the Cagliari lagoon. The thickness of these alluvial sediments is highly variable, ranging from one metre to 3-4 meters. Within the channels, gravel deposits can also be very coarse, with cobble size generally larger in the upstream sections and tending to decrease downstream, where a local increase in fine matrix components is observed.

Littoral and coastal ridge deposits are found along the coast of the Gulf of Cagliari, bordering the promontory of S. Elia and the Lagoon of Santa Gilla. Littoral deposits consisting of medium-coarse sandy sediments near Poretto-Marina Piccola, usually become medium-fine along the coastline of the Plaia and in the Rada of Sant'Efisio. Littoral ridge deposits indicate rapid Holocene sedimentation, composed of materials altered from ancient alluvial and/or deltaic deposits by current watercourses (Bellotti, 2000; Pranzini, 2004). The origin of these deposits is associated with rapid Holocene progradation driven by the sedimentation of alluvial fans.

Anthropic deposits are composed of artificial landfill materials with geotechnical characteristics that vary significantly based on their composition, degree of compaction, period, and method of accumulation.

2.4 Hydrogeological setting

The Capoterra Plain is characterized by two-aquifer systems (Ardau et al., 1997; Barrocu et al., 2004; Sciabica, 1994; Barrocu et al., 2004): i) a shallow, phreatic aquifer, with a thickness of about 30 m (Balia et al., 2009); ii) and a multilayer aquifer, locally confined, with a thickness of about 100 m (Balia et al., 2009). The first aquifer is mainly represented by recent alluvium deposits (Holocene) and terraced alluvium, while the second aquifer system is hosted in alluvium (Quaternary) characterized by a highly variable permeability, resulting in variation in local hydraulic conductivity due to internal facies heterogeneity (Pala, 1983; Balia et al., 2009). In the easternmost part of the plain, a 10-25 m thick sandy-clayey lenticular layer separates these two aquifers (Pala, 1983). The bottom of the deepest aquifer, instead, is characterized by a clayey layer to the east, corresponding to the transition with Miocene deposits and by the crystalline basement to the west (Pala, 1983). The fractured granite complexes in the western part of the plain, adjacent to the hills, represent the main source of water recharge (Barrocu et al., 2004).

The hydraulic conductivity K of the phreatic aquifer was estimated by previous studies as falling in the range 1.58x10-4 – 2.11x10-4 m/s. The K range of the deeper aquifer was estimated between at 6.79x10-7 – 1.92x10-5 m/s (Barrocu et al., 1997; Sciabica, 1994; Pala, 1983).

According to hydrochemistry data, the two aquifers are interconnected in several areas, one of the main reasons possibly being bad completion of pumping wells (Balia et al., 2009). As a results, the groundwater of the two aquifers mix and consequently spreading of salinization phenomena is observed. Salinization problems are well known in the area (Barrocu et al. 1994; Barrocu et al., 2004) and the possible causes are seawater intrusion and saline spray either from the sea and the salt-works. The result is a lower water salinity in the deep aquifer than in the shallow one, in the eastern sector. An explanation can come from higher hydraulic conductivity of the upper aquifer, where most of the water is pumped from wells and the saltwater intrusion has reached farther inland. The second explanation is related to the spray from the salt-works. On the western sector, closed to the recharge area and to the coastline, the two aquifers have a similar salination value. The reason could be that both have a natural and induced seawater intrusion (Balia et., 2009, Barrocu et al., 2004) and might be confirmed by measuring the resistivity and induced polarization, in order to define the extension of seawater intrusion for several metres inland and downland to a depth of the order of 150 m (Balia et al., 1994; Godio et al., 1999).

Groundwater heads of the Capoterra Plain have been studied previously. In figure 2, the comparison between groundwater contour maps for the shallow aquifer in January 1993 (Barrocu et al., 1994, figure 6A) and in November 2008 (CACIP, 2012; figure 6B) is shown. Both studies show groundwater heads decreasing more or less regularly from the western sector towards the middle of the plain, with a W-E direction. Both groundwater contour maps show groundwater head depressions due to aquifer exploitation at least in two different areas, where groundwater heads decrease below the sea level. The first one is in the northern side of the plain, while the second is located close to the salt-works and lagoon. Both interpolations show similar groundwater flow patterns.

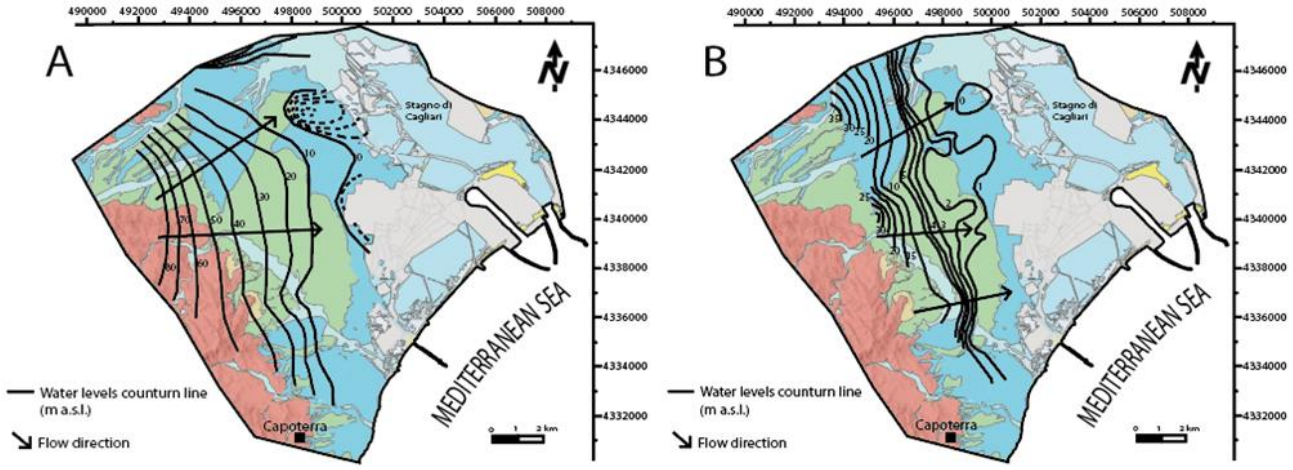

Figure 6. A) Phreatic aquifer groundwater contour map interpolated from data collected the during January 1993 showing a W-E groundwater flow direction (modified by [61]). B) Phreatic aquifer groundwater contour map interpolated from data collected during September 2008 showing a W-E groundwater flow direction (modified by CACIP, 2012).

The variation of the sedimentation inside the plain has produced discontinuous clayey levels, which reach the coastline but disappear towards the western part of the plain. Both aquifers are affected by saline intrusion, mainly due to large pumping rates linked to the industrial activity combined with scarce meteoric input (Napoli and Vanino, 2011). Furthermore, this variation in sedimentation has originated shallow clay lenses mainly distributed near the eastern part of the study area. Locally, these lenses can give place to perched aquifers.

Similar aquifer systems are described in the northern part of the Campidano (Arborea plain; Ghiglieri et al. 2017; Barroccu et al. 1995, 2004; Soddu and Barrocu, 2006). As for our study area, Arborea plain has the same characteristics, such as the presence of the sea, streams, the alluvial plain and the mountainous part. Moreover, the two areas show the same hydrogeological characteristics, with the presence of a phreatic aquifer that is separated from the deeper one by a clay level in the central-northern part of the plain while they are connected hydraulically in the southern part.

3. Data and methods

3.1 Data source

The hydrogeological model was implemented integrating surface mapping with information from lithological boreholes logs. Surface geological data are derived from the 1:50,000 maps of the "Geological Map of Italy" (Carta Geologica d'Italia), specifically Capoterra, Assemini, Cagliari e Pula sheets[1].

900 boreholes logs were collected, of which 225 from 'Italian Institute for Environmental Protection and Research' (ISPRA) and Sardinia Regional Environmental Agencies (ARPAS) and 675 from private companies (figure 7). The depth of the boreholes logs is mainly limited to 15 m (42%) or between 15 and 30 m (43%) below ground level; only 15% the boreholes reach greater depths, up to 187 m.

The compiled database includes information on stratigraphy, granulometry, and groundwater head information from wells and boreholes. Rough data were digitized and interpreted to identify the main granulometric classes based on the sediment lithological description. In detail, four main classes were defined: gravel, sand, silt and clay, each characterized by distinct hydraulic conductivity properties.

Hydraulic conductivity values, determined from field (Slug tests, step drawdown tests, multi-wells constant rate pumping tests) and laboratory tests (such as constant load tests), were compiled into a dedicated database. Hydraulic conductivity values calculated from filed test range between 1E-03 to 1E-06 m/s, which align with the predominant lithologies in the study area. Laboratory tests performed on fine-grained samples, collected from aquitards and aquiclude layers show hydraulic resulted in hydraulic conductivity values ranging from 1E-08/1E-11 m/s. These data were important for accurately representing the hydraulic conductivity distribution within the hydrogeological model.

[1] Available at www.sardegnageoportale.it

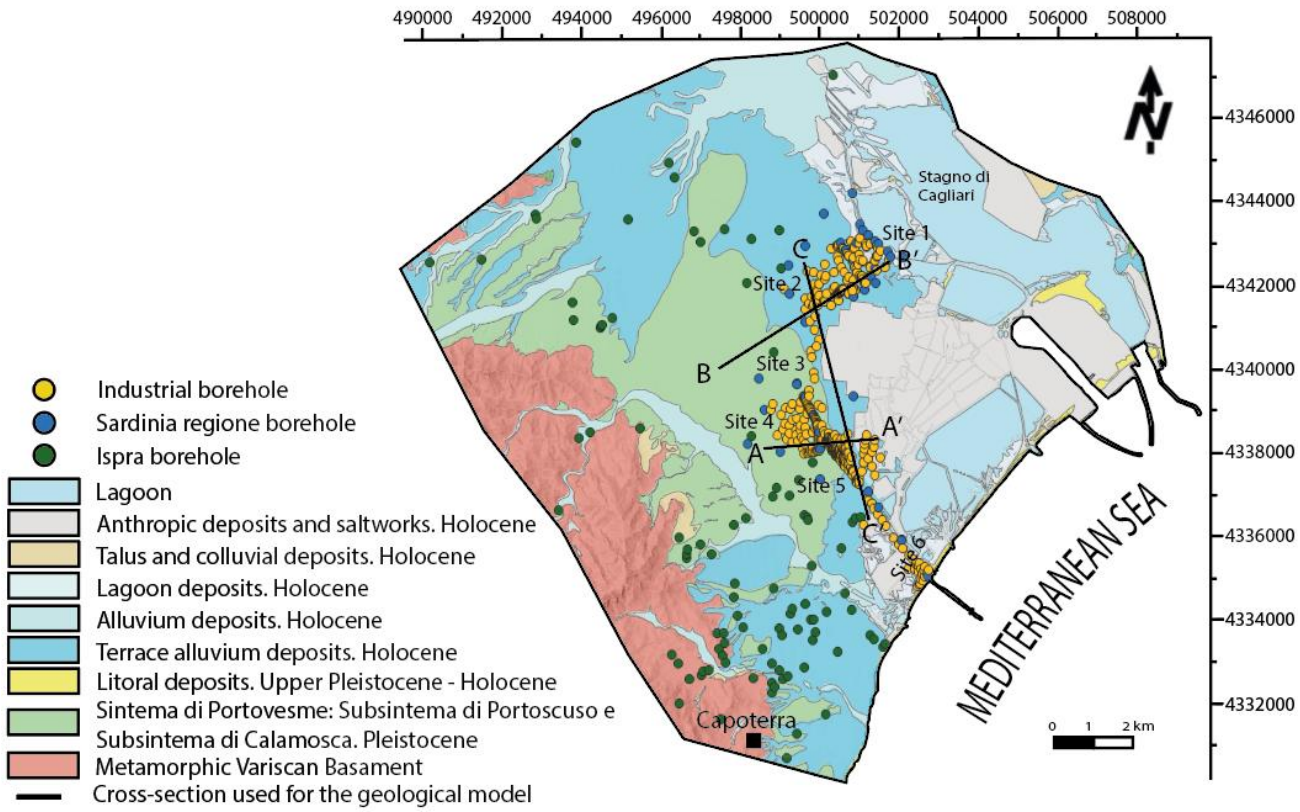

Figure 7. Geological map's details of the study area highlighted in the enlargement with respect to Figure 1-B, providing a closer view of the geological features essential to understand the possible depositional context. In addition, can be observed the distribution of the boreholes constituting the database. The black lines trace the cross-section used for the sedimentological model, described in detail in figure 6.

Groundwater flow model calibration was performed using groundwater heads measurements collected between 2018 and the end of 2023 from 6 different industrial sites (figure 3) where regular measurements are carried out, as well as rainfall/climate data from five of the six weather stations located in the study area, managed by ARPAS[2].

Figure 8 shows hydrographs recorded at site 2 (yellow line) and site 4 (blue line). This allows to quantify the amplitude of seasonal groundwater heads oscillations width and therefore identify the possible scenarios to be used as reference for numerical flow simulations. The analysis of groundwater heads over the past five years (figure. 8) shows a clear reduction of duration and magnitude of wet periods. This trend can be attributed to the significant decrease in precipitation observed in recent years and the simultaneous increase in temperature. The application of the Turc formula further supports this observation, revealing that effective precipitation (Q) is currently very low.

$$E=\frac{P^2}{\sqrt{0.9+P^2/L^2}}$$

[2] Rete meteo ARPAS - 2016-2022 (arcgis.com)

E=Evapotraspiration

T= Correct average Temperature

P=Average precipitation

L costant in Turc formula is:

$$L=300+25T+0.05T^3$$

The effective precipitation (Q) will be:

$$Q=P-E$$

(Turc formula)

This reduction in infiltration directly influences the behaviour of the groundwater head in the study area. During low groundwater heads periods, typically occurring in the summer months, the trend remains stable, mainly due to minimal precipitation input and the effect of elevated temperatures. For model calibration, an average groundwater heads scenario was defined as a reference and identified in April 2021 (green box, figure 8).

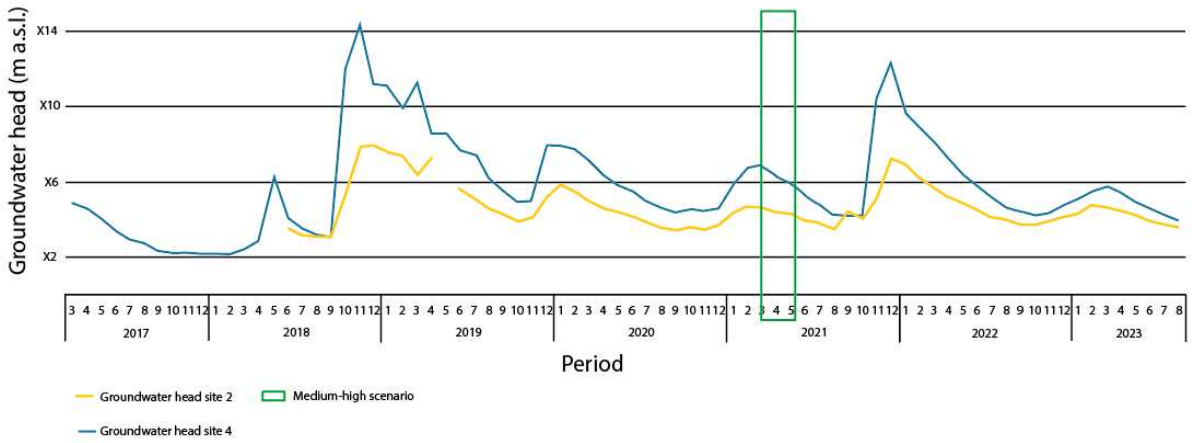

Figure 8. The graph shows the groundwater head variation of site 4 and site 2 from March 2017 to September 2023 on a weekly basis. The green box highlights the selected an average groundwater head scenario of April 2021 used for modelling purposes.

Figure 9 shows the phreatic aquifer groundwater contour map designed using data collected in April 2021. It has been realized by applying a “Convergent Interpolation”, as an interpolation algorithm, and using the observed groundwater head value of approximately 150 monitoring wells as well top. Afterward, the contour lines have been obtained by applying the process “create contour”, to the resulting surface. The main groundwater flow direction (W-E trend) is coherent with previous studies. In the western sector of the plain, the groundwater contour map of figure 2B shows two high groundwater heads zones (CACIP, 2012), which are not visible in the interpolated groundwater

contour map. This difference is related to the spatial distribution of the data used during the interpolation process. This project used only groundwater heads value collected within the industrial sites, whereas the CACIP data were built using monitoring well data distributed throughout the plain. The information from groundwater contour line of CACIP study, situated along the western part, were used to tune the numerical groundwater flow model due to a lack of data in the database.

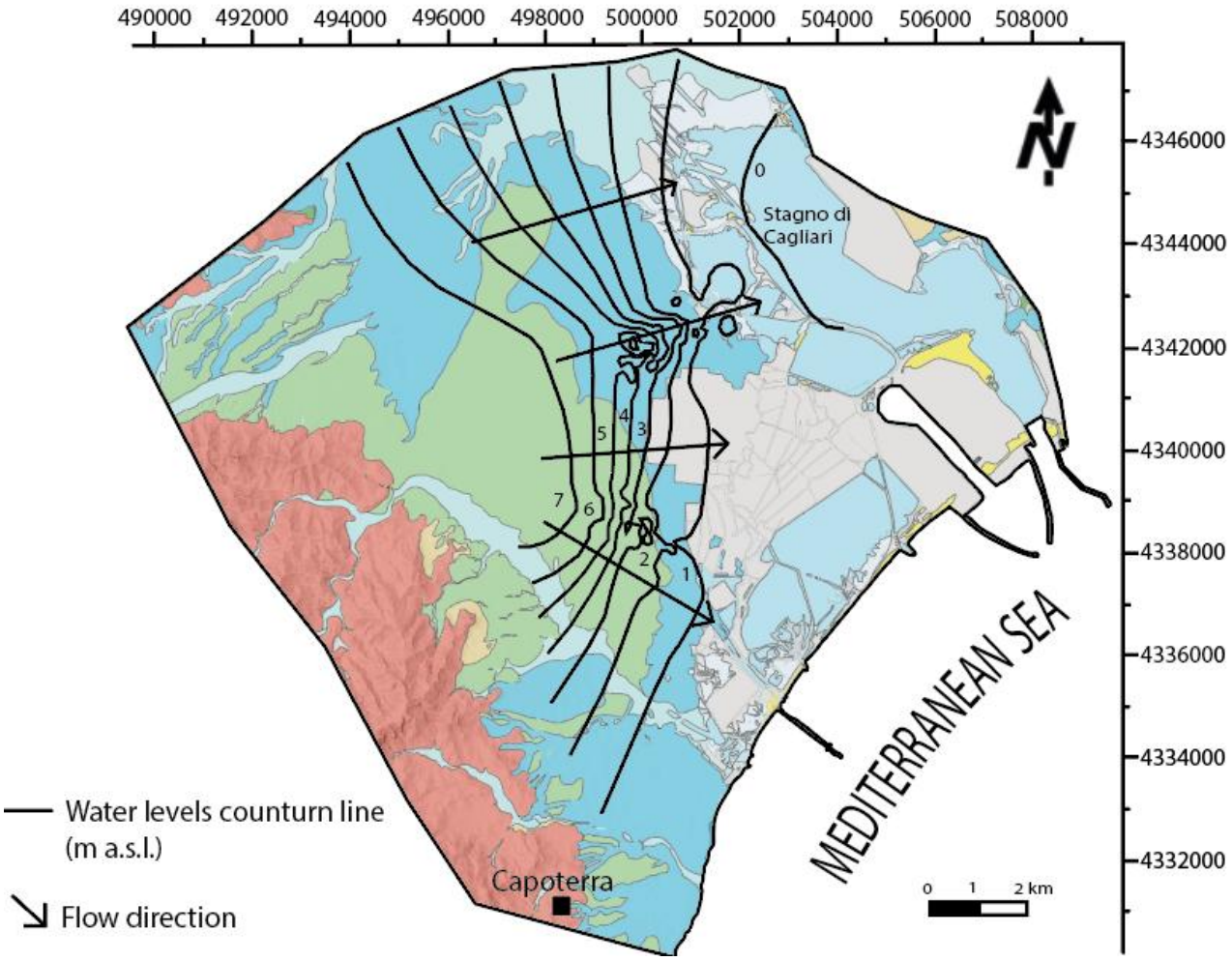

Figure 9. A) The groundwater contour line of the phreatic aquifer has been shown during April 2021. It is evident the W-E groundwater flow direction.

3.2 Sedimentological model

Starting from boreholes and surface data, geological cross-sections were drawn. Previous studies on the stratigraphy of the Capoterra plain did not include a detailed description of most recent Quaternary sediments, but described the general depositional context (Ardau et al., 1997; Barrocu et al., 2004; Sciabica, 1994; Barrocu et al., 2004), which is associated with the interaction between alluvial and marine environments (figure 10).

The areas near the saltworks and Santa Gilla lagoon are characterised by the presence of lagoon deposits (Holocene) above terraced alluvial deposits (Holocene) (figure 10, Section AA'). The former sediments are mostly composed of silt and clay, occasionally sandy and gravelly, while the

latter sediments are composed of mainly gravel and sand. Moving towards the centre of the plain, the depositional environment changes from an alluvial fan depositional environment to terraced alluvial deposits, showing fine material layers in the deep portions (figure 10).

Below Holocene deposits, the 'Subsintema of Portoscuso' and 'Subsintema of Calamosca', part of the 'Sintema of Portovesme' occur (figure 10). The 'Subsintema of Portoscuso', which characterises the centre of the plain, represents a continental deposit made of medium to coarse terraced alluvial gravels with subordinate sand and gravel, having a planar cross-bedding stratification. On the contrary, the 'Subsintema of Calamosca' represents a sandy deposit with a bidirectional tidal structure, made of sparse mollusks (i.e., Astrea Rugosa, Conus sp., Glycymeris glycymeris, Arca noae). Section AA' of figure 10, exhibits fine sediments of tentative Pleistocene age, in accordance with the presence of the 'Subsintema of Portoscuso'. These fine sediments were supposed to be of a Pleistocene age, differently from available cartography data.

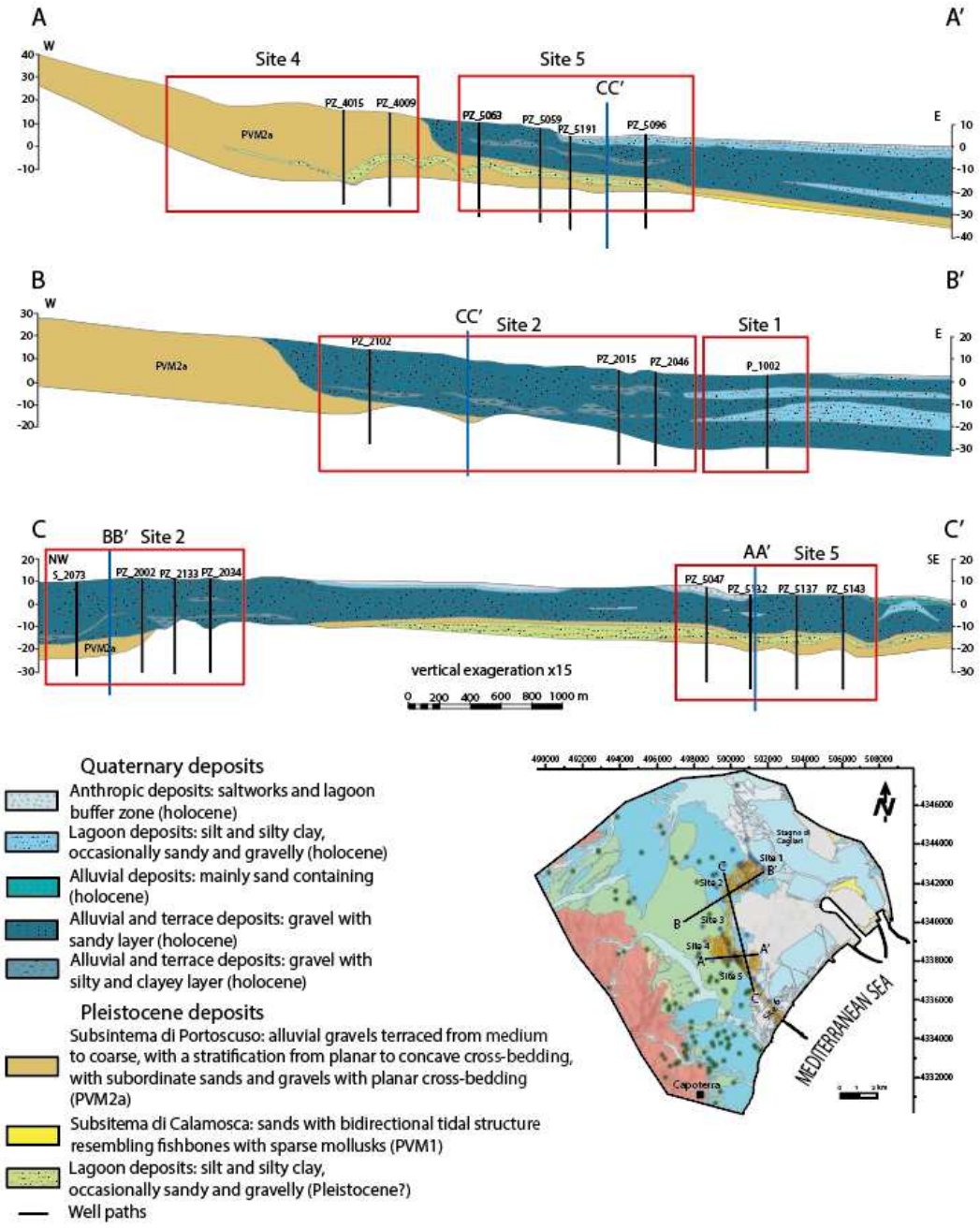

Figure 10. The sections show the distribution of Quaternary-Pleistocene deposits in our study area. As you can see, sections AA' and BB' show a transition from W to E of coarse to fine sediments, while section CC' shows, from NW to SE, respectively terraced alluvial deposits above Subsintema of Portoscuso and lagoon deposits located near the saltworks.

3.3 Conceptual model

The conceptual geological model summarises all available data and information which show an impact on the hydrogeology of the study area and provides a framework for creating the groundwater flow model (Andersen et al., 2015). The conceptual model phase is crucial and required in most environmental studies to comply with government regulation. The conceptual model defines the basic detail of hydrogeological system (geometry, hydraulic heads, hydraulic conductivity, etc.), contamination history and chemical processes acting in the subsurface and all the other features that influences the hydraulic behaviour of the system.

In order to understand the aquifer behavior and to simulate the groundwater flow, it has been necessary to outline some initial and boundary conditions, as well as a detailed generalization of the aquifer system. While the initial conditions include the hydraulic head distribution - assumed on historical groundwater head values from monitoring wells - the hydrological conditions, set along the boundaries of the conceptual model, determine the mathematical boundary conditions of the numerical model (Andersen et al., 2015). Such boundaries influence the groundwater flow direction calculated as a steady-state numerical model (Andersen et al., 2015). For the numerical model described in this article, the following constant heads were defined: the sea condition to the east and south, and a condition in the mountainous zone located to the west of the plain. A recharge boundary was also established, with its value determined by the average precipitation recorded in four meteorological stations during the analyzed piezometric period. Finally, the pumping values of the wells in the area were defined as specified flux boundaries. The model was divided into layers based on borehole data and groundwater head values, with each layer assigned to distinct hydraulic properties. The result is a model characterized by a shallow aquitard (approximately 10 meters below ground level), which locally supports a perched aquifer, and a second aquitard located about 20 meters below ground level, dividing the phreatic aquifer into two separate portions: a shallow portion and a deep portion locally and partially confined. Hydraulic conductivity was assigned based on the grain size distribution of each layer, considering the heterogeneity of the area. The recharge zone is located in the mountainous part of the study area, where the fractured basement is exposed, while the main discharge zones are the sea and areas of pumping well activity.

3.4 Three-Dimensional Hydrogeological model

The hydrogeological model is based on the lithological correlation and the preliminary definition of hydrogeological units showing similar hydraulic properties and behaviour. An aquifer system consists mainly of three key components: aquifers, aquitards and aquiclude. Using geological datasets and lithological correlation, driven by hydraulic properties, these components have been successfully reconstructed (Chapter 2, Appendix A).

The following section provides a description of the development of the 3D hydrogeological model. For further details, refer to Appendix A.

Petrel 2021© software (Schlumberger, 2010) was selected because it is a widely recognised software mostly used in the field of Oil and Gas and offers powerful capabilities in subsurface modelling. Using Petrel 2021©, a 3D hydrogeological model was developed by integrating the lithological units with their hydraulic properties. It provided a high computational power in the geostatistical simulation and allows the management of discontinuous layers (e.g., layers which pinch out) in the grid creation. However, as explained in Chapter 3.5, ModelMuse allows only for a 3D grid

in which each cell has a minimum thickness value. Therefore, in order to incorporate the layers pinch out, the 3D geological grid was modified as follows (more detail in Chapter 3, Appendix A):

I. The fine grid coherent with stratigraphic data, has been used to extract the thickness map for each zone;

II. A bulk shift has been applied to allow the grid to generate a continuous layer along the 3D grid as per table below;

III. The thickness map generated from fine grid, is discretized inside the continuous grid with a cut-off at 0.5 m;

IV. The regions created in this way would be merged in order to create the final grid coherent with the previous (figure 13).

Figure 11B shows the modified grid of the 3D hydrogeological model, adapted for subsequent use with ModelMuse. The grid was adjusted by adding a fictitious thickness to avoid the presence of pinch-outs, which ModelMuse cannot handle. However, to maintain the original model texture, thanks to the "sharp" boundary obtained from the thickness map (see step III of the above list) in all the different zones were assigned the code of the preceding layer, indirectly recreating the pinch out closure. This approach ensures consistency with the initial stratigraphic framework, preserving each zone's hydrogeological properties while overcoming the technical limitations of ModelMuse.

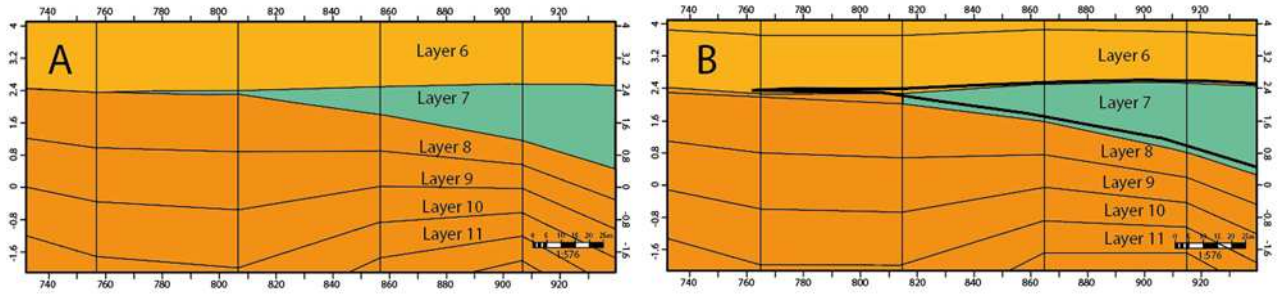

Figure 11. A) The figure A shows the 3D hydrogeological grid created by Petrel where the aquitard layers pinch out. B) The figure B shows the 3D hydrogeological grid modified in order to permit the running of the model on ModelMuse.

The grid created for this project consisted of 50 m × 50 m cells distributed over 20 layers, each with an extension of about 132 km^2 (more detail in Chapter 3, Appendix A).

The hydrogeological model was developed from a three-dimensional grid populated by importing facies data.

Elevation values of the surfaces, obtained by stratigraphic correlation, as described in **Section 4.2**, were assigned to the grid, creating a 3D model consisting of the following hydrogeological units: perched aquifer, Aquitard 0 (about 10 m from b.g.l.), shallow phreatic aquifer, Aquitard 1 (about 20

m from b.g.l.) and deep phreatic aquifer. Following the grid development, the next phase involved defining the number of layers for each zone in the model. The perched aquifer into 6 layers, the shallow phreatic aquifer into 10 layers, while only a single layer was assigned to each of the other zone.

Using borehole log data, the predominant facies were identified within every single layer and for each borehole; afterwards, facies and corresponding hydraulic conductivity values were assigned and distributed throughout the rest of the model, selecting the most appropriate method for the modelling phase (more detail in Chapter 4, Appendix A). Petrel software offers a wide range of algorithms for geostatistical distribution, two of them were tested in this project, the "Sequential Indicator Simulation" (SISIM) and "Indicator Kriging" (IK). The first one is a stochastic method that distributes properties on a cell-by-cell basis, constrained by directional variograms. It generates multiple realizations of facies or other properties (conditioned to integer values, like, 0, 1, 2, etc.) by calculating the best stochastic distribution based on well data, variograms, and other relevant input parameters. The simulation involves a random selection of facies within the bounds of these inputs, providing a range of possible distributions that represent uncertainty in the model. In contrast, the Indicator Kriging is a more deterministic geostatistical interpolation method. It estimates the probability that each point or cell in the model belongs to a specific category by applying the kriging algorithm. Indicator Kriging transforms categorical data into binary indicators and applies kriging to these indicators based on spatial correlations (variograms). The result is a probability map for each category, providing a deterministic estimate of the likelihood of occurrence without generating multiple realizations. IK is widely used in reservoir modeling and uncertainty assessment. Unlike SISIM, which produces multiple realizations, IK provides a single, probabilistic estimate of the spatial distribution of categories. The variogram is a crucial component of both methods, influencing how far the data correlations extend spatially.

Based on the sedimentary background and source direction of the study area, a main range of 400x400 m and a vertical range of 1 m were selected. The variogram correlates all the data included into the range. Finally, facies were distributed (using the facies data as starting point).

To maintain aquifer heterogeneity, grain size distribution was uploaded. The stratigraphic descriptions were converted into granulometric classes in compliance with the Italian Geotechnical Society (Associazione Geotecnica Italiana - AGI) 1977 guidelines. The simulation of the grain size classes, in % value, was nested within the previous simulation (SISIM model result) using the "Sequential Gaussian Simulation" algorithm (SGS) for each single facies code. The SGS method is a conditional simulation following a sequential principle under the multi-gaussian random function model (Emery and Peláez, 2011; Goovaerts, 1997). The advantage of this method is its simplicity and

effectiveness in generating numerical models with correct spatial statistics. The choice of the Sequential Gaussian Simulation (SGS) algorithm for the granulometric distribution was made after a comparison between the results obtained by applying both the Sequential Gaussian Simulation (SGS) method and Kriging nested to the facies model generated by the SISIM algorithm.

To define the distribution of hydraulic conductivity (K), a database was created gathering all laboratory and pumping tests, with a total of 104 records (figure 12). As shown in the graph in figure 12, the distribution of hydraulic conductivity reaches very low values (10E-10/10E-11 m/s) which are consistent with those obtained from laboratory tests. However, as illustrated in figure 18, these values were set to a higher value of 10E-7 m/s. This adjustment was made due to ModelMuse's difficulty in handling such low hydraulic conductivity values effectively within the model. Lithology associated to lab test was synthesised as per log description described above , while for pumping tests an equivalent lithology was considered (weighted average on thickness)following the same conversion process described for log desctipion. The sum of clay and silt in % showed, as mentioned, the best correlation with hydraulic conductivity (k).

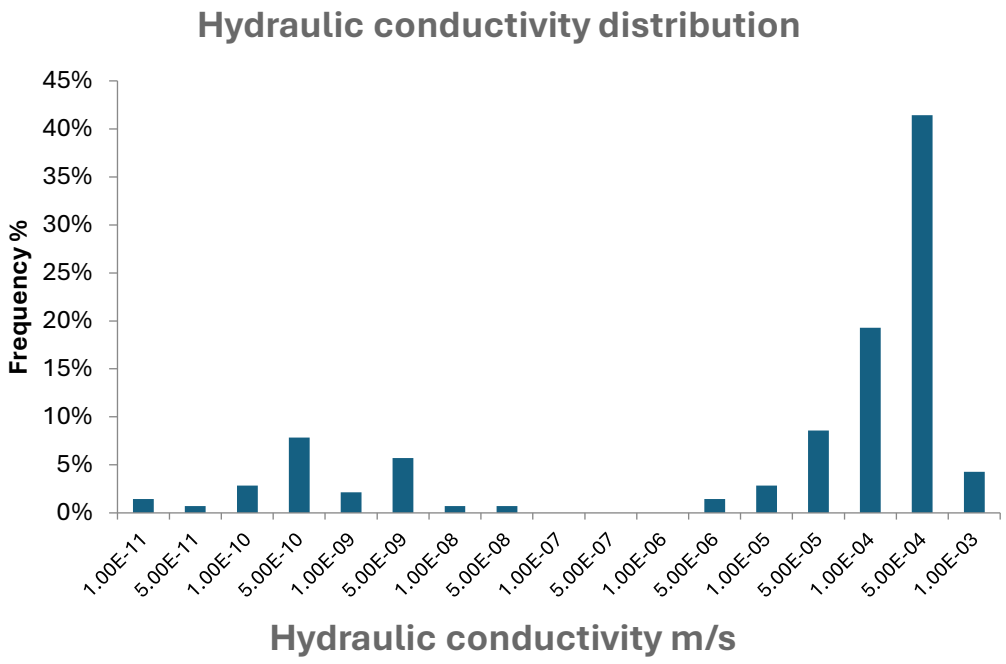

Figure 12. The graph in Figure 13 illustrates the distribution of hydraulic conductivity values which was obtained from laboratory and pumping tests. This graph is showing a higher concentration for the higher hydraulic conductivity value. These higher values are typically representative of the aquifer zones, where the permeability is greater.

3.5 Numerical groundwater flow model

The numerical groundwater flow model was simulated using MODFLOW 6, which is supported by ModelMuse version 5.1.1, an open-source graphical user interface provided by the U.S. Geological Survey (USGS; Winston, 2019). MODFLOW 6 efficiently simulates groundwater flow. The governing

equation for groundwater flow is formulated based on a control volume finite difference approach. This equation can be expressed in three dimensions, considering hydraulic conductivity in the x, y and z directions, specific storage and external inflow/outflow (Langevin et al., 2017). The general form of the governing equation is:

$$\frac{\partial}{\partial \mathrm{t}} (S_s h) = \nabla \cdot (K \nabla h) + W$$

(1)

where

h: is the hydraulic head (piezometric level).

Ss: is the specific storage of the porous media.

K: represents the hydraulic conductivity tensor.

W: includes all external water sources or sinks (e.g., recharge, pumping) (Langevin et al., 2017).

This equation describes the behaviour of water flowing through porous media and is based on Darcy's Law for flow and mass conservation.

The specific parameters of MODFLOW 6 are described in **Table 1**.

Table 1. Specific parameters of MODFLOW 6.

Parameters	**Symbol**	**Unit**	**Description**
Hydraulic head	h	[m]	Elevation of the water surface in a well
Hydraulic conductivity	K	[m/s]	Measure of the material's ability to transmit water
Specific storage	S_s	[s^{-1}]	Volume of water released from storage per unit declines in hydraulic head
Time step	Δt	[m]	Time increment for numerical solution
Spatial step (x, y, z)	Δx, Δy, Δz	[m]	Grid size in the x, y and z directions
Source/sink term	W	[s^{-1}]	Rate of water entering or leaving the system.
Storage coefficient	S	[-]	Product of specific storage and aquifer thickness in confined conditions.

Based on the above consideration, the following section provides a description of the development of the numerical flow model. For further details, refer to Appendix B.

The choice of ModelMuse, along with Petrel 2021© for hydrogeological numerical modelling, was driven by their compatibility in grid type and indexing. Data on the grid, surface elevation, and hydraulic conductivity distribution of Petrel 2021© were directly transferred to ModelMuse (figure 13, section A). Unlike Petrel 2021©, which can handle pinch-outs (cell thickness equal to zero), ModelMuse requires minimum cell thickness (0.1 cm in this project grid). Consequently, the hydrogeological model grid was adjusted in order to assign a minimum thickness to these discontinuous layers, minimising the impact on interpolation steps.

To prevent the possibility of having two or more monitoring or pumping wells in the same cell, a quadtree refinement was performed. Starting from the ModelMuse grid, the centroid of each cell was exported to Petrel, where an average hydraulic conductivity map was created to define the hydraulic conductivity values for each cell centroid. Subsequently, this data was imported into ModelMuse and intersected to set the hydraulic conductivity values for the cells (figure 13, section B).

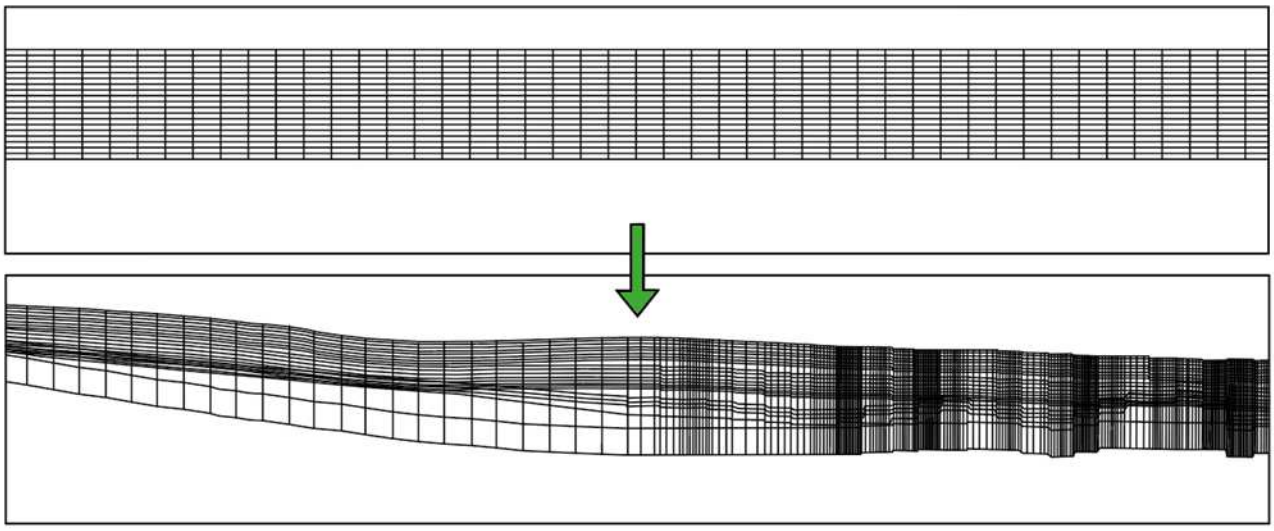

Figure 13. This figure shows the passage from a regular grid created on ModelMuse (section A) to the final numerical groundwater flow grid model, where it was importing the surface elevation and the quadtree refinement (section B).

The model has been set up as a steady state. The Specified-Head (CHD) package was used to simulate specified constant head boundaries, the Recharge package (RCH) was implemented to input recharge over polygonal area, and the well package (WEL) allowed to input of a pumping rate. In addition, the Observation Utility Package (OBS) was used to input observed groundwater head values (about 300).

After having identified the groundwater head scenario (**figure 8**) and the choice of the different packages, the flow model calibration process was finally started by collecting groundwater head data.

4 Results

4.1 Hydrostratigraphic model

Once the hydrogeological units were defined and correlated, porosity/hydraulic conductivity values were assigned (**Table 2**), on the basis of grain size distribution.

Table 2. Sedimentological and hydrogeological units relationship based on the hydraulic conductivity value obtained by pumping tests and literature. (* http://www.sardegnageoportale.it/ carta delle permeabilità dei substrati della Sardegna)

Sedimentological Units	**Prevalent lithological description**	**Hydraulic conductivity ***	**Hydrogeological units**
Lagoon deposits	Silt and silty clay	low conductivity	Aquitard 0 and aquitard 1
Alluvial deposits	Sand	high conductivity	Perched aquifer, shallow phreatic aquifer, deep phreatic aquifer
Terraced deposits	Gravel with sandy layer	medium to high conductivity	Perched aquifer, shallow phreatic aquifer, deep phreatic aquifer
Subsintema di Portoscuso	Gravel and sand	medium to high conductivity	Perched aquifer, shallow phreatic aquifer, deep phreatic aquifer
Subsintema di Calamosca	Sand	medium to high conductivity	Perched aquifer, shallow phreatic aquifer, deep phreatic aquifer

The lithological units result in a complex hydrogeological setting, featuring a multilayer aquifer in the western region transitioning to a phreatic aquifer in the lagoon and/or marine area and occasionally presenting a perched aquifer. Figure 14 shows the simplified hydrogeological model developed through two cross-sectional representations extending from a mountain area (west side) to the Santa Gilla lagoon (east side) and showing the transition from an undifferentiated aquifer to a multilayer phreatic aquifer. The western sector is characterised by a depositional environment associated with an alluvial fan and terrace deposits; in this area, no continuous clay layers in the first 30 m b.g.l. were identified. Going eastward, the marine deposition dynamic becomes relevant. In particular, clay lenses are predominantly observed near Santa Gilla lagoon, resulting in a more complex architecture of the phreatic aquifer, which is locally split into a shallow and a deep (locally confined) portion. Nevertheless, it is possible to find a perched aquifer locally. The interdigitation of sandy and clay layers could be explained by eustatic variations.

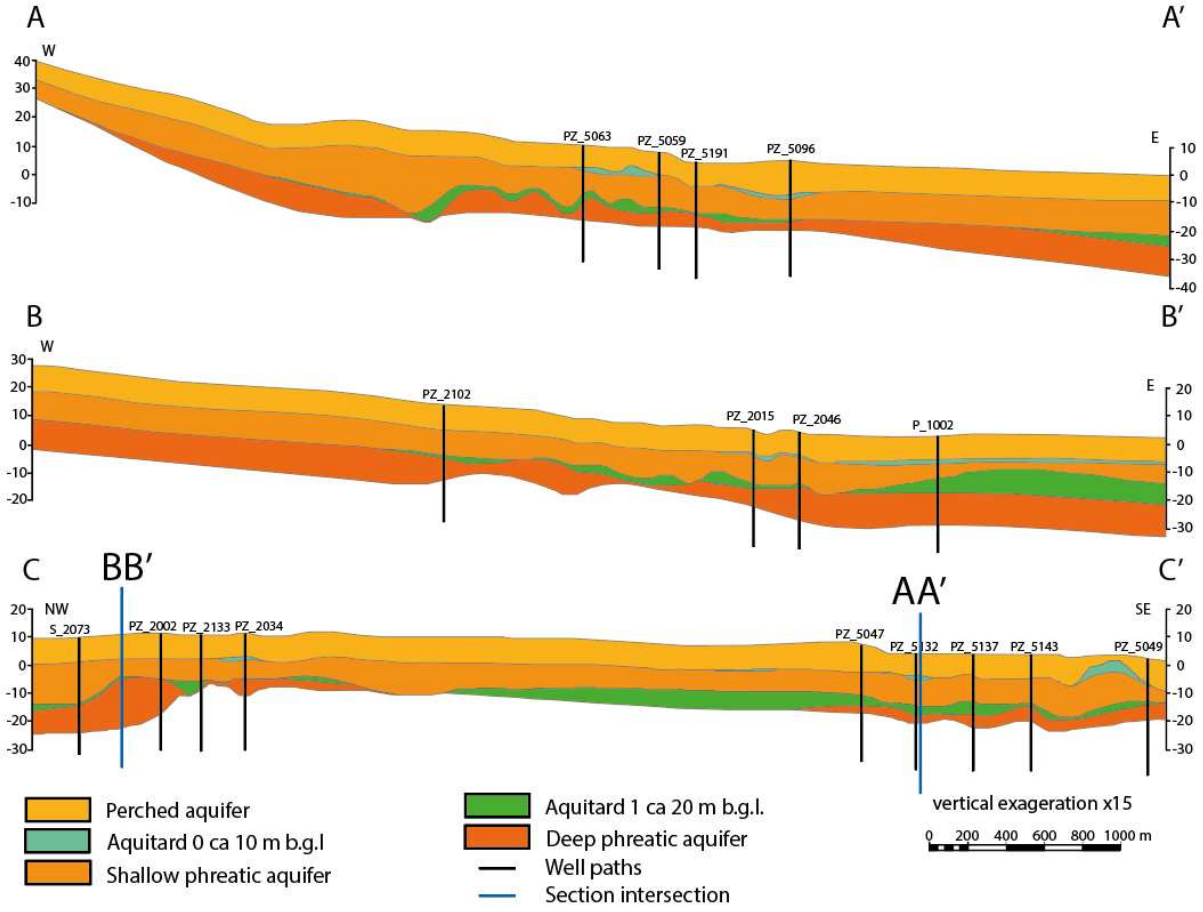

Figure 14. Hydrogeological cross section based on our sedimentary cross section, which position has been previously represented in figure 2. The C-C' section is crossed perpendicularly from W to E by the A-A' and the B-B' sections. These two underline the discontinuity of Aquitard 1, which tends to disappear towards the mountain zone located in the western part of our study area. Therefore, the shallow phreatic aquifer and the deep phreatic aquifer are hydraulically interconnected. On the contrary, the C-C' section shows a continuous tendency of Aquitard 1 towards south, which is probably due toa different depositional environment.

4.2 Hydrogeological model

The hydrogeological model was developed using Petrel 2021©. Borehole log analysis and facies interpretation of the lithological data was carried out and imported on the software. Subsequently, the hydrogeological correlation process was performed (figure 15). Following the data logs, two aquitards were correlated, also considering groundwater head values (figure 15): a shallow aquitard (ca 10 m b.g.l.) locally supporting a perched aquifer, and a second aquitard located about 20 m b.g.l., dividing the phreatic aquifer into two separated portions (a shallow and a deep one, the latter locally and partially confined) (figure 14).

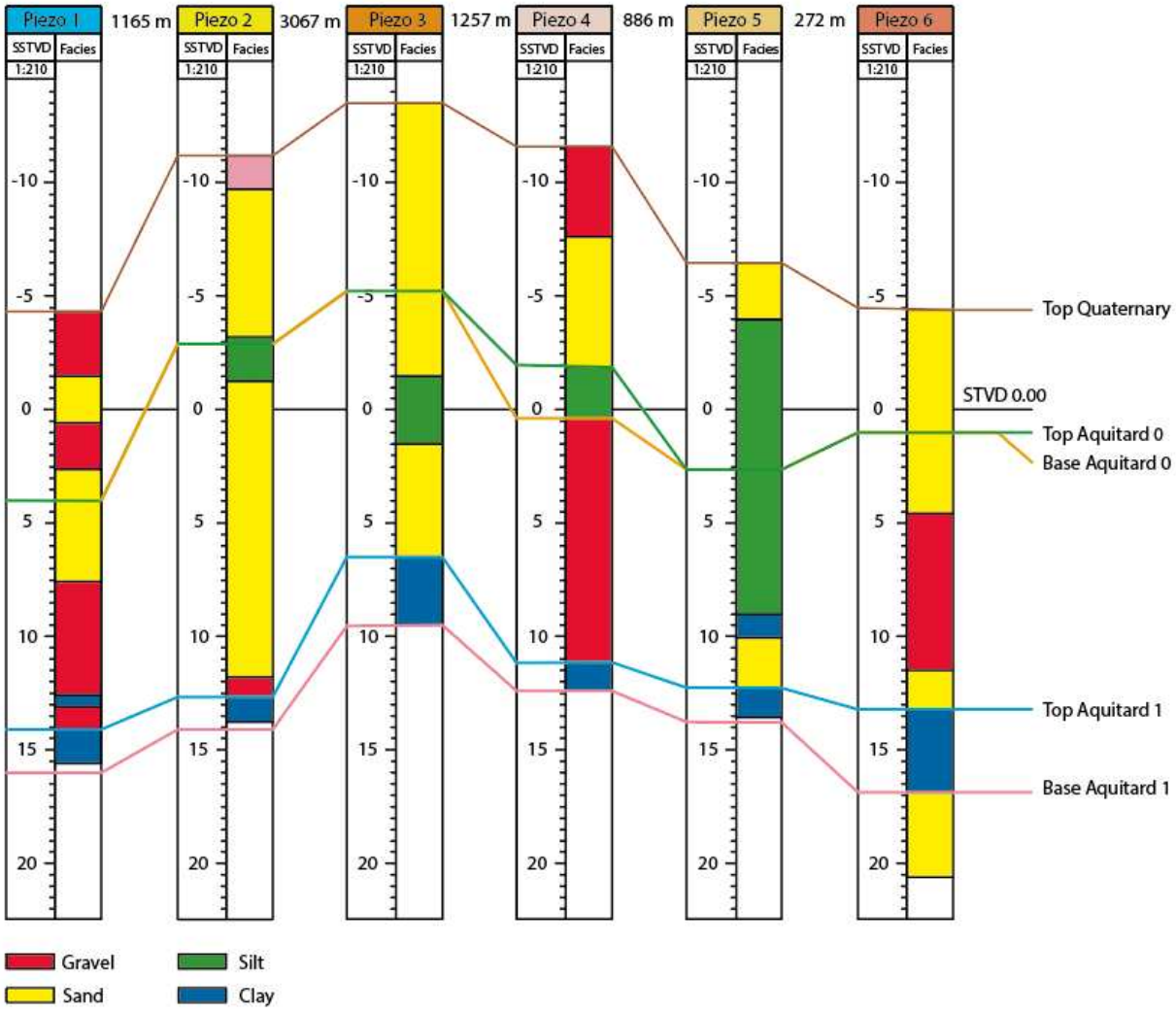

Figure 15. The hydrogeological correlation allowed to define the possible surfaces, which characterised the hydrogeological model. By following the lithology of the borehole log data, it has been possible to define the presence of a shallower aquitard (highly discontinuous) and a deeper aquitard that define the phreatic aquifer target of the study.

As mentioned in chapter 3, the hydrogeological model was populated with several geostatistical distribution. Figure 16 compares the facies distribution results produced by different combination of algorithms and variogram. In detail, figure 16A shows the facies distribution using the Sequential Indicator Simulation (SISIM) algorithm. This algorithm maintains statistical texture within well data across the entire model, even in areas without data, leading to a stochastic distribution that maintains the original facies statistics. Moreover, figure 16B displays the Indicator Kriging algorithm, which uses the same well data and variogram (400x400 m) as in figure 16A. In areas with well data, the results are similar to those in figure 16A, but in areas without data, Indicator Kriging tends to create continuous facies lenses by averaging information from the nearest well data points. At the end, figure 16C represents the results of Indicator Kriging using a much larger variogram (2000x2000 m). This approach incorporates information from a larger number of wells, leading to greater heterogeneity across the model. However, despite this wider range, Indicator Kriging

continues to create smooth and continuous lenses in areas with limited data. The comparison between the figures highlights how the SISIM model (figure 16A) better represents the statistical variability of facies across the grid, even in data-sparse regions. In contrast, Indicator Kriging (figures 16B and 16C) tends to produce more deterministic, lens-like structures, with increased heterogeneity only when using a larger variogram (figure 16C). However, the limitation of creating overly continuous lenses remains when using Indicator Kriging, especially in areas with sparse data.

Two sections were created for each model in the same areas (as shown in figure 16) to compare how the algorithm and variogram affect the facies distribution, both in zones with well data and in those with no information. Sections 1, 3, and 5 illustrate how the presence of well data influences facies distribution. The results of these three sections remain quite similar, even when applying different algorithms (SISIM for Section 1 and Indicator Kriging for Sections 3 and 5), as long as the variogram used is the same (Sections 1 and 3) or larger (2000x2000 variogram in Section 5). In these data-rich areas, the choice of algorithm has a limited effect, leading to consistent facies modeling.

In areas where data distribution is scarce, the modeling results can be significantly different depending on the used algorithm. Sections 4 and 6, created using Indicator Kriging, show continuous lenses strongly influenced by the variogram size. The larger variogram (as in Section 6), the more continuous and homogenized the lenses become, reducing the model's heterogeneity. In contrast, Section 2, produced with SISIM, offers a more realistic model, as the algorithm preserves the same statistical distribution used in areas with well data. For this reason, it was decided to proceed with facies modeling using the SISIM algorithm.

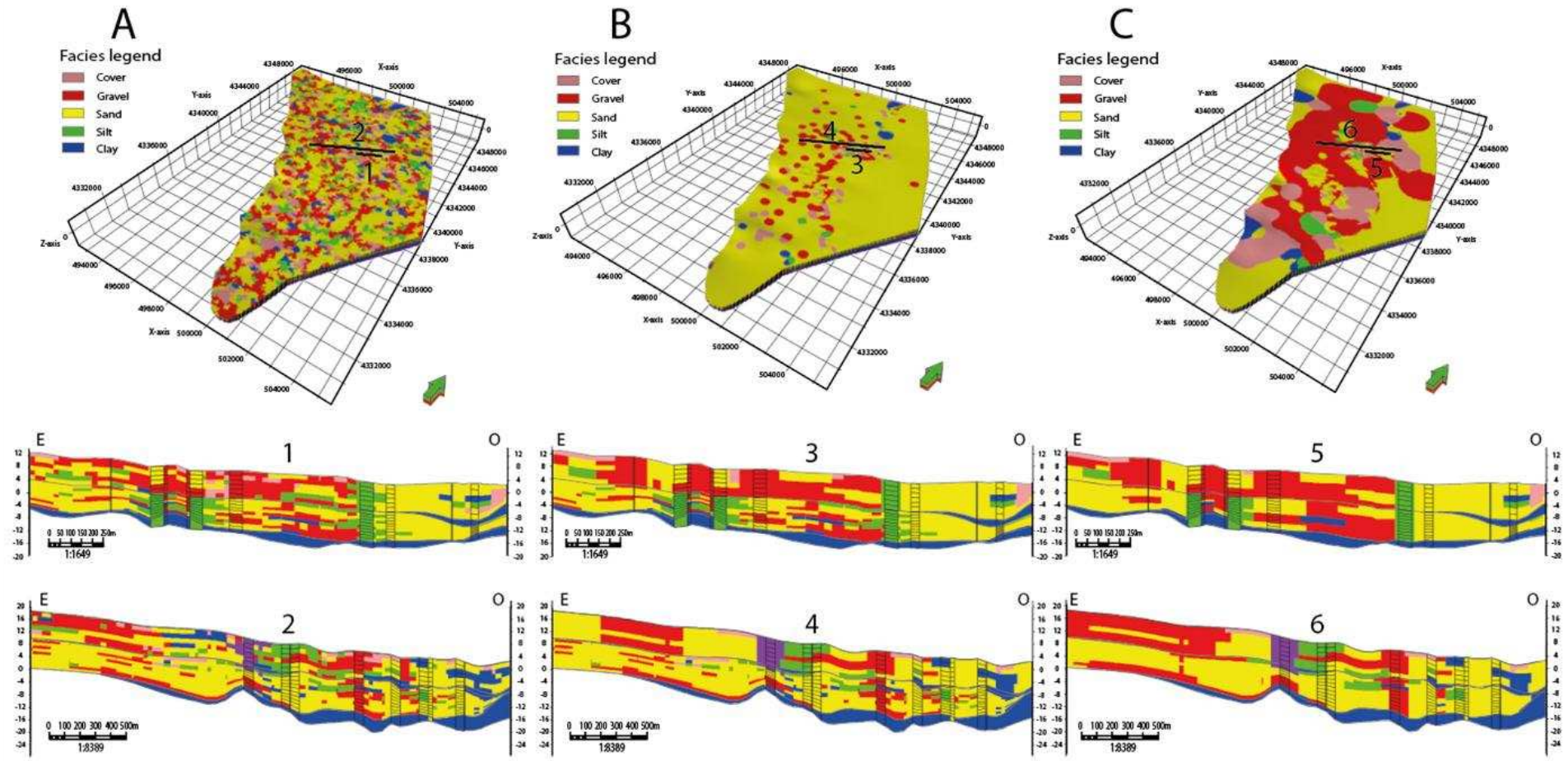

Figure 16. A) Result of the facies distribution using the "Sequential indicator simulation" algorithm and a variogram 400x400 m. The figure shows the distribution of the 5 main facies classes, which were obtained from the description of the lithological logs. Figure 14A presents the facies distribution obtained through the SISIM algorithm, whereas Figures 14B and 14C display the results of applying the Indicator Kriging (IK) algorithm. Sections 1, 3, and 5 compare the two algorithms and variogram effects in areas with high well data density, showing relatively small differences between the SISIM and IK algorithms when well data are abundant. On the other hand, Sections 2, 4, and 6 compare the algorithms and variograms in data-sparse regions. In these areas, the differences are more pronounced, with the SISIM algorithm providing a more heterogeneous and geologically plausible facies distribution compared to the smoother and more continuous lenses produced by the IK algorithm, particularly with larger variograms (as seen in Figure 14C).

In figure 17, Section A, which was generated using the Sequential Gaussian Simulation (SGS) method, shows a model with sharper transition. These sharp changes are consistent with the variations observed in the well log data, making this approach more representative of the actual underground heterogeneity. In contrast, Section B, obtained through the Kriging method, displays a smoother and more homogeneous model, especially in areas with sparse well data. This smoothness can oversimplify the true complexity of the subsurface, making Kriging less ideal for representing the abrupt changes that characterize the study area's facies distribution.

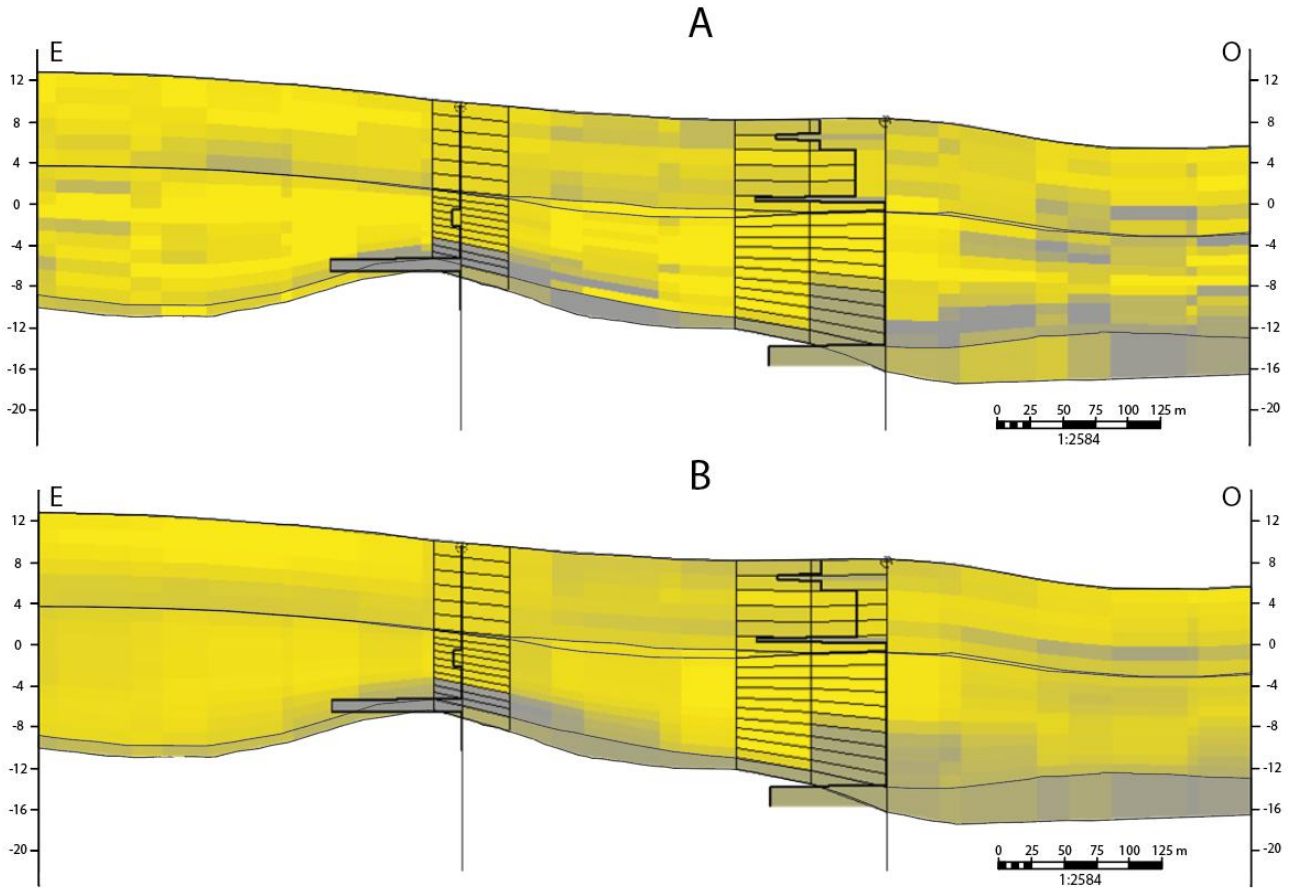

Figure 17. Section A illustrates the grain size distribution created using the Sequential Gaussian Simulation (SGS) algorithm, highlighting sharp and well-defined transitions between the different facies. In contrast, Section B represents the grain size distribution produced by the Kriging method, where the transitions are smoother and more gradual, leading to a more homogeneous model.

For this part, the sum of clay and silt percentage was considered as a generic “fine material” since hydraulic conductivity showed a negative correlation with this parameter, see purple line in figure 19. In figure 17, the high percentage of fine material is represented with grey coloring. The comparison between figure 16A and figure 18 shows how the distribution of granulometric percentages is associated with the distribution of facies. It can be observed that a significant percentage (up to 40%) is modelled inside the coarse facies (Sand and Gravel) according to log description confirming the high heterogeneity observed.

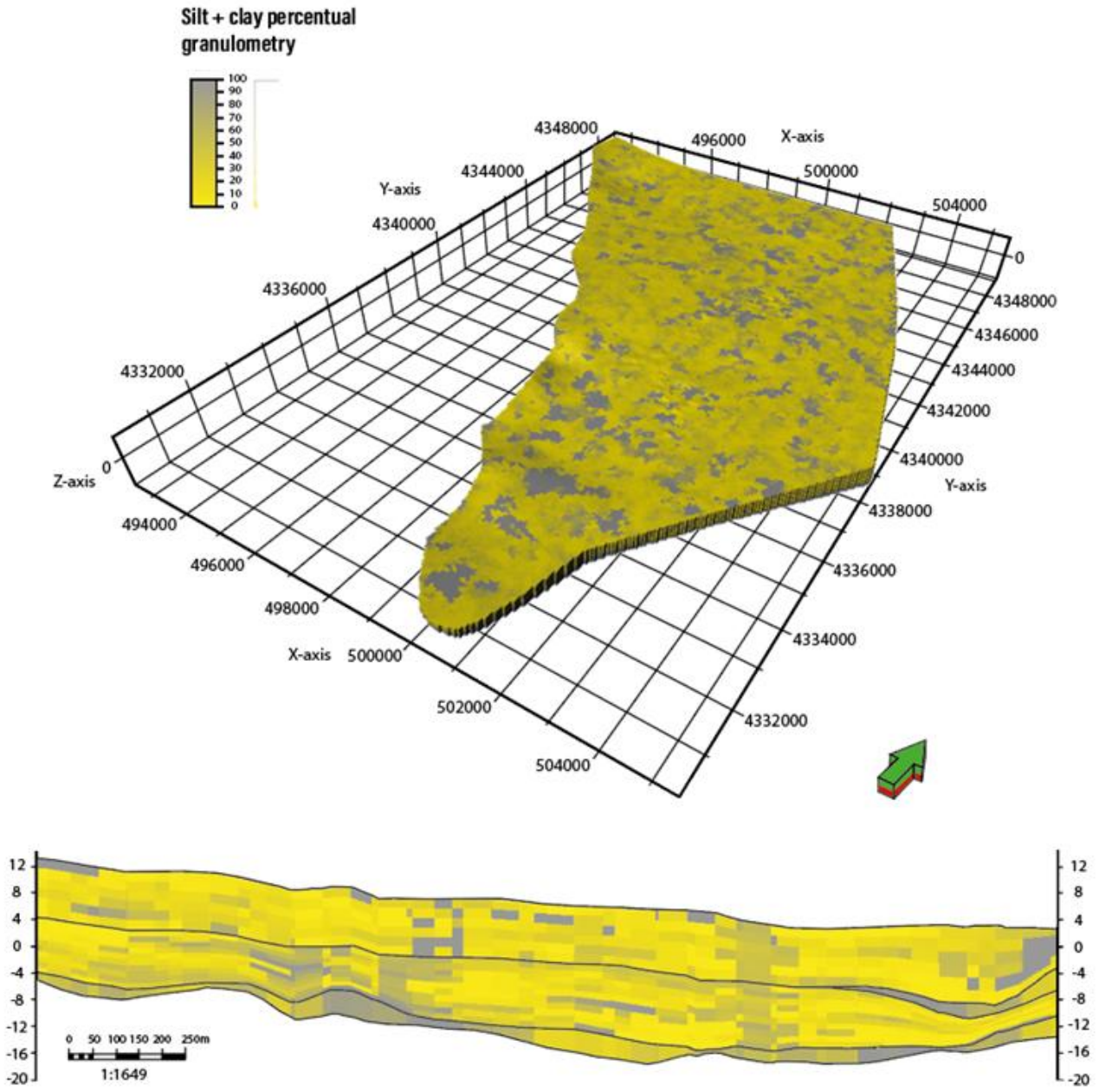

Figure 18. Result of the sum of Silt and Clay distribution using the "Sequential Gaussian Simulation" algorithm and a variogram 400x400 m. The model in the figure shows the distribution of the percentages of grain sizes of silt and clay, achieved from the stratigraphic descriptions of the facies.

The 3D distribution of K was obtained with SGS and a bivariate algorithm, nested to the previous granulometric distribution. This combination was able to reconstruct a distribution of a given cross-plot. Results are represented in figure 19, for distributed geostatistical samples the facies were visualised as Z-axis. The figure 19 shows how the gravel and sandy facies are much more concentrated in proximity to higher hydraulic conductivity values. The hydraulic conductivity distribution was achieved applying the bivariate algorithm with the granulometric percentages of silt and clay distribution.

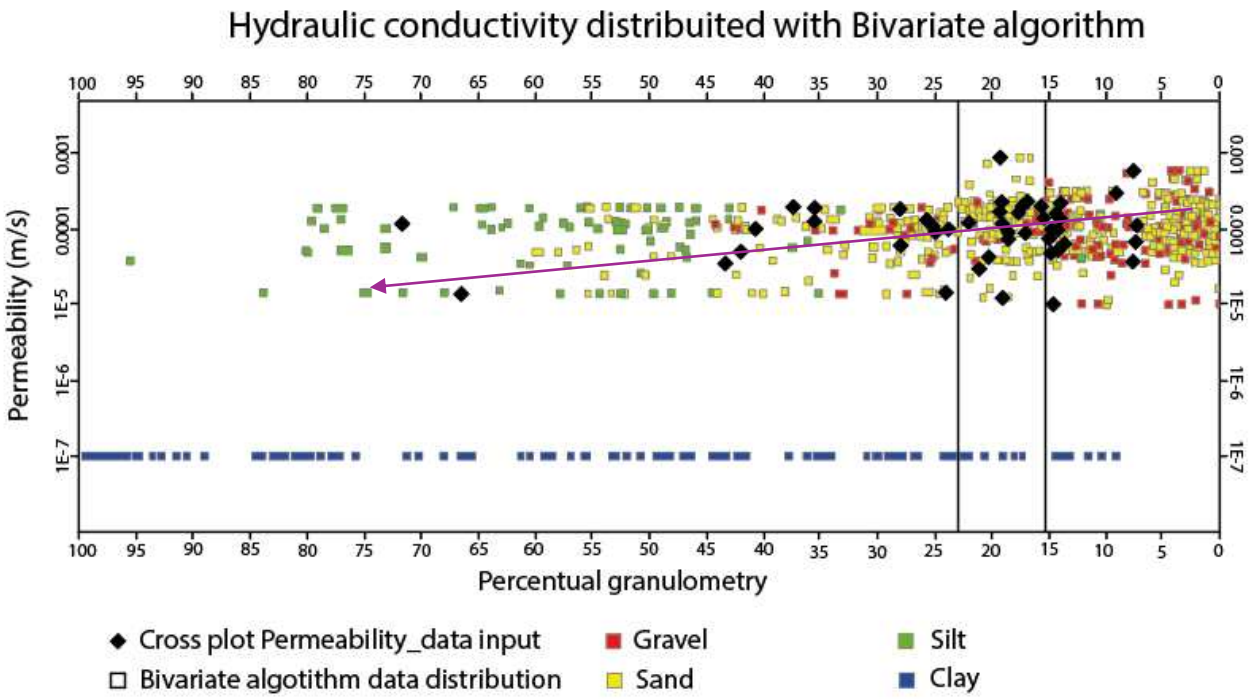

Figure 19. Graphic shows the hydraulic conductivity distributed with the Bivariate algorithm.

Figure 20 compared the facies modelling results (figure 20A) with the hydraulic conductivity distribution (figure 20B). It can be observed that the areas where clay and silt are distributed (blue and green in figure 20A) correspond to those having a lower conductivity (blue color in figure 20B). On the contrary, areas with a lower content of fine material (yellow and red color in figure 20A) correspond to zones with greater hydraulic conductivity value, which in figure 20B are represented by colors tending towards red.

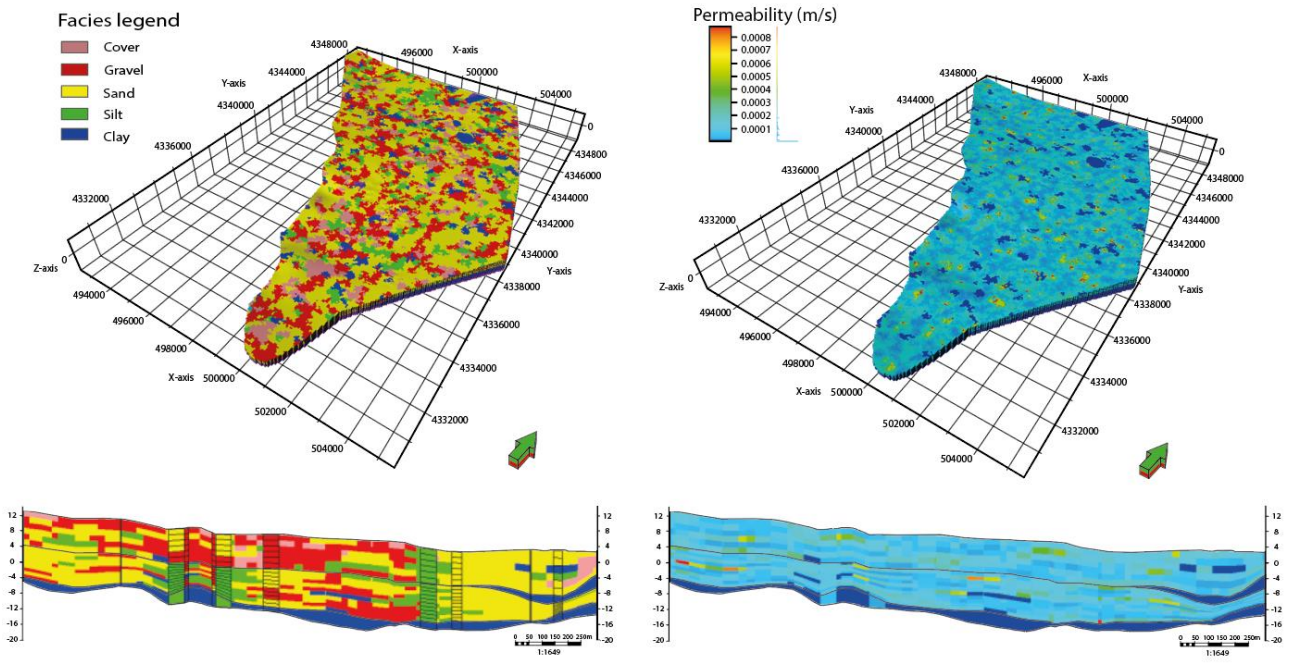

Figure 20. A) Result of the facies distribution using the "Sequential indicator simulation" algorithm and a variogram 400x400 m. B) The hydraulic conductivity value distribution applying the bivariate algorithm with the silt and clay percentual granulometric distribution.

4.3 Numerical groundwater flow model and calibration

The hydrogeological model represented the frame for developing the numerical groundwater flow model, which was implemented in ModelMuse, reproducing the three-dimensional grid of the hydrogeological model. Nevertheless, to avoid the possibility of having two or more monitoring or pumping wells in the same cell, a quadtree refinement was performed. Hydraulic conductivity data were imported into the numerical model.

To simulate the numerical flow model, a steady-state model with a starting time equal to "−1 s" and an ending time equal to "0 s" was set up. Regarding the boundary conditions, two Specified-Heads (CHDs, usually associated with the constant head boundary) were assigned; the first CHD with values ranging between 4 and 35 m on the western part of the study area and the second CHD set at 0 near the sea coastline, to represent the sea level. While the Recharge (RCH) values were calculated using rainfall data during the selected period. The same process was applied to the WEL package data, assigning a specific pumping rate to each active well (approximately 150). Groundwater heads measured at the monitoring wells network (about 300) were imported using the Observation (OBS) package.

By running the model, the hydrogeological balance and the simulated groundwater contour map were produced.

The calibration process of this scenario was obtained by minimizing the difference between measured and simulated groundwater heads by a trial-and-error procedure: boundary conditions or

conductivity distribution were iteratively modified to enhance final calibration results. Figure 21 shows a cross plot where measured groundwater heads are plotted on the X-axis, and simulated groundwater heads are plotted on the Y-axis. The purpose of this graph is to show how plotted values of individual monitoring wells deviate from a bisector of the second and fourth quadrant. The calibration results of the average head scenario are shown.

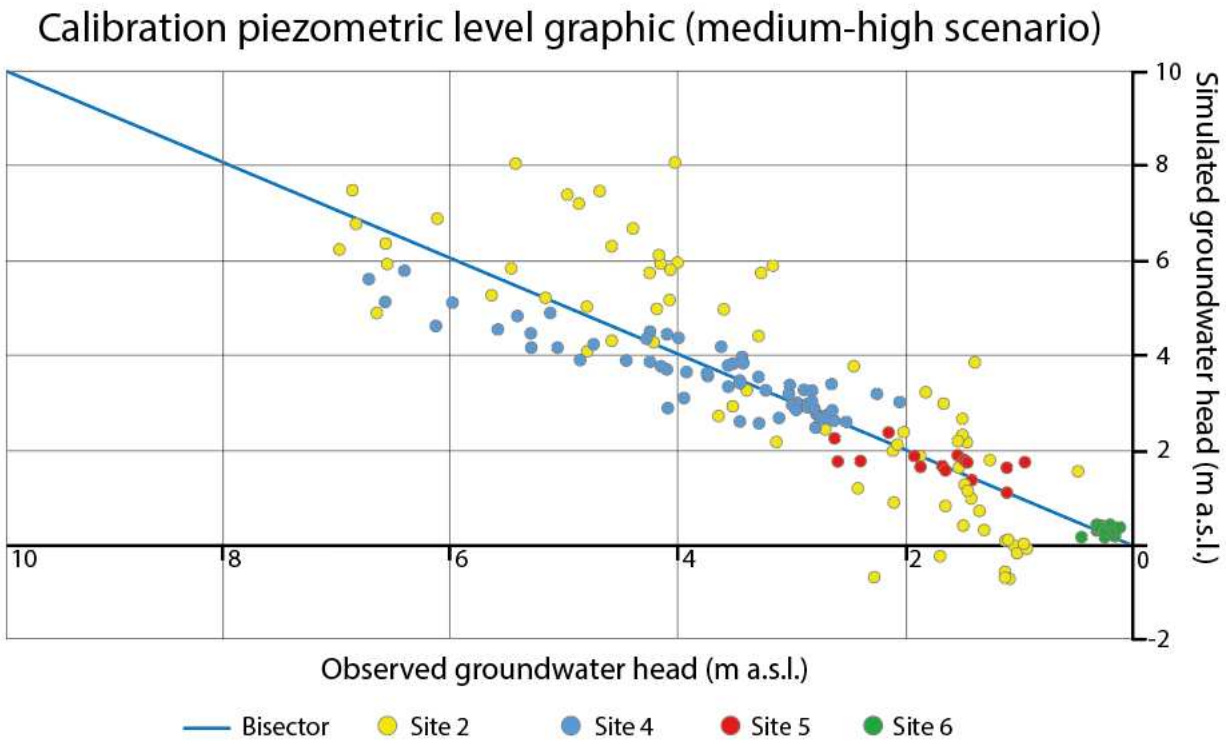

Figure 21. Graph represented an average scenario, where the difference between the measured groundwater heads (X-axis) and the simulated groundwater head (Y-axis) is plotted. The plot represents the groundwater flow direction having the highest groundwater head placed west (left side of the plot).

Figure 21 shows the calibration result of an average heads scenario. A significant correlation between observed and simulated groundwater heads is noted. While site 4, 5 and 6 are well represented with very low residuals, some groundwater heads measurements at site 2 show greater residuals between observed and simulated groundwater heads.

These monitoring wells measure the groundwater head of the phreatic aquifer, which is the focus of the study. Figure 22 shows the simulated groundwater contour map. The comparison with the interpolated groundwater contour map (figure 9) indicates a good correlation. Both contour maps show a W-E main flow direction, despite the NNW-SSE secondary trend in the southern sector. The hydraulic gradient is the same in both interpretations.

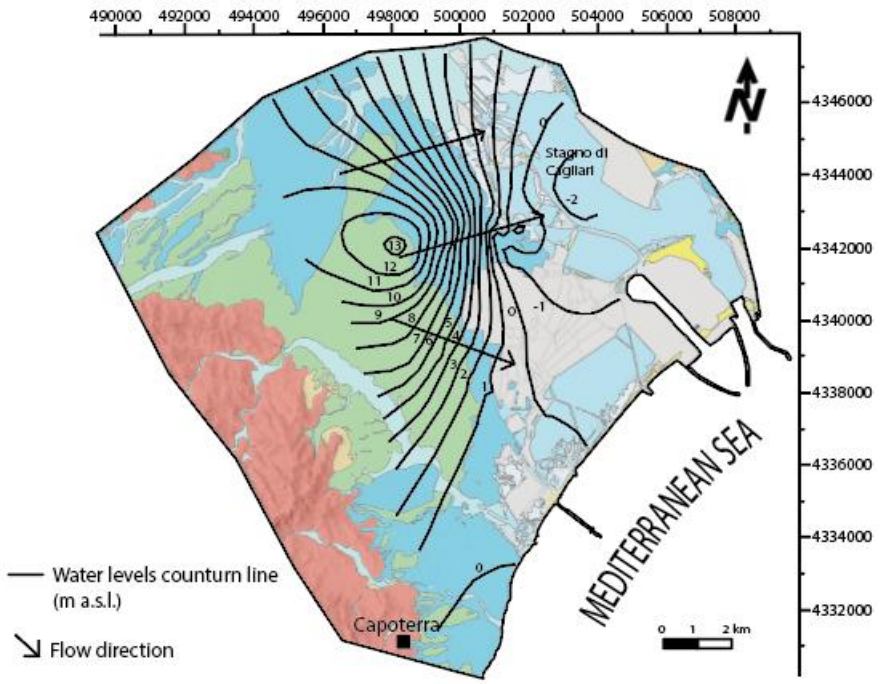

Figure 22. A) Groundwater head contour lines obtained by the interpolation of the groundwater head of the average scenario has been shown. The main W-E groundwater flow direction have been highlighted.

The comparison with groundwater contour map carried out by CACIP (CACIP, 2012) (figure 6B) reveals some differences, mainly related to the different data set used. As mentioned above, in this project only groundwater heads data collected within industrial sites were considered, whilst CACIP used data throughout the plain. This allowed to explain the differences of the groundwater contour line in the western area of the plain, where these data were not available for the selected period. Conversely, sites areas have better groundwater contour line details. Other differences are related to the increase in exploitation activities in the industrial areas in recent years.

The hydrogeologic balance of the plain flow model showed the difference of 0.15% between calculated in and out flow rates. It must be stated that data regarding groundwater withdrawal related to agricultural activities, drinking use, and other industrial activities were not available, hence they were not included (figure 23).

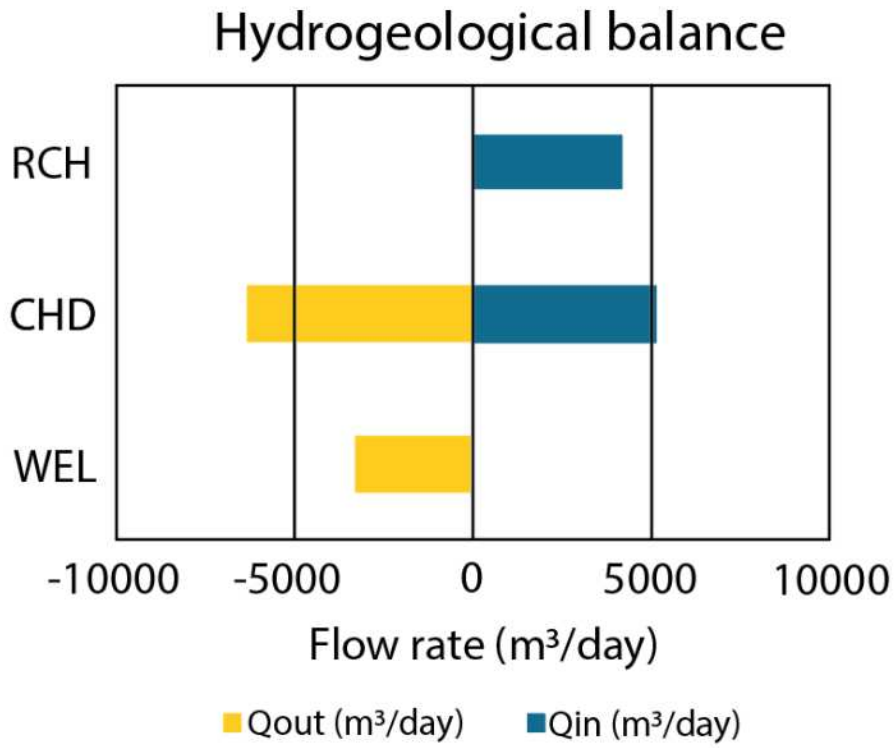

Figure 23. The simulated hydrogeological balance of Capoterra Plain shows a difference of 0.15 % between the in and out flow rate. The in flow rate is linked to the recharge (RCH) and to the western Specified-Head (CHD). The out flow rate is related to wells activity and the sea Specified-Head (CHD).

The final output generated by the numerical flow model is the particle tracking data in *forward* mode, which helps identify potential groundwater flow paths. In Figure 24, the particle tracking results are presented for sites 2 and 4, illustrating the flow trajectories of groundwater. These tracks help visualize the movement of water particles through the subsurface, revealing the flow directions and how groundwater might move from one point to another within the aquifer.

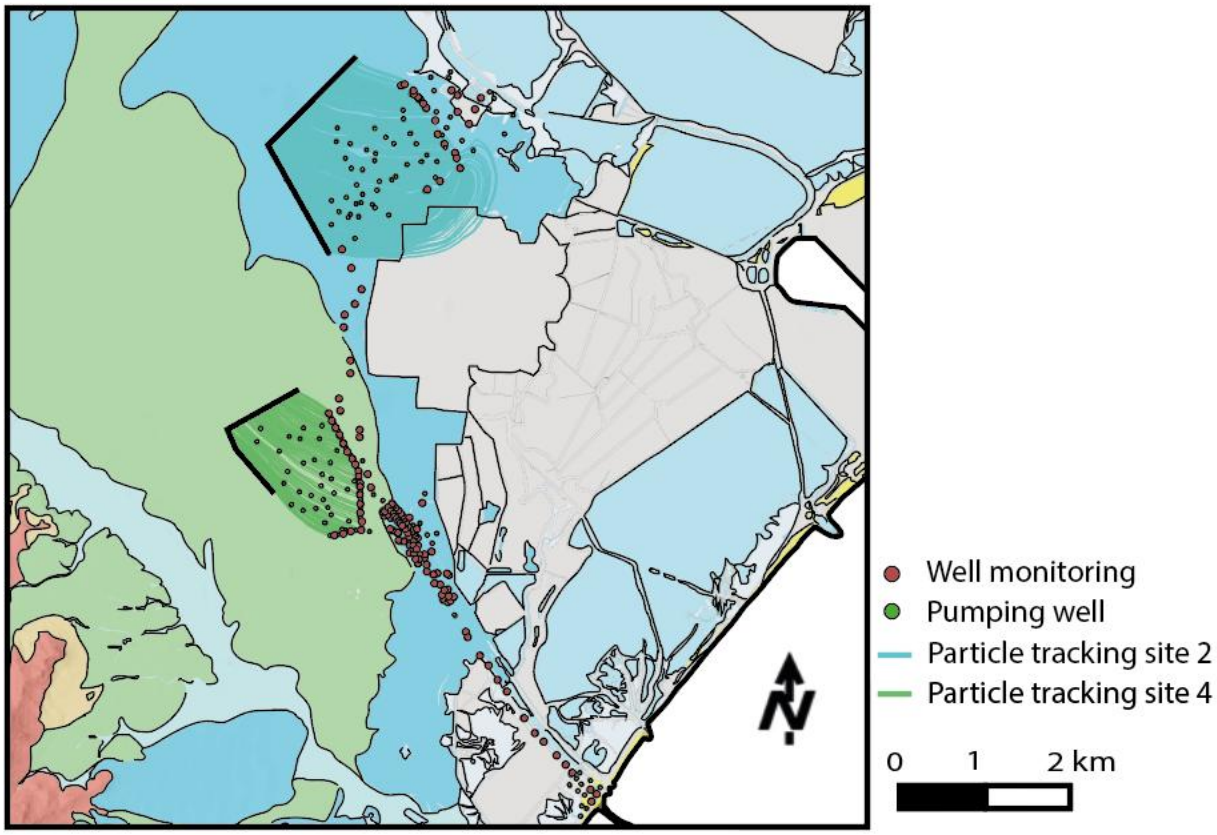

Figure 24. This figure presents the particle tracking in *forward* mode for sites 2 and 4. The particle paths indicate potential groundwater flow directions and trajectories within the aquifer, offering insights into the movement and dispersion of water particles through the subsurface.

5. Discussion

The hydrogeological model developed for the Capoterra Plain has allowed a more accurate representation of the complex interactions between depositional processes and local subsurface heterogeneities, particularly in the neighborhood of industrial sites. This increased precision, compared to previous models such as the one developed for the Arborea area in the western Campidano Plain (Ghiglieri et al., 2016), has highlighted the presence of fine-grained lenses and perched aquifers that significantly influence groundwater flow dynamics.

A comparison with existing literature reveals that, although the transition from multilayer aquifers in mountainous areas to phreatic aquifers in coastal zones is a common feature in other Sardinian coastal plains, the distribution of fine-grained lenses and the presence of perched aquifers seem to be distinctive characteristics of the Capoterra Plain. In particular, the low hydraulic conductivity layer identified at site 5 and the perched aquifer located approximately 10 m below ground level in the central-southern portion of the model, have no direct counterparts in previous studies. These results suggest a higher degree of local lithological heterogeneity, probably associated

with variations in depositional processes, which may also occur in other coastal plains but often remain undetected due to a lack of high-resolution surveys..

In the literature, there are few documented cases where Petrel has been successfully integrated with standard hydrogeological simulation software (e.g., Visual MODFLOW and FEFLOW). This is primarily because Petrel is not directly compatible with these platforms, requiring the development of custom workflows, such as a customised MATLAB script, to facilitate data exchange (Morgan, 2018).

The integration of Petrel for geostatistical modelling, later coupled with ModelMuse for flow numerical modelling, represents a significant methodological advance. Despite some difficulties in data exchange between the two software packages, Petrel and ModelMuse benefit from a large computational capacity and share similarities, such as the use of the same grid type and grid indexing. This facilitated the development of a detailed 3D hydrogeological model capable of capturing subsurface complexity, particularly in industrial areas characterized by high data density. This methodological approach has proven effective in handling heterogeneous datasets and uneven well distribution, filling data gaps through geostatistical interpolation techniques.

Nevertheless, some limitations must be acknowledged. One limitation of this model is the absence of data on the depositional environment. This information is not included in the stratigraphic descriptions, leading to the decision to establish correlations based on the piezometric level. Consequently, the hydrogeological model lacks key depositional context, which could have enhanced the geostatistical distribution of facies and improved the overall accuracy of the model. The absence of geophysical data constrained the direct validation of aquifer and aquitard geometries, increasing uncertainty regarding the lateral continuity of fine-grained lenses and the actual depth of perched levels. Furthermore, the application of stochastic simulation algorithms such as SISIM, while providing a more realistic probabilistic distribution compared to deterministic methods like IK, introduces uncertainty related to variogram selection and geostatistical parameterization.

The analysis of historical groundwater head variations revealed an increase in hydraulic gradient in the eastern part of the plain, suggesting a possible intensification of groundwater abstraction. This phenomenon, which has also been observed in other intensively exploited coastal plains, could potentially heighten the risk of seawater intrusion, warranting further specific investigations and enhanced monitoring efforts.

The primary contribution of this study lies in highlighting the considerable local heterogeneity of aquifers in the Capoterra Plain and proposing an integrated methodological approach combining

geostatistical modeling and hydrogeological simulation. This approach could be successfully extended to other coastal areas characterized by heterogeneous data distribution and complex lithostratigraphic variability.

To further improve the model and reduce uncertainties regarding aquifer geometries, future research should incorporate geophysical surveys, hydrogeochemical analysis and more detailed information on groundwater abstraction activities within the area. Additionally, the development of custom scripts in Matlab or Python could streamline the assignment of hydraulic parameters within ModelMuse grid cells, enhancing the efficiency and reliability of hydrogeological simulations.

6. Conclusions

This study applied a robust and innovative approach to develop a coupled hydrogeological and groundwater flow model using only borehole logs and groundwater head data in clastic aquifers. The methodology was applied in the Capoterra Plain, a coastal aquifer in southern Sardinia (Italy), characterized by a highly heterogeneous distribution of mixed alluvial and marine sediments.

The analysis of Quaternary sediments and their associated depositional environments, based on borehole log data, allowed the construction of stratigraphic cross-sections for the study area. A key innovative aspect of this project was the use of Petrel, a software originally developed for Oil & Gas geological model, to create the hydrogeological model for environmental purposes. Specifically, Petrel was used to define the surfaces delimiting aquifer system units and to distribute borehole log data within the hydrogeological model through geostatistical simulations. To preserve the heterogeneity of the aquifer, granulometry percentages, derived from lithological log descriptions, were distributed nested to the facies model. Subsequently, the hydraulic conductivity distribution was set up using a bivariate algorithm.

Following the hydrogeological modeling phase, ModelMuse was employed to implement and run the numerical groundwater flow model, incorporating the hydrogeological framework previously generated in Petrel. After the definition of the boundary conditions, the model was calibrated through a trial-and-error procedure, yielding a strong agreement between observed and simulated groundwater heads. This validated the coupled hydrogeological and flow model. The calibration process also highlighted the critical role of fine sediment layers in influencing groundwater flow dynamics, emphasizing the complexity of the system.

The primary scientific contribution of this study lies in improving the understanding of the hydrogeological structure of the Capoterra Plain. The research identified the presence and spatial distribution of fine-grained layers that significantly affect groundwater flow patterns. These findings provide a more accurate representation of the aquifer system compared to previous models.

Methodologically, this study demonstrated the successful integration of Petrel and ModelMuse for hydrogeological modeling—an approach that remains relatively rare in the field. The use of Petrel allowed the development of a detailed hydrogeological model of the study area, while ModelMuse has adequately represented the natural hydrogeological phenomena. This combined approach offered a valuable solution for developing hydrogeological models in areas with irregular data distribution and complex sedimentary environments.

In practical terms, the developed model provided a robust and innovative foundation for assessing the hydrogeological balance of the Capoterra Plain and supporting more effective management of groundwater extractions. The results can contribute to mitigate the risk of over-exploitation, optimizing groundwater resource management. Future research could enhance the model by integrating geophysical data, hydrogeochemical analysis and extending the monitoring network, thereby improving the representation of boundaries condition and recharge areas. Overall, this work has contributed to both the understanding of the Capoterra Plain's hydrogeology and the development of modeling techniques applicable to other complex aquifer systems.

References

1. Al-Baldawi, B. A. (2015). Building a 3D geological model using petrel software for Asmari reservoir, south eastern Iraq. Iraqi Journal of Science, 1750-1762.
2. Alvarez, W. (1972). Rotation of the Corsica–Sardinia microplate. Nature Physical Science, 235(58), 103-105.
3. Anderson, M. P., Woessner, W. W., & Hunt, R. J. (2015). Applied groundwater modeling: simulation of flow and advective transport. Academic press.
4. Ardau F, Barbieri G, Barrocu G, Pirastru E (1997) Application of radioisotope techniques to control flow process during artificial coastal aquifer recharge. Proceedings of Application of Isotope Techniques to Investigate Groundwater Pollution, Vienna, 2–5 December 1997.
5. Arthaud, F., & Matte, P. (1977). Late Paleozoic strike-slip faulting in southern Europe and northern Africa: Result of a right-lateral shear zone between the Appalachians and the Urals. Geological society of America bulletin, 88(9), 1305-1320.
6. Balia R, Boi A, Deidda GP, Marchisio M, Sambuelli L (1994) Electrical and I.P. survey in a coastal area west of Cagliari (Southern Sardinia). Proceedings of the 13th Salt Water Intrusion Meeting, Cagliari, 5–10 June 1994
7. Balia, R., Ardau, F., Barrocu, G., Gavaudò, E., & Ranieri, G. (2009). Assessment of the Capoterra coastal plain (southern Sardinia, Italy) by means of hydrogeological and geophysical studies. Hydrogeology journal, 17(4), 981.
8. Barazzuoli, P., Nocchi, M., Rigati, R., & Salleolini, M. (2008). A conceptual and numerical model for groundwater management: a case study on a coastal aquifer in southern Tuscany, Italy. Hydrogeology Journal, 8(16), 1557-1576.
9. Barca S., Melis E., Annino E., Cincotti F., Ulzega A., Orrù P. & Pintus C. (2005) - Note illustrative della Carta Geologica d'Italia 1:50.000 "Foglio 557 - Cagliari". ISPRA-Servizio Geologico d'Italia.
10. Barfod, A. A., Møller, I., Christiansen, A. V., Høyer, A. S., Hoffimann, J., Straubhaar, J., & Caers, J. (2018). Hydrostratigraphic modeling using multiple-point statistics and airborne transient electromagnetic methods. Hydrology and Earth System Sciences, 22(6), 3351-3373.
11. Barroccu, G., Ghiglieri, G., Uras, G., 1995. Intrusione salina e vulnerabilità degli acquiferi costieri nella piana di Oristano (Sardegna centro-occidentale) [Seawater intrusion and vulnerability of coastal aquifers in the Oristano plain (central and western Sardinia)]. Convegno Gestione Irrigua in Ambiente Mediterraneo, Oristano, Italy. (Technical report, unpublished).

12. Barrocu G, Fidelibus MD, Sciabica MG, Uras G (1994) Hydrogeologica land hydrogeochemical study of saltwater intrusion in the Capoterra coastal aquifer system (Sardinia). Proceedings of the 13th Salt Water Intrusion Meeting, Cagliari, 5–10 June 1994.
13. Barrocu G, Muscas L, Sciabica MG (2004) Geographic information systems and modelling of saltwater intrusion in the Capoterra Alluvial Plain (Sardinia-Italy). In: Cheng AHD, Ouazar D (eds) Coastal aquifer management, monitoring, modelling, and case studies. Lewis, Boca Raton.
14. Barrocu, G., Sciabica, M. G., Uras, G., Cortis, A., & Vernier, E. (1997, November). Saltwater intrusion and artificial recharge modelling in the coastal aquifer system of Capoterra (Southern Sardinia). In Proc. Int. Conf. on Water Problems in the Mediterranean Countries, Near East University Civil Engineering Department Nicosia (pp. 2-1001).
15. Bellotti, P. (2000). Il modello morfo-sedimentario dei maggiori delta tirrenici italiani. *Bollettino-Societa Geologica Italiana*, *119*(3), 777-792.
16. Beven, K. (2002). Towards an alternative blueprint for a physically based digitally simulated hydrologic response modelling system. Hydrological processes, 16(2), 189-206.
17. Biddau, R., & Cidu, R. (2016). Groundwater contamination: environmental issues and case studies in Sardinia (Italy). Threats to the Quality of Groundwater Resources: Prevention and Control, 53-76.
18. Brassington, F. C., & Younger, P. L. (2010). A proposed framework for hydrogeological conceptual modelling. Water and Environment Journal, 24(4), 261-273.
19. Cappelli B., Carmignani L., Castorina F., Di Pisa A., Oggiano G. & Petrini R. (1992) - A Hercynian suture zone in Sardinia: geological and geochemical evidence. Geodinamica Acta: 5, 101-118, Paris.
20. Carmignani L, Oggiano G, Barca S, Conti P, Salvadori I, Eltrudis A, Funedda A, Pasci S (2001) Geologia della Sardegna. Note illustrative della Carta Geologica della Sardegna a scala 1:200.000 [Geology of Sardinia: notes on the geological map of Sardinia on the scale of 1:200.000]. In: Memorie Descrittive della Carta Geologica d'Italia 60, Istituto Poligrafico e Zecca dello Stato, Rome.
21. Carmignani, L., Carosi, R., Di Pisa, A., Gattiglio, M., Musumeci, G., Oggiano, G., & Carlo Pertusati, P. (1994). The hercynian chain in Sardinia (Italy). Geodinamica Acta, 7(1), 31-47.
22. Carmignani, L., Decandia, F. A., Disperati, L., Fantozzi, P. L., Lazzarotto, A., Liotta, D., & Oggiano, G. (1995). Relationships between the Tertiary structural evolution of the Sardinia-Corsica-Provençal Domain and the Northern Apennines. Terra Nova, 7(2), 128-137.

23. Carmignani, L., Funedda, A., Oggiano, G., & Pasci, S. (2004). Tectono-sedimentary evolution of southwest Sardinia in the Paleogene: Pyrenaic or Apenninic Dynamic? Geodinamica Acta, 17(4), 275-287.
24. Carmignani, L., Oggiano, G., Funedda, A., Conti, P., & Pasci, S. (2016). The geological map of Sardinia (Italy) at 1: 250,000 scale. Journal of Maps, 12(5), 826-835.
25. Carosi, R., Montomoli, C., Tiepolo, M., & Frassi, C. (2012). Geochronological constraints on post-collisional shear zones in the Variscides of Sardinia (Italy). Terra Nova, 24(1), 42-51.
26. Carta Geologica D'Italia, Foglio 556. Available online: https://www.isprambiente.gov.it/Media/carg/556_ASSEMINI/Foglio.html (accessed on 20 November 2023).
27. Carta Geologica D'Italia, Foglio 557. Available online: https://www.isprambiente.gov.it/Media/carg/557_CAGLIARI/Foglio.html (accessed on 20 November 2023).
28. Carta Geologica D'Italia, Foglio 565. Available online: https://www.isprambiente.gov.it/Media/carg/565_CAPOTERRA/Foglio.html (accessed on 20 November 2023).
29. Carta Geologica D'Italia, Foglio 565. Available online: https://www.isprambiente.gov.it/Media/carg/note_illustrative/565_Capoterra.pdf (accessed on 20 November 2023)
30. Carta Geologica D'Italia, Foglio 566. Available online: https://www.isprambiente.gov.it/Media/carg/566_PULA/Foglio.html (accessed on 20 November 2023).
31. Casini, L., Cuccuru, S., Maino, M., Oggiano, G., & Tiepolo, M. (2012). Emplacement of the Arzachena Pluton (Corsica–Sardinia Batholith) and the geodynamics of incoming Pangaea. Tectonophysics, 544, 31-49.
32. Casini, L., Cuccuru, S., Puccini, A., Oggiano, G., & Rossi, P. (2015). Evolution of the Corsica–Sardinia Batholith and late-orogenic shearing of the Variscides. Tectonophysics, 646, 65-78.
33. Casini, L., Funedda, A., & Oggiano, G. (2010). A balanced foreland–hinterland deformation model for the Southern Variscan belt of Sardinia, Italy. Geological Journal, 45(5-6), 634-649.
34. Casini, L., Puccini, A., Cuccuru, S., Maino, M., & Oggiano, G. (2013). GEOTHERM: A finite difference code for testing metamorphic P–T–t paths and tectonic models. Computers & Geosciences, 59, 171-180.

35. Cassinis, G., Durand, M., & Ronchi, A. (2003). Permian-Triassic continental sequences of Northwest Sardinia and South Provence: stratigraphic correlations and palaeogeographical implications. Bollettino della Società Geologica Italiana, 2(119), e129.
36. Casula, G., Cherchi, A., Montadert, L., Murru, M., & Sarria, E. (2001). The Cenozoic graben system of Sardinia (Italy): geodynamic evolution from new seismic and field data. Marine and petroleum geology, 18(7), 863-888.
37. Cavinato A. (1939) - Nuovi risultati ed osservazioni nel rilievo geologico del Foglio Mandas. Atti Acc. Lincei, s. 6, 29, Roma.
38. Cherchi A. & Montadert L. (1982) - The oligo-miocene rift of Sardinia and the early history of the Western Mediterranean basin. Nature, 298, 736-739.
39. Cherchi A. & Montadert L. (1984) - Il sistema di rifting oligo-miocenico del Mediterraneo occidentale e sue conseguenze paleogeografiche sul Terziario sardo. Mem. Soc. Geol. It.: 24, 387-400, Roma.
40. Cherchi A. & Murru M. (1985) - Plio-Quaternary Campidano graben. 19th European Micropaleontological Colloquium-Sardinia, Cagliari University, 105-112.
41. Cherchi, A., & Montadert, L. (1982). Oligo-Miocene rift of Sardinia and the early history of the western Mediterranean basin. Nature, 298(5876), 736-739.
42. Chiang, W. H., & Kinzelbach, W. (2005). 3D-groundwater modeling with PMWIN (p. 411). Berlin: Springer.
43. Chicco, J.M.; Fonte, L.; Mandrone, G.; Tartaglino, A.; Vacha, D. Hybrid (Gas and Geothermal) greenhouse simulations aimed at optimizing investment and operative costs: A case study in NW Italy. *Energies* **2023**, *16*, 3931.
44. Chicco, J.M.; Mandrone, G. Modelling the Energy Production of a Borehole Thermal Energy Storage (BTES) System. *Energies* **2022**, *15*, 9587.
45. Cidu, R., Biddau, R., & Fanfani, L. (2009). Impact of past mining activity on the quality of groundwater in SW Sardinia (Italy). Journal of Geochemical Exploration, 100(2-3), 125-132.
46. Civita M., 2001. Aspetti metodologici nella realizzazione delle Carte di Vulnerabilità degli acquiferi all'inquinamento. In: Le risorse idriche sotterranee: conoscerle per proteggerle, Venezia, 14-15 novembre 2001.
47. Cocco, F., Oggiano, G., Funedda, A., Loi, A., & Casini, L. (2018). Stratigraphic, magmatic and structural features of Ordovician tectonics in Sardinia (Italy): a review. Journal of Iberian Geology, 44, 619-639.

48. Cocherie, A., Rossi, P., Fanning, C. M., & Guerrot, C. (2005). Comparative use of TIMS and SHRIMP for U–Pb zircon dating of A-type granites and mafic tholeiitic layered complexes and dykes from the Corsican Batholith (France). *Lithos*, *82*(1-2), 185-219.
49. Consorzio Industriale Provinciale di Cagliari (CACIP). Available online: https://cacip.portaletrasparenza.net/it/trasparenza/pianificazione-e-governo-del-territorio/piano-di-caratterizzazione-dell-agglomerato-di-macchiareddu.html (accessed on 15 October 2022).
50. Dansgaard, W., Johnsen, S. J., Clausen, H. B., Dahl-Jensen, D., Gundestrup, N. S., Hammer, C. U., ... & Bond, G. (1993). Evidence for general instability of past climate from a 250-kyr ice-core record. *nature*, *364*(6434), 218-220.
51. Dati Meteorologici e Agrometeorologici delle Reti di Stazioni ARPAS. Available online: https://dati-annuali-rete-arpas-2021-arpas.hub.arcgis.com/pages/dati_meteo_2016_2022 (accessed on 15 February 2024).
52. Del Moro A., Di Simplicio P., Ghezzo C., Guasparri G., Rita F. & Sabatini G. (1975) - Radiometric data and intrusive sequence in the Sardinian Batholith. N. Jb. Miner. Abh., 126: 28-44, Stuttgart.
53. Di Salvo, C., Di Luzio, E., Mancini, M., Moscatelli, M., Capelli, G., Cavinato, G. P., & Mazza, R. (2012). GIS-based hydrostratigraphic modeling of the city of Rome (Italy): analysis of the geometric relationships between a buried aquifer in the Tiber Valley and the confining hydrostratigraphic complexes. Hydrogeology Journal, 20(8), 1549.
54. Di Vincenzo, G., Carosi, R., & Palmeri, R. (2004). The relationship between tectono-metamorphic evolution and argon isotope records in white mica: constraints from in situ 40Ar–39Ar laser analysis of the Variscan basement of Sardinia. Journal of Petrology, 45(5), 1013-1043.
55. Edel, J. B., Casini, L., Oggiano, G., Rossi, P., & Schulmann, K. (2014). Early Permian 90° clockwise rotation of the Maures–Estérel–Corsica–Sardinia block confirmed by new palaeomagnetic data and followed by a Triassic 60° clockwise rotation.
56. El-Azhari A. et al., Analyses of groundwater level in a data-scarce region based on assessed precipitation products and machine learning, Groundwater for Sustainable Development, Volume 26, 2024, 101299, https://doi.org/10.1016/j.gsd.2024.101299.
57. Emery, X., & Peláez, M. (2011). Assessing the accuracy of sequential Gaussian simulation and cosimulation. Computational Geosciences, 15, 673-689.
58. Enemark, T., Peeters, L. J., Mallants, D., & Batelaan, O. (2019). Hydrogeological conceptual model building and testing: A review. Journal of Hydrology, 569, 310-329.

59. Ferre, E. C., & Leake, B. E. (2001). Geodynamic significance of early orogenic high-K crustal and mantle melts: example of the Corsica Batholith. *Lithos*, *59*(1-2), 47-67.
60. Frau F. (1994) - A new hydrothermal manifestation in the Campidano graben, Italy: the Su Campu borehole (Monastir). Miner. Petrogr. Acta. 37, 155-162.
61. Funedda A., Carmignani L., Pasci S., Patta E. D., Uras V. e Conti P. (2009) - F° 556 "Assemini". Note illustrative della carta geologica d'Italia in scala 1:50.000. APAT-Servizio Geologico d'Italia, Roma.
62. Funedda, A., Oggiano, G., & Pasci, S. (2000). The Logudoro Basin; a key area for the Tertiary tectono-sedimentary evolution of north Sardinia. Bollettino della Società Geologica Italiana, 119(1), 31-38.
63. Gaggero, L., Gretter, N., Langone, A., & Ronchi, A. (2017). U–Pb geochronology and geochemistry of late Palaeozoic volcanism in Sardinia (southern Variscides). Geoscience Frontiers, 8(6), 1263-1284.
64. Gaggero, L., Oggiano, G., Funedda, A., & Buzzi, L. (2012). Rifting and arc-related early Paleozoic volcanism along the north Gondwana margin: geochemical and geological evidence from Sardinia (Italy). *The Journal of Geology*, *120*(3), 273-292.
65. Ghiglieri, G., Carletti, A., Da Pelo, S., Cocco, F., Funedda, A., Loi, A., ... & Pittalis, D. (2016). Three-dimensional hydrogeological reconstruction based on geological depositional model: a case study from the coastal plain of Arborea (Sardinia, Italy). Engineering Geology, 207, 103-114.
66. Godio A, Sambuelli L, Barrocu G, Ranieri G (1999) Applicaciòn del método TDEM para la delimitaciòn de la intrusiòn salina en el acuìfero costero de Capoterra (Cerdeña Sud-Occidental) [TDEM method application for delineating salt-water intru sion in the coastal aquifer of Capoterra (south-western Sardinia)]. In: Proceedings of Jornadas sobre actualidad de las técnicas geofisicas aplicadas en hidrogeologìa, Granada, 1999
67. Gong, W., Zhao, C., Juang, C. H., Zhang, Y., Tang, H., & Lu, Y. (2021). Coupled characterization of stratigraphic and geo-properties uncertainties–a conditional random field approach. Engineering Geology, 294, 106348.
68. Goovaerts, P. (1997). Geostatistics for natural resources evaluation (Vol. 483). Oxford University Press.
69. Heinz, J., & Aigner, T. (2003). Hierarchical dynamic stratigraphy in various Quaternary gravel deposits, Rhine glacier area (SW Germany): implications for hydrostratigraphy. International Journal of Earth Sciences, 92, 923-938.

70. Hudon-Gagnon, E., Chesnaux, R., Cousineau, P. A., & Rouleau, A. (2015). A hydrostratigraphic simplification approach to build 3D groundwater flow numerical models: example of a Quaternary deltaic deposit aquifer. Environmental Earth Sciences, 74, 4671-4683.
71. Irace, A., Clemente, P., Piana, F., De Luca, D. A., Polino, R., Violanti, D., ... & Petricig, M. (2010). Hydrostratigraphy of the late Messinian-Quaternary basins in the southern Piedmont (northwestern Italy). Mem. Descr. Carta Geologica It, 90, 133-152.
72. Istituto Superiore per la Protezione e la Ricerca Ambientale (ISPRA). Available online: https://sgi2.isprambiente.it/viewersgi2/ (accessed on 05 June 2022)
73. Kinzelbach, W. (1986). Groundwater modelling: An introduction with sample programs in BASIC. Elsevier.
74. Klingbeil, R., Kleineidam, S., Asprion, U., Aigner, T., & Teutsch, G. (1999). Relating lithofacies to hydrofacies: outcrop-based hydrogeological characterisation of Quaternary gravel deposits. Sedimentary Geology, 129(3-4), 299-310.
75. Lal, A., & Datta, B. (2020). Performance evaluation of homogeneous and heterogeneous ensemble models for groundwater salinity predictions: A regional-scale comparison study. Water, Air, & Soil Pollution, 231(6), 320.
76. Lamarmora A. (1857) - Voyage en Sardaigne: Troisième Partie. Description Géologique et Paléontologique. Bocca Impr. Royale, 2 vol., Torino.
77. Langevin, C. D., Hughes, J. D., Banta, E. R., Niswonger, R. G., Panday, S., & Provost, A. M. (2017). Documentation for the MODFLOW 6 groundwater flow model (No. 6-A55). US Geological Survey.
78. Lecca L., Lonis R., Luxoro S., Melis E., Secchi F. & Brotzu P. (1997) - Oligo-Miocene volcanic sequences and rifting stages in Sardinia: a review. Period. Min.: 66, 7-61, Roma.
79. Lee, J. Y., Moon, S. H., & Yun, S. T. (2010). Contamination of groundwater by arsenic and other constituents in an industrial complex. Environmental Earth Sciences, 60, 65-79.
80. Li, P., Karunanidhi, D., Subramani, T., & Srinivasamoorthy, K. (2021). Sources and consequences of groundwater contamination. Archives of environmental contamination and toxicology, 80, 1-10.
81. Macdonald, R. W., Harner, T., & Fyfe, J. (2005). Recent climate change in the Arctic and its impact on contaminant pathways and interpretation of temporal trend data. Science of the total environment, 342(1-3), 5-86.
82. Mackay, D. M., Roberts, P. V., & Cherry, J. A. (1985). Transport of organic contaminants in groundwater. Environmental science & technology, 19(5), 384-392.

83. Madsen, R. B., Høyer, A. S., Andersen, L. T., Møller, I., & Hansen, T. M. (2022). Geology-driven modeling: A new probabilistic approach for incorporating uncertain geological interpretations in 3D geological modeling. Engineering Geology, 309, 106833.
84. Madsen, R. B., Kim, H., Kallesøe, A. J., Sandersen, P. B., Vilhelmsen, T. N., Hansen, T. M., ... & Hansen, B. (2021). 3D multiple-point geostatistical simulation of joint subsurface redox and geological architectures. Hydrology and Earth System Sciences, 25(5), 2759-2787.
85. Maxia C., Palmerini V., Ulzega A. & Barca S. (1970) - Geomorfologia e sedimentologia del settore sud-orientale del Campidano (Sardegna meridionale). Boll. Soc. Geol. It., 89, 567-597.
86. Moretti A. (1953) - Problemi teorici e pratici della geologia del Campidano. Boll. Serv. Geol. It. 74, 1, Roma.
87. Morgan, S. E. (2018). Investigating the role of buried valley aquifer systems in the regional hydrogeology of the Central Peace Region in Northeast British Columbia.
88. Mukherjee, A., Fryar, A. E., & Howell, P. D. (2007). Regional hydrostratigraphy and groundwater flow modeling in the arsenic-affected areas of the western Bengal basin, West Bengal, India. Hydrogeology Journal, 15, 1397-1418.
89. Murru M. & Salvadori A. (1990) - Ricerche stratigrafiche sul bacino paleogenico del Sulcis (Sardegna sud-occidentale). Geologica Romana: 26, 149-165, Roma.
90. Napoli R., Vanino S. Valutazione del rischio di salinizzazione dei suoli e di intrusione marina nelle aree costiere delle regioni meridionali in relazione agli usi irrigui. INEA, 2011, 40-51.
91. Neuman, S. P., Wierenga P. J., & Nicholson, T. J. (2003). A comprehensive strategy of hydrogeologic modeling and uncertainty analysis for nuclear facilities and sites (p. 311). Division of Systems Analysis and Regulatory Effectiveness, Office of Nuclear Regulatory Research, US Nuclear Regulatory Commission.
92. Oggiano, G., Funedda, A., Carmignani, L., & Pasci, S. (2009). The Sardinia-Corsica microplate and its role in the Northern Apennine Geodynamics: new insights from the Tertiary intraplate strike-slip tectonics of Sardinia. Italian Journal of Geosciences, 128(2), 527-539.
93. Orsini, J. (1976). Les granitoides hercyniens corso-sardes; mise en evidence de deux associations magmatiques. *Bulletin de la Société Géologique de France*, *7*(5), 1203-1206.
94. Pala A (1983) Studio geoidrologico della piana di Capoterra (Sardegna Meridionale) [Hydrogeological study of the Capoterra plain (southern Sardinia)]. Rend Seminar Facoltà Sci Univ Cagliari 53:171–196.
95. Pala A, Pecorini G, Porcu A, Serra S (1982) Schema geologico strutturale della Sardegna [Geological and structural scheme of Sardinia]. In: Ricerche Geotermiche in Sardegna con particolare riferimento al Graben del Campidano, CNR-PFE-SPEG-RF-10, CNR, Rome.

96. Paquette, J. L., Ménot, R. P., Pin, C., & Orsini, J. B. (2003). Episodic and short-lived granitic pulses in a post-collisional setting: evidence from precise U–Pb zircon dating through a crustal cross-section in Corsica. *Chemical Geology*, *198*(1-2), 1-20.
97. Pasci S. (1997) - Tertiary transcurrent tectonics of North-Central Sardinia. Bull. Soc. Géol. France: 168, 301-312, Paris.
98. Pecorini G. & Pomesano Cherchi A. (1969) - Ricerche geologiche e biostratigrafiche sul Campidano meridionale (Sardegna). Mem. Soc. Geol. It., 8, 421-451.
99. Pomesano Cherchi A. (1967) - Studio biostratigrafico del Miocene della Sardegna centro-meridionale (Campidano-Marmilla orientale. Sarcidano). Atti IV Convegno Neogene Mediterraneo, Giorn. Geol. 35, Bologna.
100. Pranzini, E. (2004). La forma delle coste. *Geomorfologia costiera impatto antropico e difesa dei litorali. Zanichelli*.
101. Pugin, A. J. M., Oldenborger, G. A., Cummings, D. I., Russell, H. A., & Sharpe, D. R. (2014). Architecture of buried valleys in glaciated Canadian Prairie regions based on high resolution geophysical data. Quaternary Science Reviews, 86, 13-23.
102. Refsgaard, J. C., Van der Sluijs, J. P., Brown, J., & Van der Keur, P. (2006). A framework for dealing with uncertainty due to model structure error. Advances in water resources, 29(11), 1586-1597.
103. Ronchi, A., Sarria, E., & Broutin, J. (2008). The “Autuniano Sardo”: basic features for a correlation through the Western Mediterranean and Paleoeurope. Bollettino della Società Geologica Italiana, 127(3), 655-681.
104. Rossi P., Oggiano G. & Cocherie, A. (2009) - A restored section of the "southern Variscan realm" across the Corsica-Sardinia microcontinent. Comptes Rendu Gèoscience. 341, 2-3.
105. Rossi, P., & Cocherie, A. (1991). Genesis of a Variscan batholith: Field, petrological and mineralogical evidence from the Corsica-Sardinia batholith. *Tectonophysics*, *195*(2-4), 319-346.
106. Schlumberger (2010): Petrel Seismic-to-Evaluation Software, Version 2010
107. Sciabica MG (1994) Validazione dei modelli concettuali e matematici degli acquiferi con i dati idrogeologici ed idrogeochimici delle reti di monitoraggio [Conceptual and mathematical aquifer model validation by means of hydrogeological and hydrochemical monitoring network data]. PhD Thesis, Central National Library of Florence, Italy, online catalogue code BN 97-724T, 179 pp.

108. Sciabica, M. G. (1994). *Validazione dei modelli concettuali e matematici degli acquiferi con i dati idrogeologici ed idrogeochimici delle reti di monitoraggio [Conceptual and mathematical aquifer model validation by means of hydrogeological and hydrochemical monitoring network data]* (Doctoral dissertation, University of Cagliari).

109. Singh, A. (2014). Groundwater resources management through the applications of simulation modeling: A review. Science of the Total Environment, 499, 414-423.

110. Smaoui, H., Zouhri, L., Ouahsine, A., & Carlier, E. (2012). Modelling of groundwater flow in heterogeneous porous media by finite element method. Hydrological Processes, 26(4), 558-569.

111. Soddu, S., Barrocu, G., 2006. Contaminazione salina degli acquiferi nell'area della Bonifica di Arborea (Sardegna centro-occidentale) (Aquifers salinization in the Arborea area (central and western Sardinia)). Rivista IGEA — Ingegneria e Geologia degli Acquiferi Vol. 21, pp. 103–112.

112. Speranza, F., Villa, I. M., Sagnotti, L., Florindo, F., Cosentino, D., Cipollari, P., & Mattei, M. (2002). Age of the Corsica–Sardinia rotation and Liguro–Provençal Basin spreading: new paleomagnetic and Ar/Ar evidence. Tectonophysics, 347(4), 231-251.

113. Stafleu, J., Maljers, D., Gunnink, J. L., Menkovic, A., & Busschers, F. S. (2011). 3D modelling of the shallow subsurface of Zeeland, the Netherlands. Netherlands Journal of Geosciences, 90(4), 293-310.

114. Stori, L., Ronchi, A., López-Gómez, J., Márquez-Aliaga, A., Ros-Franch, S., Goy, A., ... & Martín-Chivelet, J. (2023). Middle Triassic (Muschelkalk) transgression in the West Tethys: biostratigraphic evidence from Sardinia (Italy). Palaeoworld.

115. Tiwari, A. K., Orioli, S., & De Maio, M. (2019). Assessment of groundwater geochemistry and diffusion of hexavalent chromium contamination in an industrial town of Italy. Journal of contaminant hydrology, 225, 103503.

116. Ulzega, A., & Ozer, A. (1982). Comptes-rendus de l'excursion table ronde sur le Tyrrhénien de Sardaigne. *INQUA Guidebook, INQUA, Cagliari, Italy*.

117. Ulzega, A., Lecca, L., & Leone, F. (1981). Niveaux marins submerges sur la plate-forme continentale de la Sardaigne orientale. In *Rapp. Comm. Inter. Mer Mèdit.,* (Vol. 27, No. 8, pp. 35-36).

118. Vilhelmsen, T. N., Auken, E., Christiansen, A. V., Barfod, A. S., Marker, P. A., & Bauer-Gottwein, P. (2019). Combining clustering methods with MPS to estimate structural uncertainty for hydrological models. Frontiers in Earth Science, 7, 181.

119. von Raumer, J. F., & Stampfli, G. M. (2008). The birth of the Rheic Ocean—Early Palaeozoic subsidence patterns and subsequent tectonic plate scenarios. Tectonophysics, 461(1-4), 9-20.

120. von Raumer, J. F., Stampfli, G. M., & Bussy, F. (2003). Gondwana-derived microcontinents—the constituents of the Variscan and Alpine collisional orogens. Tectonophysics, 365(1-4), 7-22.

121. Weissmann, G. S., Carle, S. F., & Fogg, G. E. (1999). Three-dimensional hydrofacies modeling based on soil surveys and transition probability geostatistics. Water Resources Research, 35(6), 1761-1770.

122. Winston, R. B. (2019). ModelMuse Version 4: A graphical user interface for MODFLOW 6 (No. 2019-5036). US Geological Survey.

123. Wu, Y., Wang, W., Toll, M., Alkhoury, W., Sauter, M., & Kolditz, O. (2011). Development of a 3D groundwater model based on scarce data: the Wadi Kafrein catchment/Jordan. Environmental Earth Sciences, 64, 771-785.

124. Zhao, C., Gong, W., Li, T., Juang, C. H., Tang, H., & Wang, H. (2021). Probabilistic characterization of subsurface stratigraphic configuration with modified random field approach. Engineering Geology, 288, 106138.

Appendix A

Hydrogeological model development

Petrel software 2021 has been used to build 3D model. Petrel is a PC- based workflow application for subsurface interpretation and modeling. Data preparation is the basis for geologic model.

Model Design Workflow (Petrel)

The main steps of building a hydrogeological model using petrel software are:

- Data import.
- Input data editing and quality check (Q.C).
- Well correlation.
- Structural modeling, which includes: simple grid, make horizons and layering.
- Grid editing for data export;
- Property modeling, which includes: scale up well logs, facies modelling and petrophysical modeling.

1. Data import

On this basis of software demand and research area characteristic, the data prepare for this 3D-geological model are well heads, well tops, well logs. The input data is imported from files – on file for each data object (each well). These data include:

1. Well head: include the position of each well in 3-dimentions (x, y and z), and the measured depth along the path.
2. Well tops: Markers representing significant points (well picks) along the well path, normally linked to stratigraphy.
3. Well logs: the data cover facies and grain size percentual values along the well path.

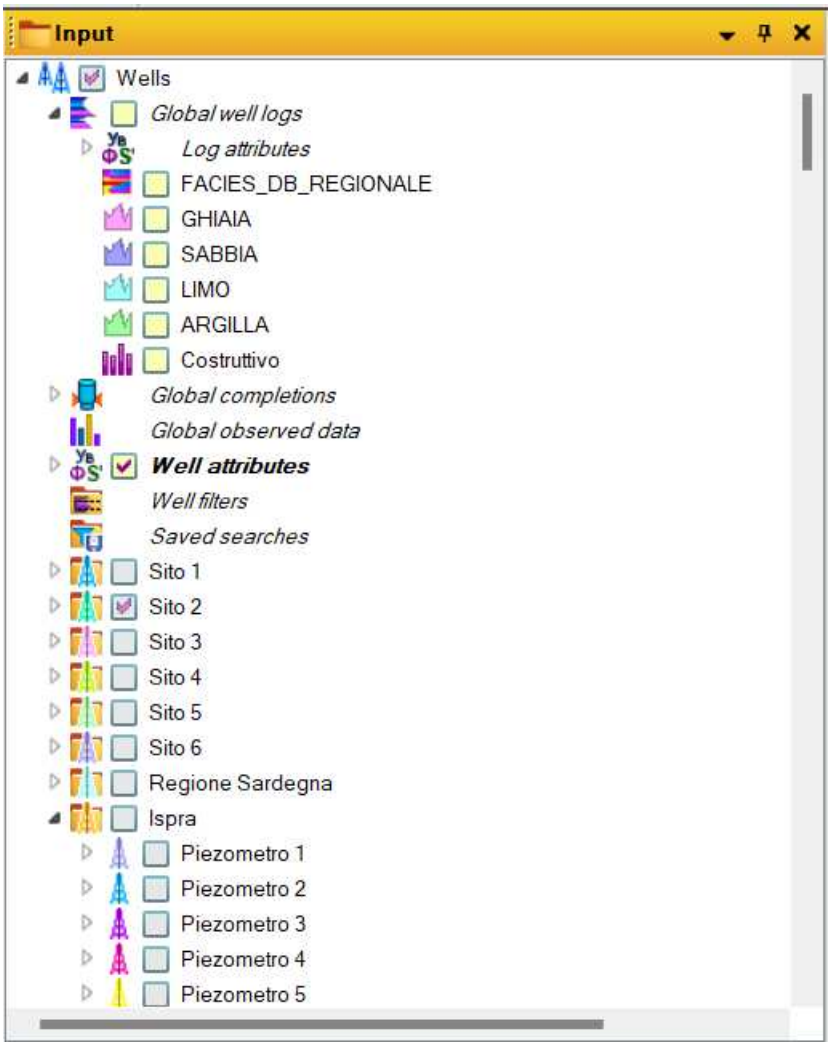

Figure 2. Input visualisation of data on Petrel software.

2. Well correlation

In this study, litho-correlation has been applied as a relatively easy method to give an idea and allow simple visualization of the changes in the thickness and the change of the petrophysical properties (i.e., grain size percentual) of the aquifer system. Borehole log analysis and facies interpretation of the lithological data was carried out and imported on the software. Subsequently, the hydrogeological correlation process was performed (figure 2). Following the data logs, two aquitards were correlated, also considering groundwater head values (figure 2): a shallow aquitard (ca 10 m b.g.l.) locally supporting a perched aquifer, and a second aquitard located about 20 m b.g.l., dividing the phreatic aquifer into two separated portions (a shallow and a deep one, the latter locally and partially confined).

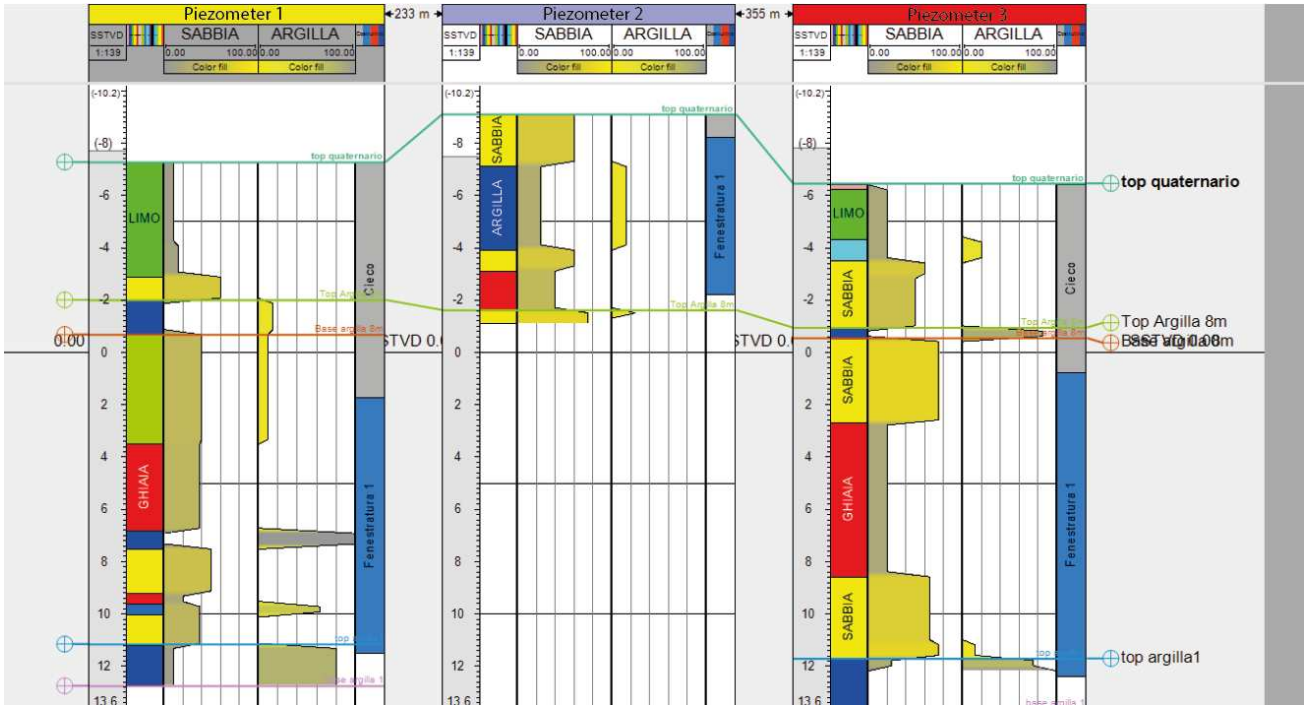

Figure 3. Lithocorrelation of the borehole data. (From left to right, facies well log, sand log, clay log, and constructing well data).

3. Structural modeling

Structural modeling is used for building geological model. It was subdivided into three processes as follows: simple grid, horizons, and vertical layering. All the three operations were performed one after the other to form one single data model. 3D hydrogeological model was built depending on the surfaces created during the lithocorrelation (figure 2).

3.1 3D Grid Construction

A 3D grid construction is the first step to build the 3D model and is a network of horizontal and vertical lines used to describe a 3D geological model. In simple terms, a 3D grid divides a model up into boxes. Each box is called a grid cell and will have a single sediment type, one value of hydraulic conductivity. These are referred to as the cell properties.

3.1.1 Simple grid

Simple grid is the first step of the development of the 3D model grid, where it is defined the top limit and the bottom limit of the model, typically used where fault network is not available and almost regular grid spacing.

The skeleton is a grid consisting of top, mid and base skeleton grids. The grid which used in the study area was represented by 3D grid systems of (50) grid along the X – axis and (50) grid along Y – axis. The size of grid was chosen depending on the area of the field. The result from simple grid is the main skeleton in top, mid and base skeletons as shown in figure 3. This figure shows a 3D grid

or three skeletons of the study area.

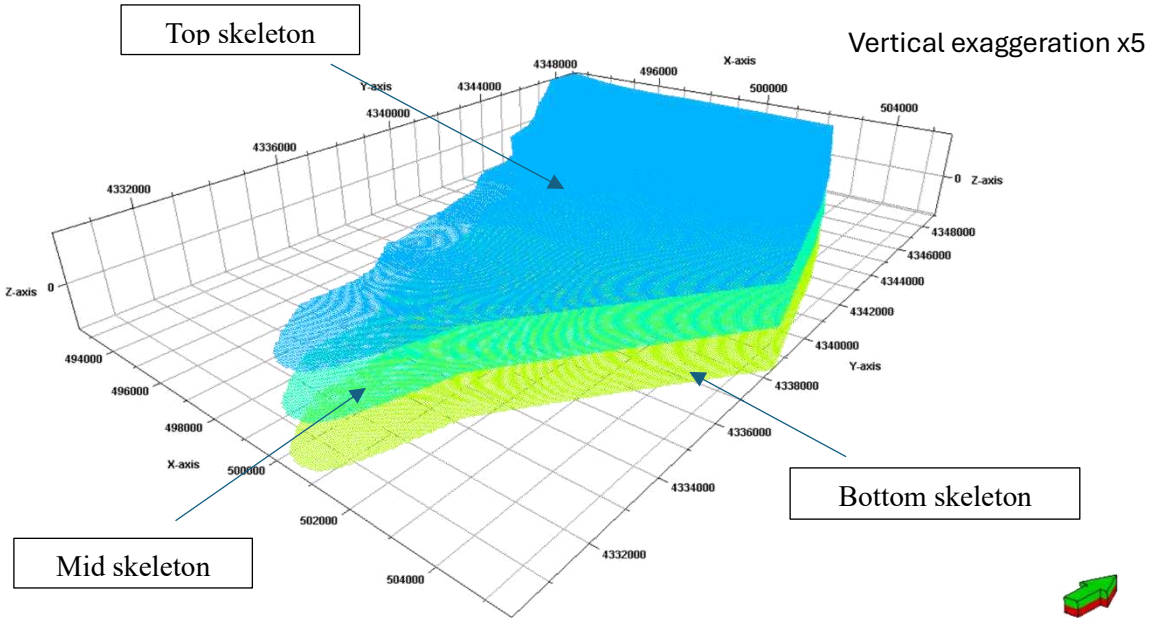

Figure 4. 3D hydrogeological skeleton of the study area.

3.1.2 Grid thickness adaptation

Grid thickness adaptation was necessary because ModelMuse run only for a 3D grid in which each cell has a minimum thickness value. Therefore, in order to incorporate the layers pinch out, the 3D geological grid was modified as follows:

- The fine grid coherent with stratigraphic data, has been used to extract the thickness map for each zone;
- A bulk shift has been applied to allow the grid to generate a continuous layer along the 3D grid as per table below and used as input for the new grid;

3.1.3 Make Horizons and make zones

The final step in structural modeling is to insert the stratigraphic horizons into the 3D geological model. Make horizons process step was used in defining the vertical layering of the 3D grid in Petrel. This present a true 3D approach in the generation of 2D surface, which was gridded in the same process, taking the relationships between the surfaces into account. Figure 4 represents horizons and zones of the main units of the study area.

Vertical exaggeration x10

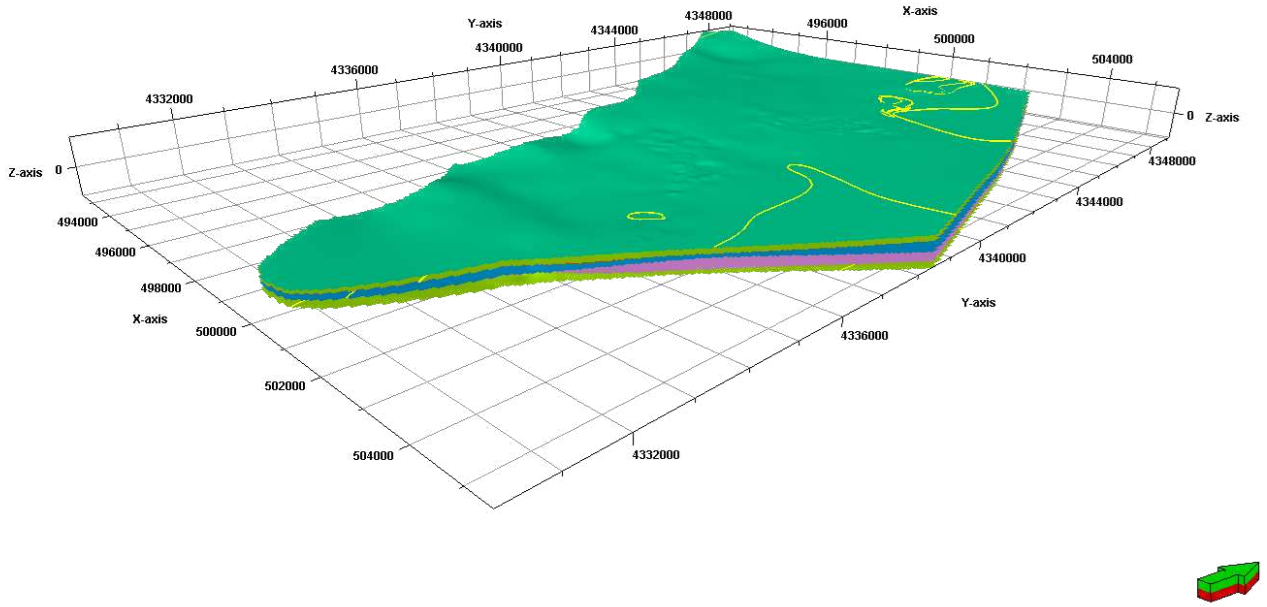

Figure 4. Main horizon of the study area.

3.1.4 Layering

The final step in building the structural framework is to define the thickness and orientation of the layers between horizons of the 3D Grid. These layers in conjunction with the pillars define the cells of the 3D Grid that are assigned attributes during property modeling [7]. Modern geology requires accurate representation of layered volumes. 3D geologic models are increasingly the best method to constrain geology at depth. Each zone of the model has been divided into many layers depending on thickness and petrophysical properties. Each of the two aquitards were divided in one layer because have the same petrophysical properties. The perched aquifer has been divided into 6 layers, while the shallow phreatic aquifer has been divided into 10 layers because the mayor thickness. The deep phreatic aquifer has been divided in just one layer because wasn't the focus of the study (Figure 5).

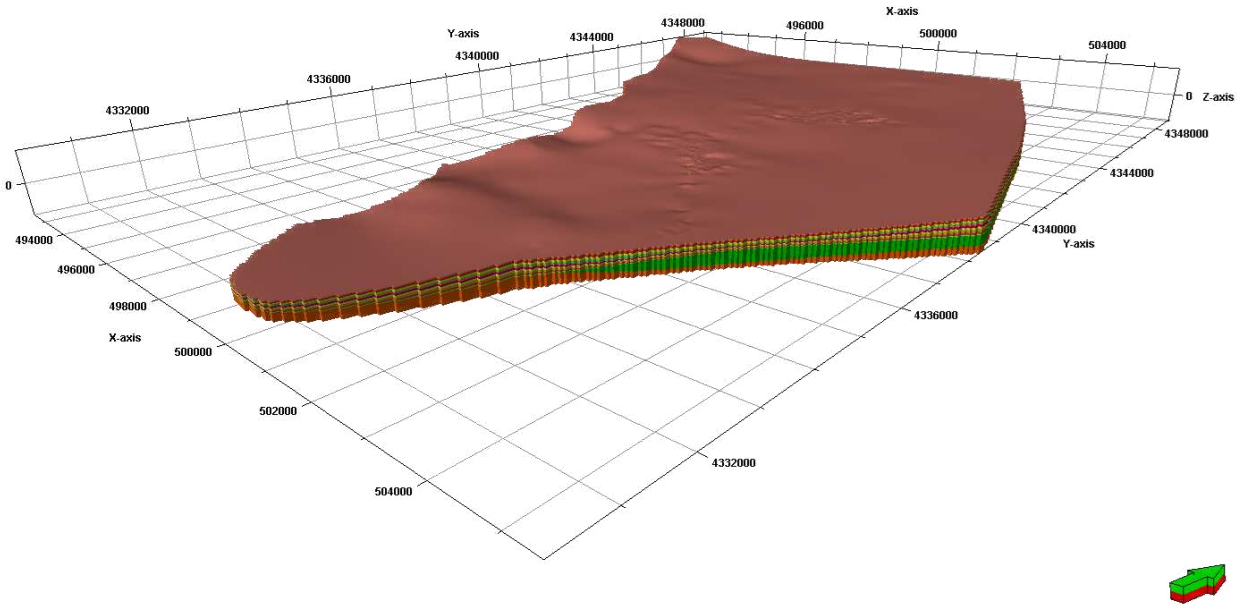

Figure 5. Layering product of the 3D hydrogeological model.

4. Property modelling

The thickness map generated from fine grid, is discretized inside the continuous grid with a cut-off at 0.5m (named Thickness_Zone1_D); afterwards the regions created in this way would be merged in order to create the final grid coherent with the original grid (Zone_D) (Figure 6).

```
Zones_D=If( Zones_hierarchy=0 And Zones_D=0 ,If( Thickness_Zone2_D=1,2 ,Zones_D ) ,Zones_D)
Zones_D=If( Zones_hierarchy=0 And Zones_D=0 ,If( Thickness_Zone3_D=1,3 ,Zones_D ) ,Zones_D)
Zones_D=If( Zones_hierarchy=0 And Zones_D=0 ,If( Thickness_Zone4_D=1,4 ,Zones_D ) ,Zones_D)
Zones_D=If( Zones_hierarchy=0 And Zones_D=0 ,If( Thickness_Zone5_D=1,5 ,Zones_D ) ,Zones_D)
Zones_D=If( Zones_hierarchy=0 And Zones_D=0 ,If( Thickness_Zone6_D=1,6 ,Zones_D ) ,Zones_D)

Zones_D=If( Zones_hierarchy=1 And Zones_D=1 ,2 ,Zones_D)
Zones_D=If( Zones_hierarchy=2 And Zones_D=1 ,3 ,Zones_D)
Zones_D=If( Zones_hierarchy=3 And Zones_D=1 ,4 ,Zones_D)
Zones_D=If( Zones_hierarchy=4 And Zones_D=1 ,5 ,Zones_D)
Zones_D=If( Zones_hierarchy=5 And Zones_D=1 ,6 ,Zones_D)

Zones_D=If( Zones_hierarchy=1 And Zones_D=0 ,If( Thickness_Zone3_D=1,3 ,Zones_D) ,Zones_D)
Zones_D=If( Zones_hierarchy=1 And Zones_D=0 ,If( Thickness_Zone4_D=1,4 ,Zones_D) ,Zones_D)
Zones_D=If( Zones_hierarchy=1 And Zones_D=0 ,If( Thickness_Zone5_D=1,5 ,Zones_D) ,Zones_D)
Zones_D=If( Zones_hierarchy=1 And Zones_D=0 ,If( Thickness_Zone6_D=1,6 ,Zones_D) ,Zones_D)
Zones_D=If( Zones_hierarchy=2 And Zones_D=0 ,If( Thickness_Zone4_D=1,4 ,Zones_D) ,Zones_D)
Zones_D=If( Zones_hierarchy=2 And Zones_D=0 ,If( Thickness_Zone5_D=1,5 ,Zones_D) ,Zones_D)
Zones_D=If( Zones_hierarchy=2 And Zones_D=0 ,If( Thickness_Zone6_D=1,6 ,Zones_D) ,Zones_D)
Zones_D=If( Zones_hierarchy=3 And Zones_D=0 ,If( Thickness_Zone5_D=1,5 ,Zones_D) ,Zones_D)
Zones_D=If( Zones_hierarchy=3 And Zones_D=0 ,If( Thickness_Zone6_D=1,6 ,Zones_D) ,Zones_D)
Zones_D=If( Zones_hierarchy=4 And Zones_D=0 ,If( Thickness_Zone6_D=1,6 ,Zones_D) ,Zones_D)
```

Figure 6. Synthetic zone discretization

Figure 7 shows the modified grid of the 3D hydrogeological model, adapted for following use with ModelMuse. However, to maintain the original model texture, the added thicknesses in the different zones were assigned the code of the preceding layer, indirectly recreating the pinch out closure. This approach maintains consistency with the initial stratigraphic framework, preserving each zone's hydrogeological properties while overcoming the technical limitations of ModelMuse

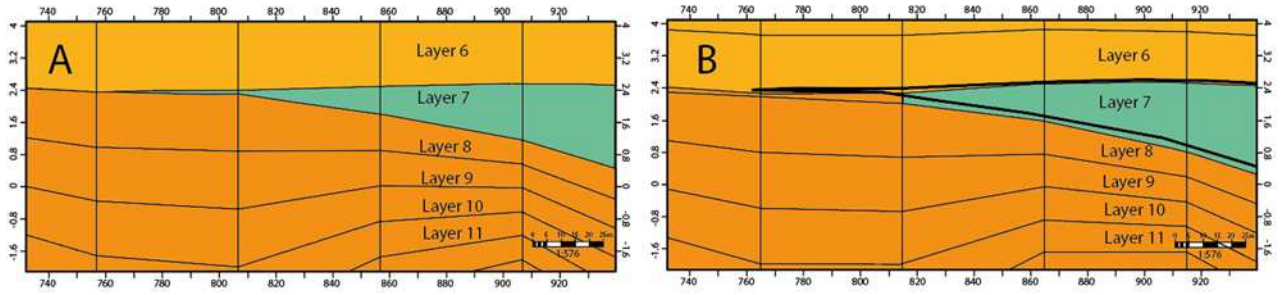

Figure 7. A) The figure A shows the 3D hydrogeological grid created by Petrel where the aquitard layers pinch out. B) The figure B shows the 3D hydrogeological grid modified in order to permit the running of the model on ModelMuse.

Scale up Well logs

The Scale up well logs allowed for the assignment of values to the cells in the 3D grid that are penetrated by the wells. It was carried out for both the facies and the grain size percentual distribution. Each cell gets one value per up scaled log. These cells are later used as a starting point for property modeling (Schlumberger, 2010). There are many statistical methods used to scale up such as (arithmetic, harmonic, ‘’most of’’ and geometric method).

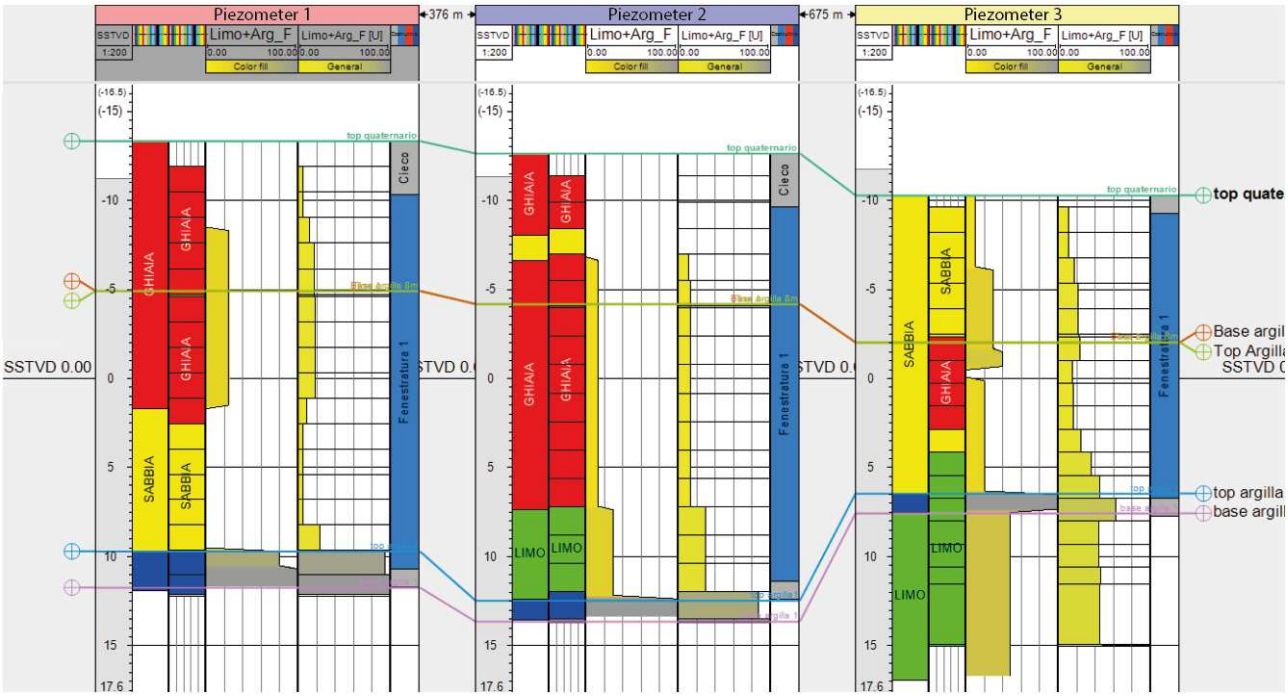

Figure 8. Well log upscaling. From the left to the right: facies well log, facies well log upscaling (most of), sum of clay and silt, sum of clay and silt upscaling (arithmetic),

Facies modelling

Using borehole logs data, the predominant facies were identified within every single layer and for each single borehole; afterwards facies and corresponding hydraulic conductivity values were assigned and distributed throughout the rest of the model selecting the most appropriate method for the modelling phase. The "Sequential Indicator Simulation" method was selected for the modelling process, being a pixel-based (or cell-based) distribution methodology constrained by directional variograms. This method will calculate the best stochastic realization of property based on the upscaled well observation, variograms and other input parameters. The size of the variable range of the variogram and the main direction will directly affect the results of the stochastic simulation. Based on the sedimentary background and source direction of the study area, a main range of 400x400 m and a vertical range of 1 m were selected (figure 9). The variogram correlates all the data included into the range. Finally, facies were distributed (using the facies data as starting point) (figure 10).

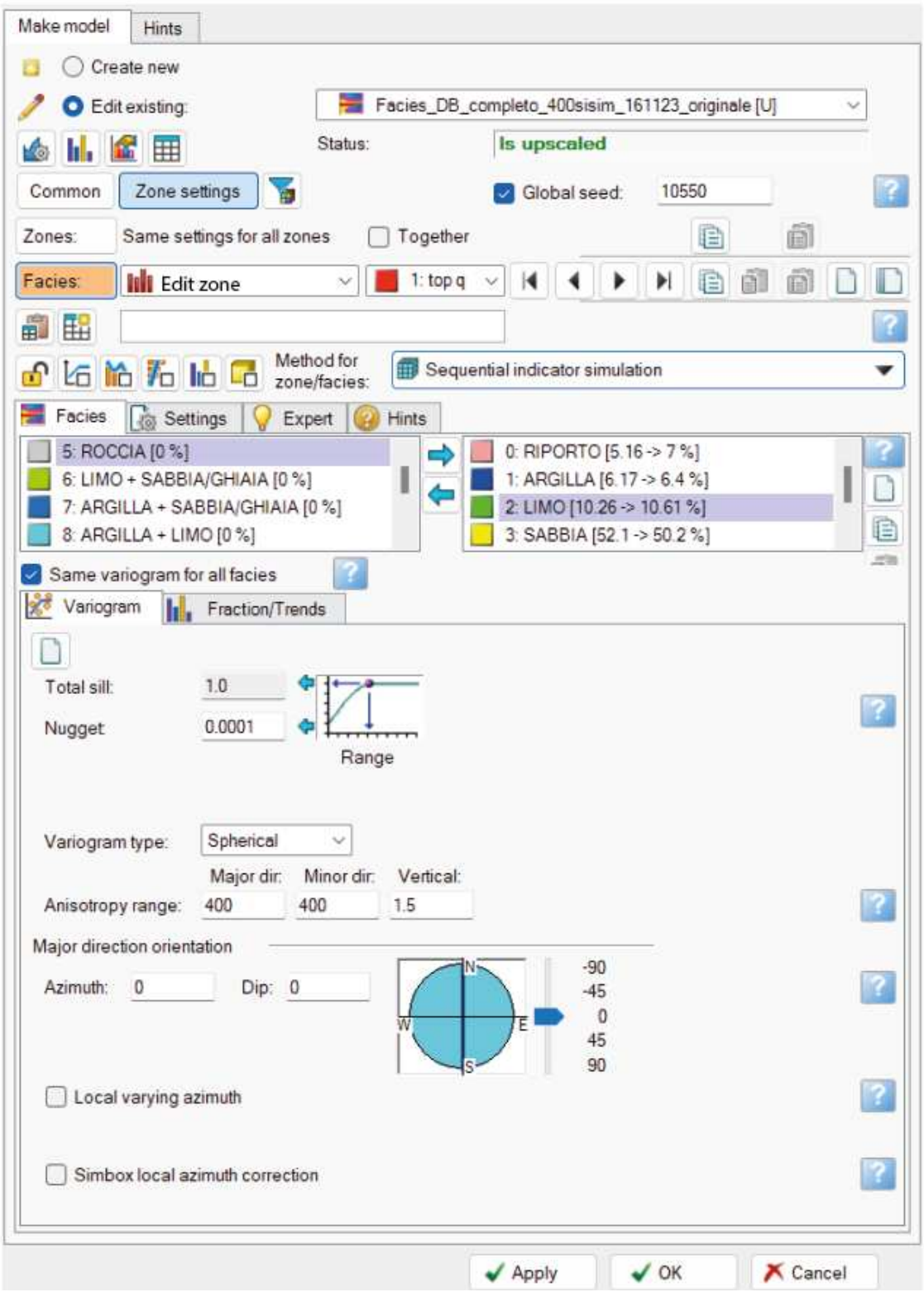

Figure 9. Examples of typical facies modelling windows.

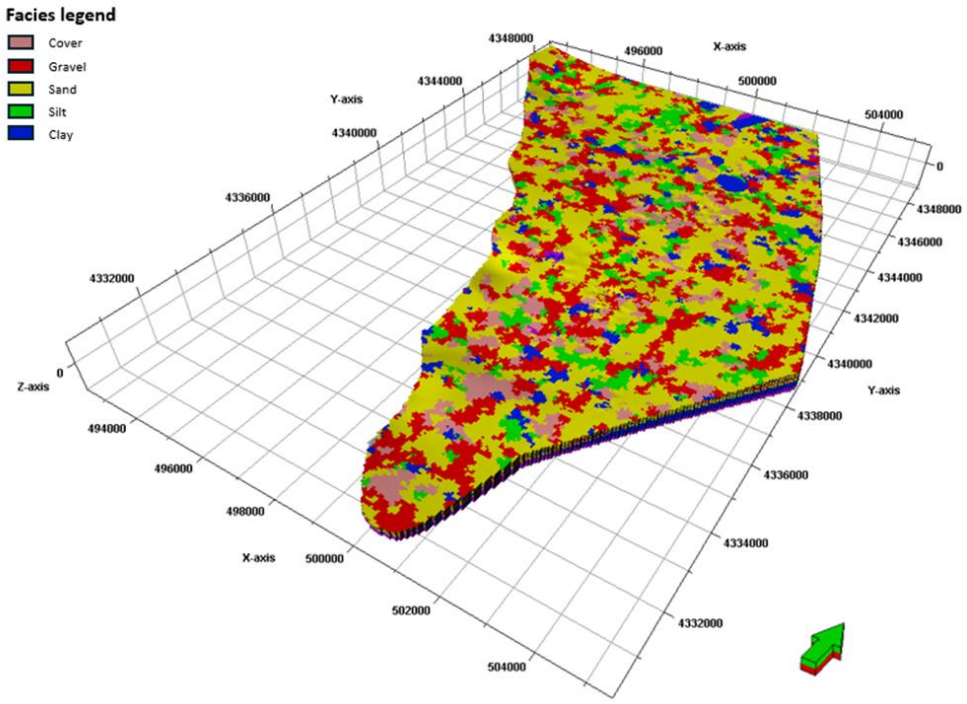

Figure 10. Result of the facies distribution using the "Sequential indicator simulation" algorithm and a variogram 400x400 m.

Petrophysical modeling process

Petrophysical property modeling is the process of assigning petrophysical property values (grain size percentual and hydraulic conductivity) to each cell of the 3D grid. Petrel offers several algorithms for modeling the distribution of petrophysical properties in a geological model. Petrophysics model was built using geostatistical methods. Sequential Gaussian Simulation algorithm was used as a statistical method which fits with the amount of the available data (figure 11).

For this part, the sum of clay and silt percentage was considered as a generic "fine material" since hydraulic conductivity showed a negative correlation with this parameter and it was distributed along the grid (figure 12).

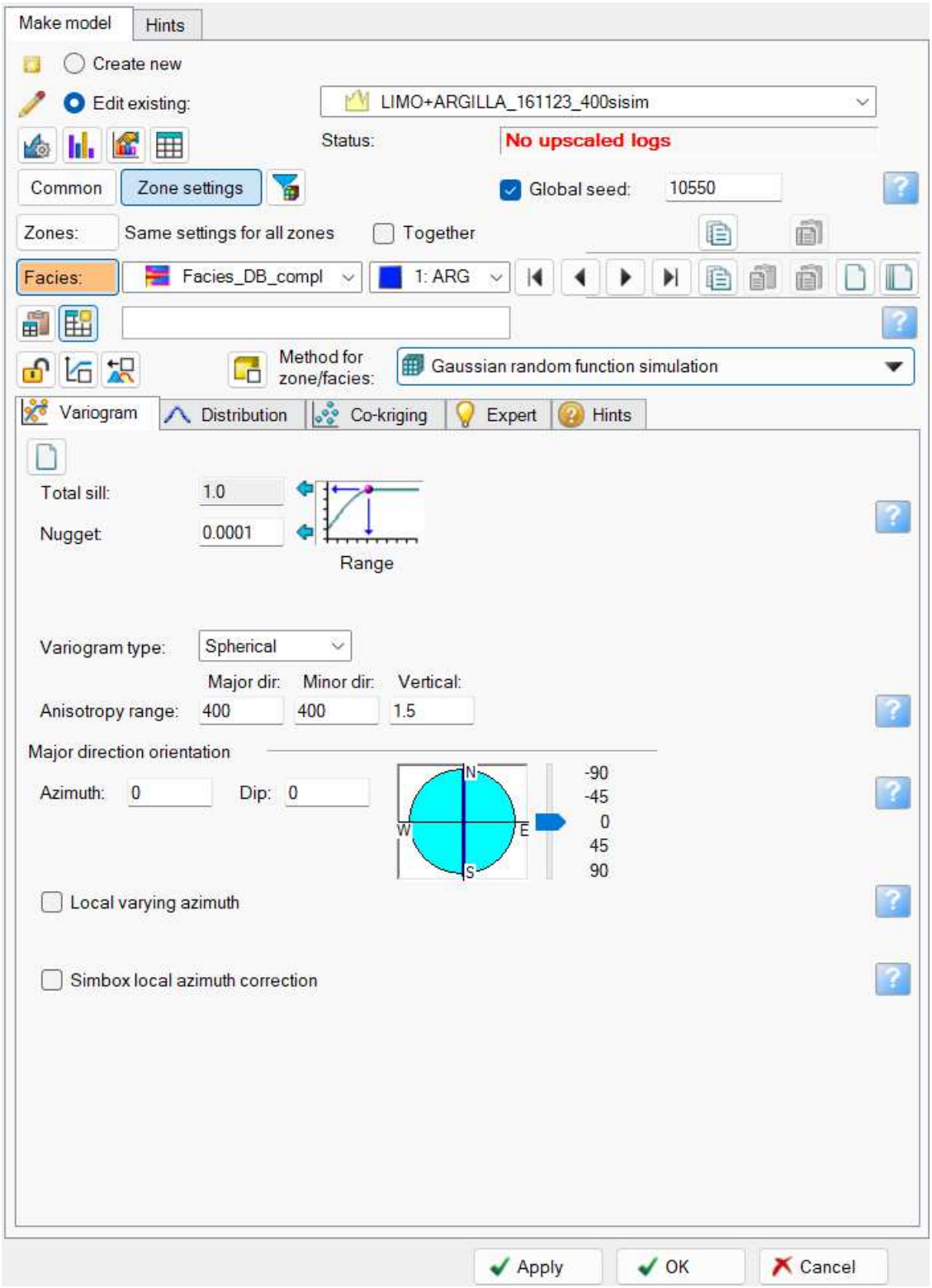

Figure 11. Petrophysical modelling windows of the grain size distribution.

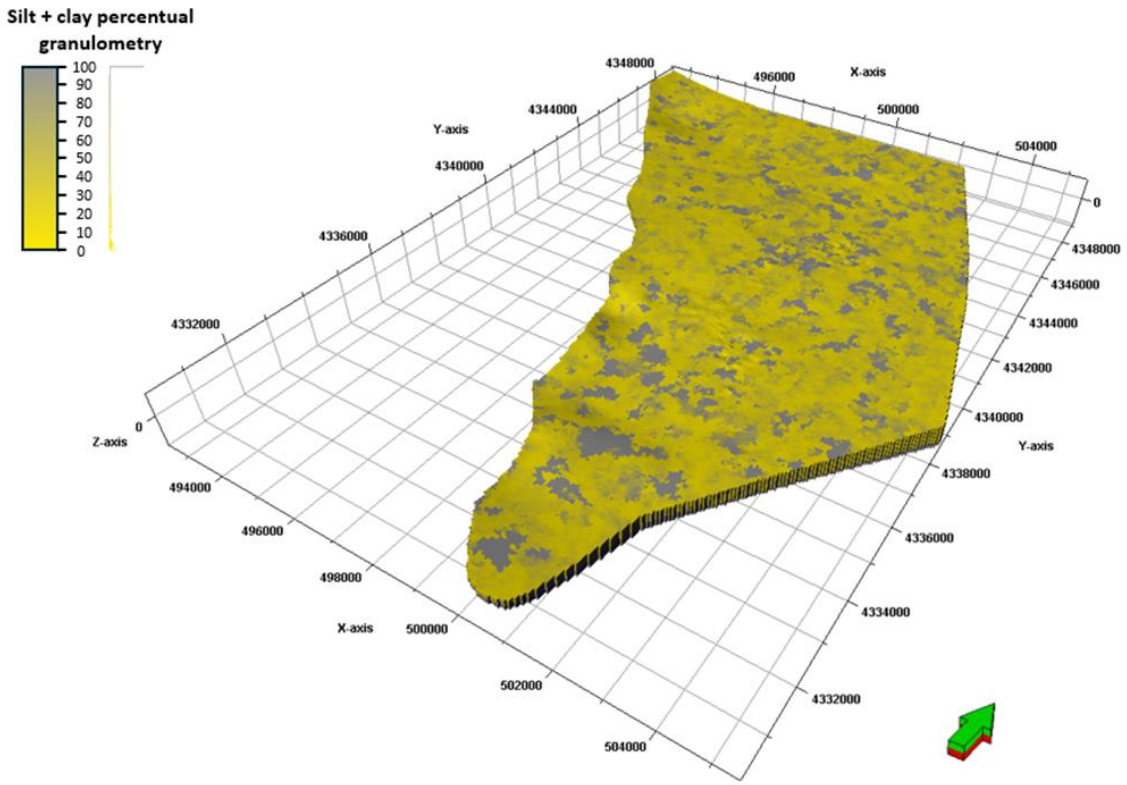

Figure 12. Result of the sum of Silt and Clay distribution using the "Sequential Gaussian Simulation" algorithm and a variogram 400x400 m.

To define the distribution of hydraulic conductivity (K), a database was created gathering all laboratory and pumping tests, with a total of 104 records. Lithology associated to lab test was synthesised as per log description, while for pumping tests an equivalent lithology was considered (weighted average on thickness). The sum of clay and silt in % showed, as mentioned, the best correlation with hydraulic conductivity (k). The 3D distribution of K was obtained with SGS and a bivariate algorithm, nested to the previous granulometric distribution (figure 13). This combination was able to reconstruct a distribution of a given cross-plot (figure 14).

The hydraulic conductivity distribution was achieved applying the bivariate algorithm with the granulometric percentages of silt and clay distribution (figure 15).

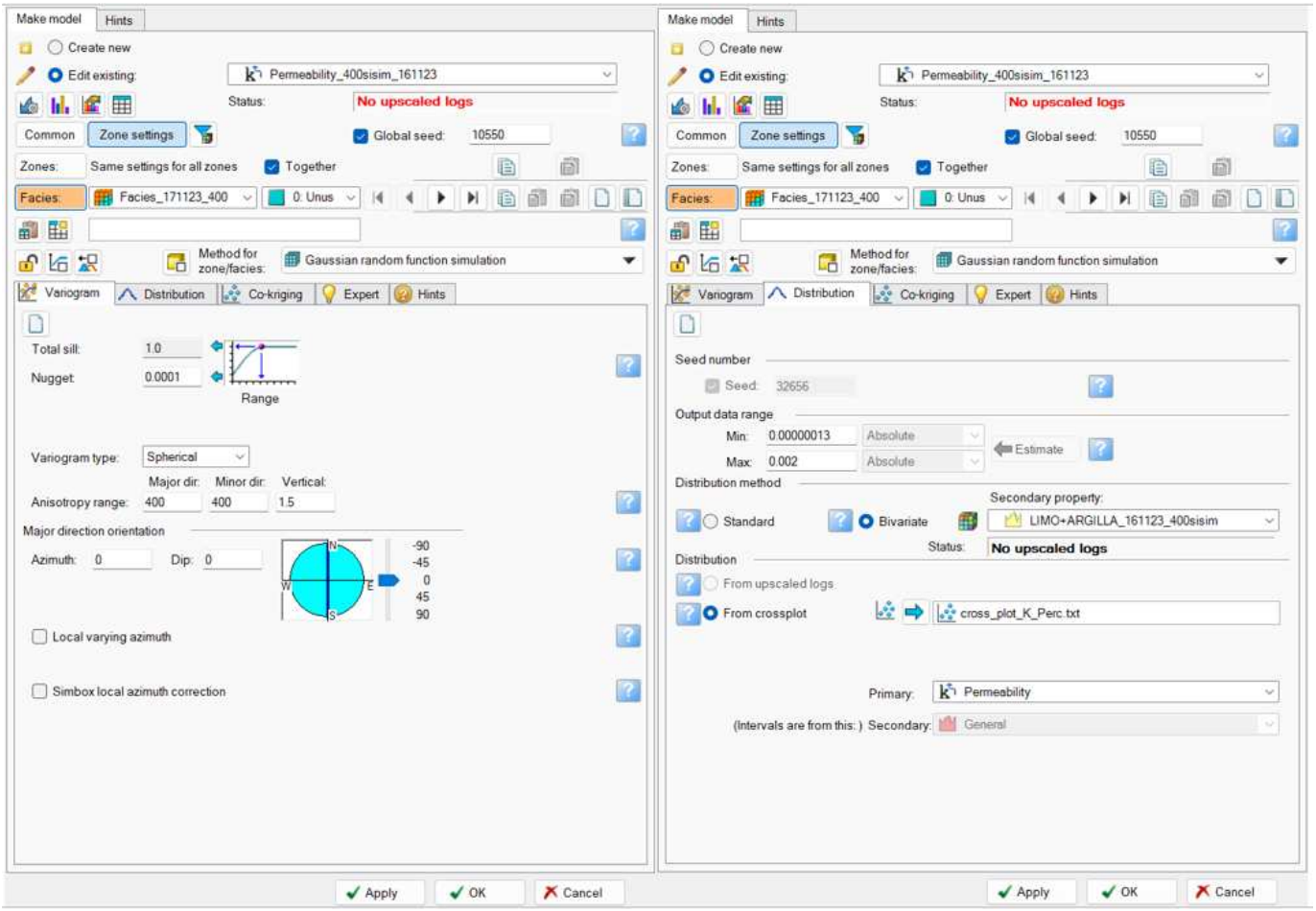

Figure 13. Petrophysical modelling windows of the hydraulic conductivity distribution process.

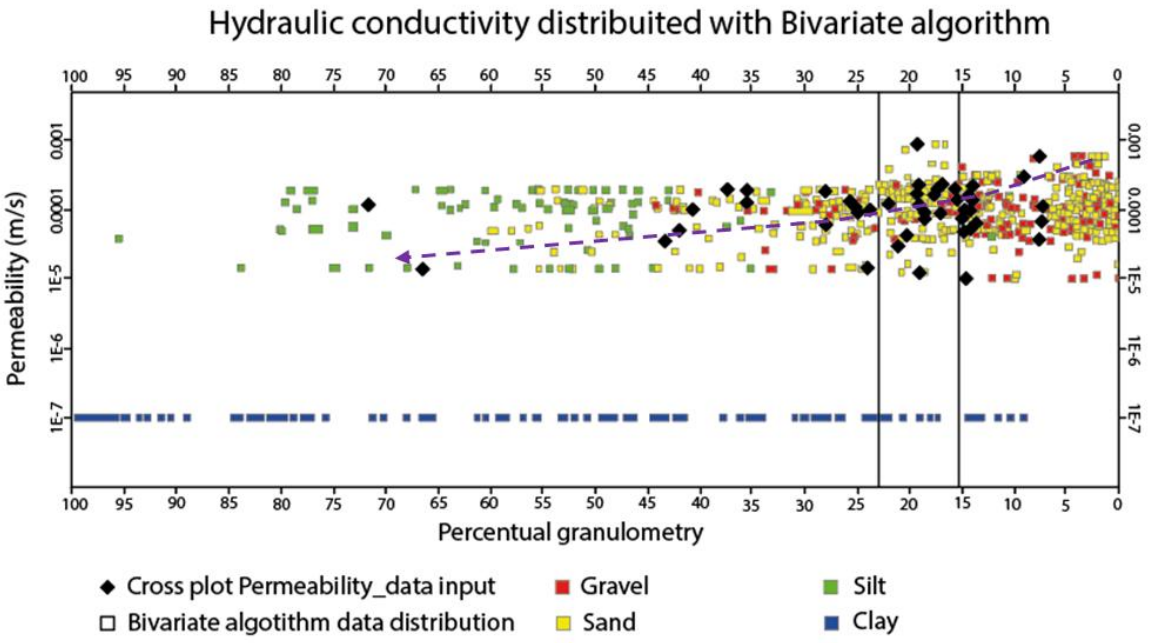

Figure 15. Graphic shows the hydraulic conductivity distributed with the Bivariate algorithm.

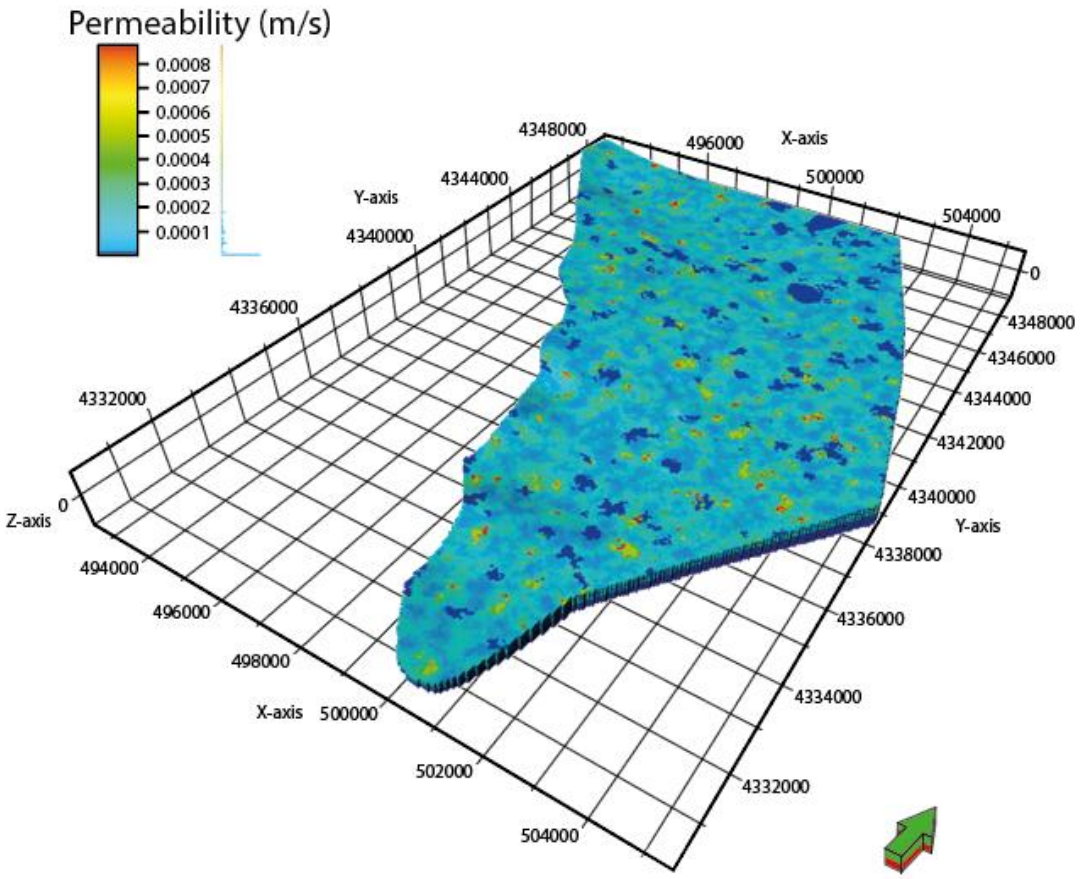

Figure 15. Result of the hydraulic conductivity distribution.

Appendix B

Numerical groundwater flow model development

The numerical groundwater flow model was developed using ModelMuse, an open-source software of the US Geological Survey (USGS), which acts as a graphical user interface for MODFLOW 6, efficiently simulating groundwater flow. Starting from the hydrogeological model developed with Petrel, we exploited their compatibility in grid type and indexing, producing a numerical groundwater flow model.

Model Design Workflow (Model Muse)

The main steps of building a numerical groundwater flow model using ModelMuse software are:

- Grid development;
- Data import;
- Grid refinement;
- Hydraulic conductivity adaptation;
- Boundary condition;
- Running and Calibration;
- Particle tracking.

1. Grid Development

The grid development begins by defining the number of rows, columns, and layers derived from the model created in Petrel. The indexing remains consistent between the two grids, as both originate from the same top-left vertex (figure 1).

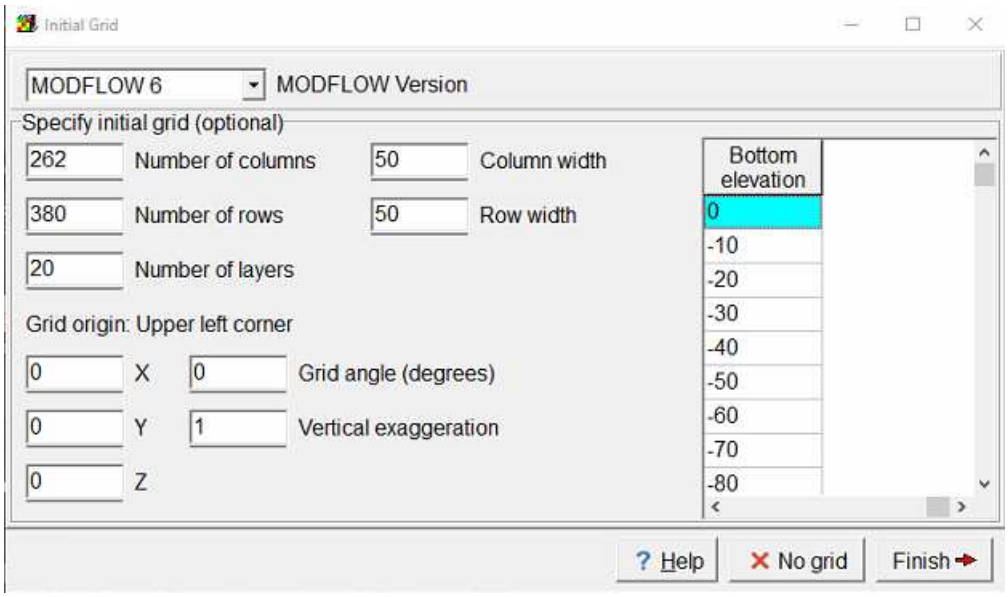

Figure 6. Initial grid data. Definition of the number of columns, rows, layers, cell widths and grid origin coordinates.

2. Data import

From the Petrel model, the boundary of the hydrogeological model and the surface elevation of each layer were exported.

The model boundary was extracted directly as a shapefile and imported into ModelMuse. It was designated with the "Set values of enclosed cells" property, applying it across all layers (figure 2). Next, a formula in the "Data Set" was used to define active and inactive cells (figure 3): all cells within the boundary were set as active, while those outsides were deactivated (figure 4).

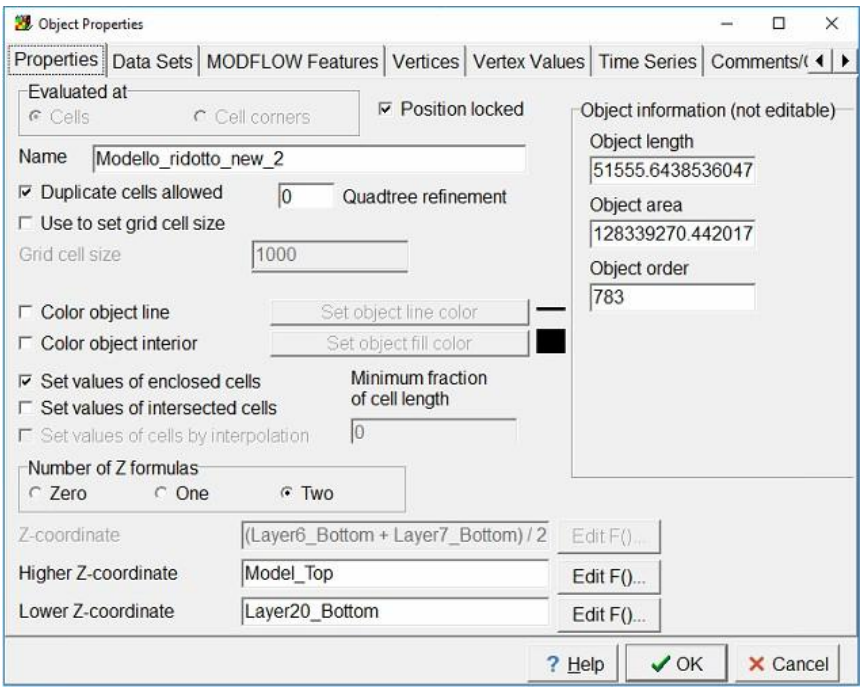

Figure 7. Applying Set values of enclosed cells property to all layers.

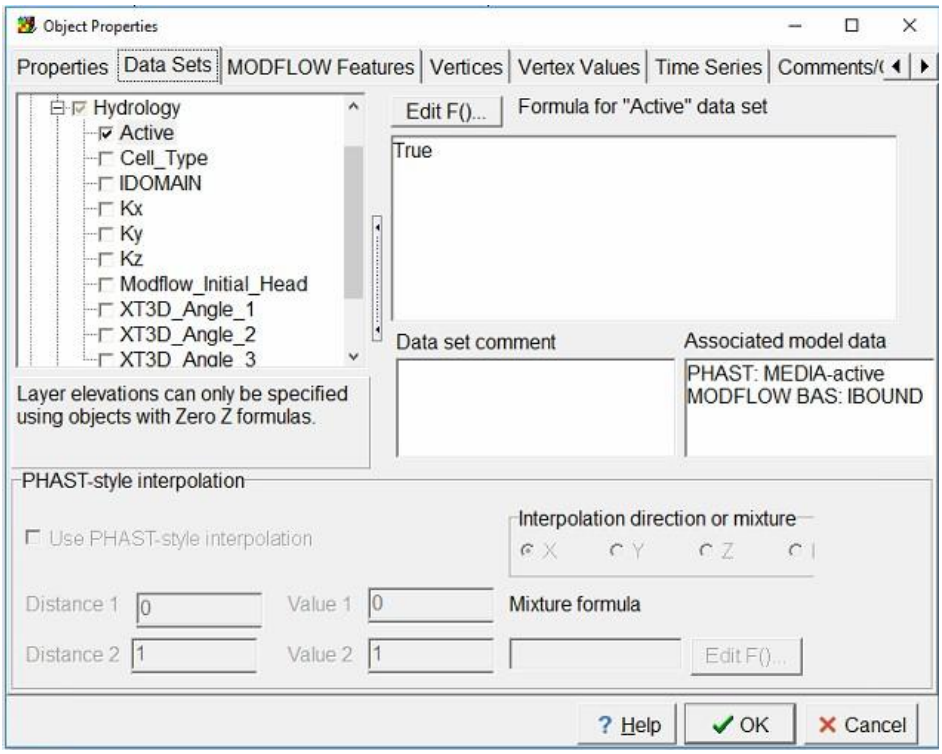

Figure 8. Data Set formula used to define active and inactive cells.

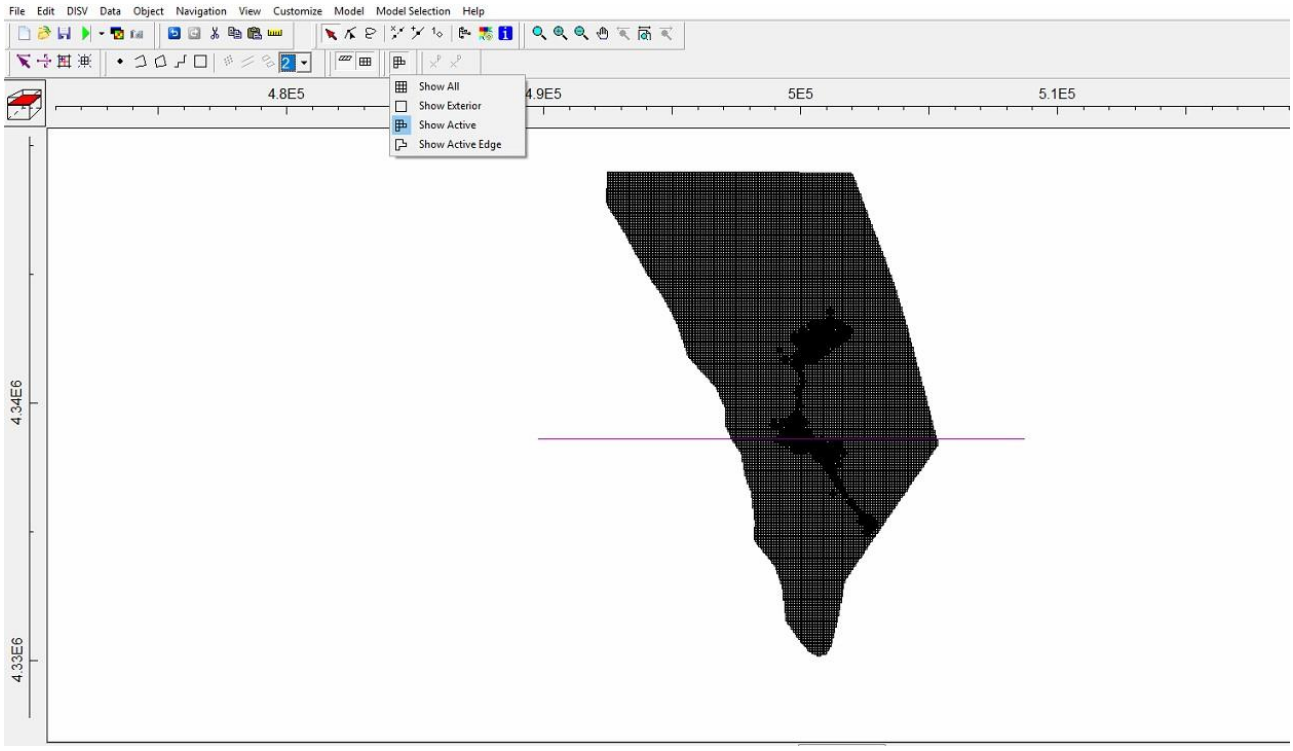

Figure 4. It shows the cells within the boundary which are set as active, while those outsides are deactivated.

For the export of each layer's elevation, the file was first imported into QGIS, where it was converted into a ModelMuse-compatible format (.grd). Each file was then associated with the corresponding reference layer in ModelMuse using interpolation (figure 5).

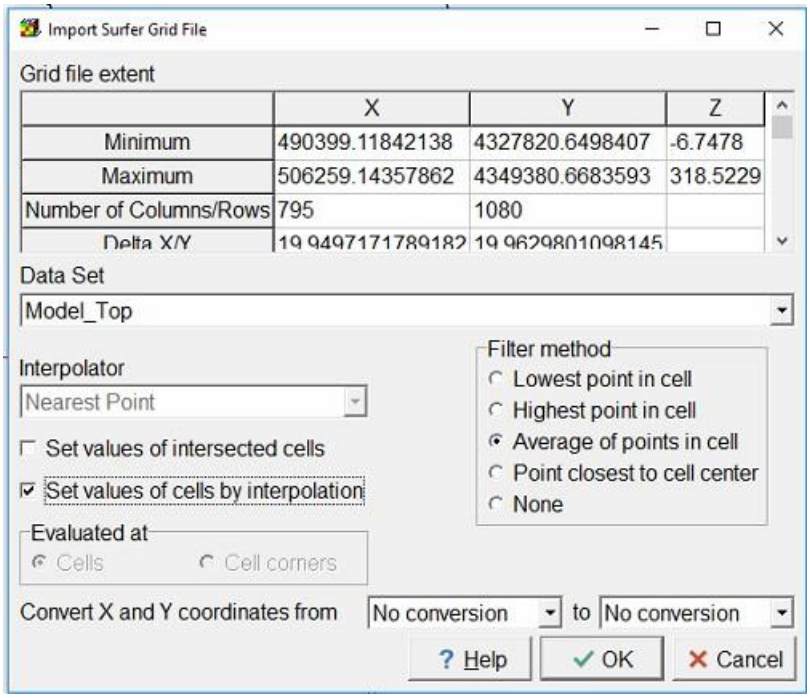

Figure 5. Import of the surface elevation for each layer.

3. Grid refinement

The wells and piezometer's locations were inserted as a shapefile to support the grid refinement phase. The grid was then converted from a "structured grid" into a "DISV," after which a quadtree refinement was generated based on the well and piezometer shapefile (figure 6, figure 7).

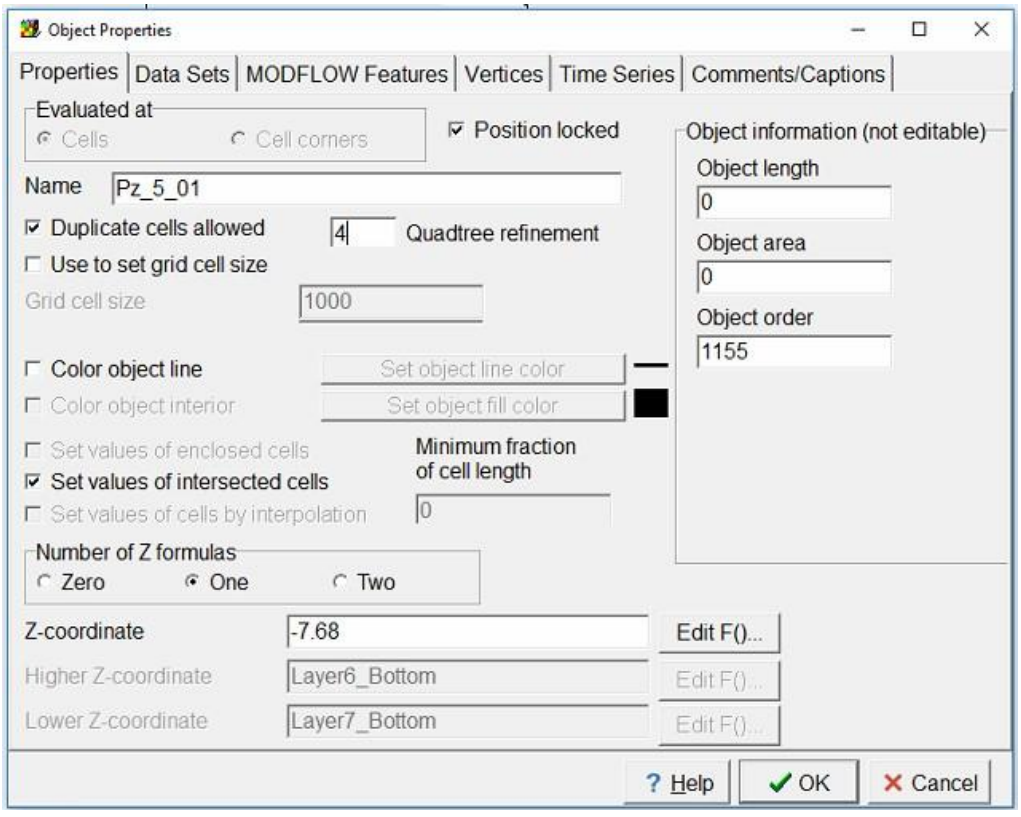

Figure 6. Quadtree refinement of well data.

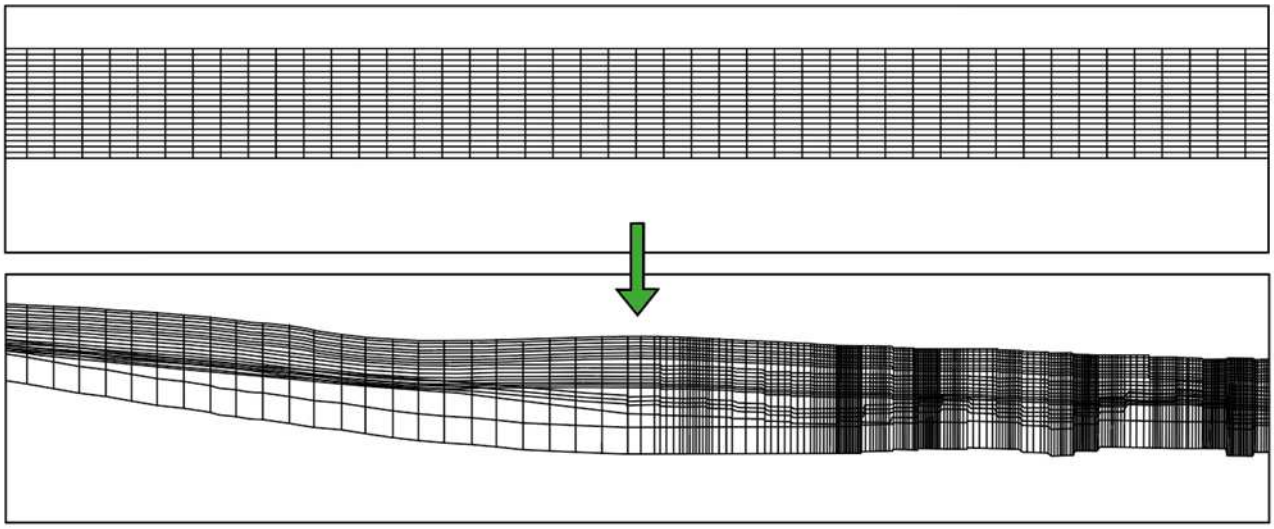

Figure 7. This figure shows the passage from a regular grid created on ModelMuse (section A) to the final numerical groundwater flow grid model, where it was importing the surface elevation and the quadtree refinement.

4. Hydraulic conductivity adaptation

Once the grid has been refined, it needs to be applied in Petrel to achieve the correct distribution of hydraulic conductivity. To distribute permeability accurately, the centroid of each cell in the ModelMuse grid was exported to Petrel. After uploading the centroid data from ModelMuse, an average map was generated, resulting in a surface grid representing the average permeability at each x and y position. We then defined the permeability values for each cell centroid and exported them in Petrel format. Note that:

- Each file contains the centroid coordinates (X, Y), layers, and corresponding permeability values.
- This process was repeated for each model layer.

Subsequently, we imported all these files into ModelMuse and applied an intersection to assign cell values (figure 8).To display the hydraulic conductivity import, go to "Data Visualization" and select the file containing the hydraulic conductivity distribution under "Data Sets" (figure 9).

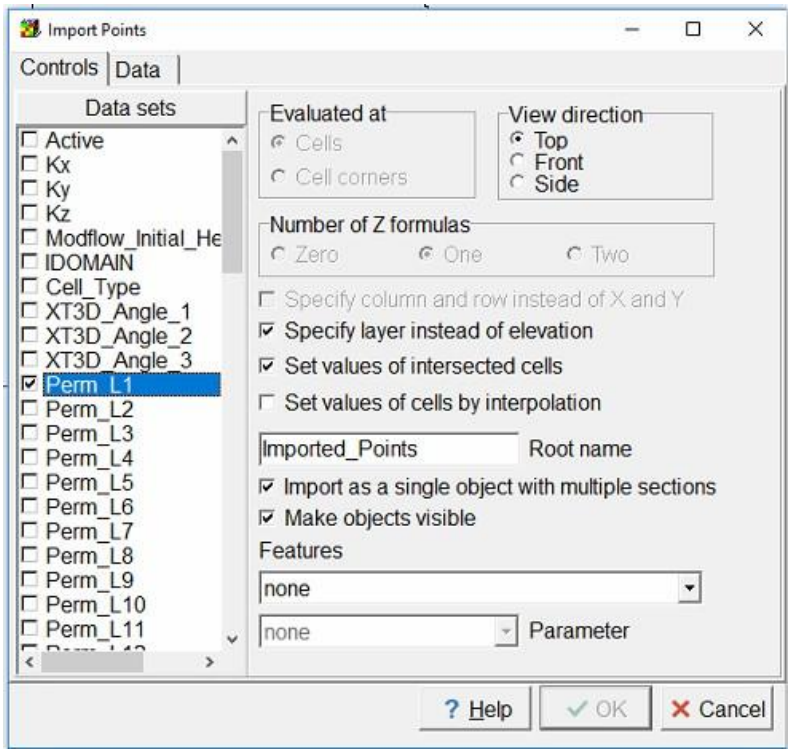

Figure 8. Hydraulic conductivity was imported for each layer by correctly setting each layer in the Data Sets (e.g., Perm_L1). The layer was specified instead of elevation, and values were assigned through intersection. A .txt file containing X, Y coordinates, layer numbers, and corresponding permeability values was uploaded into the data.

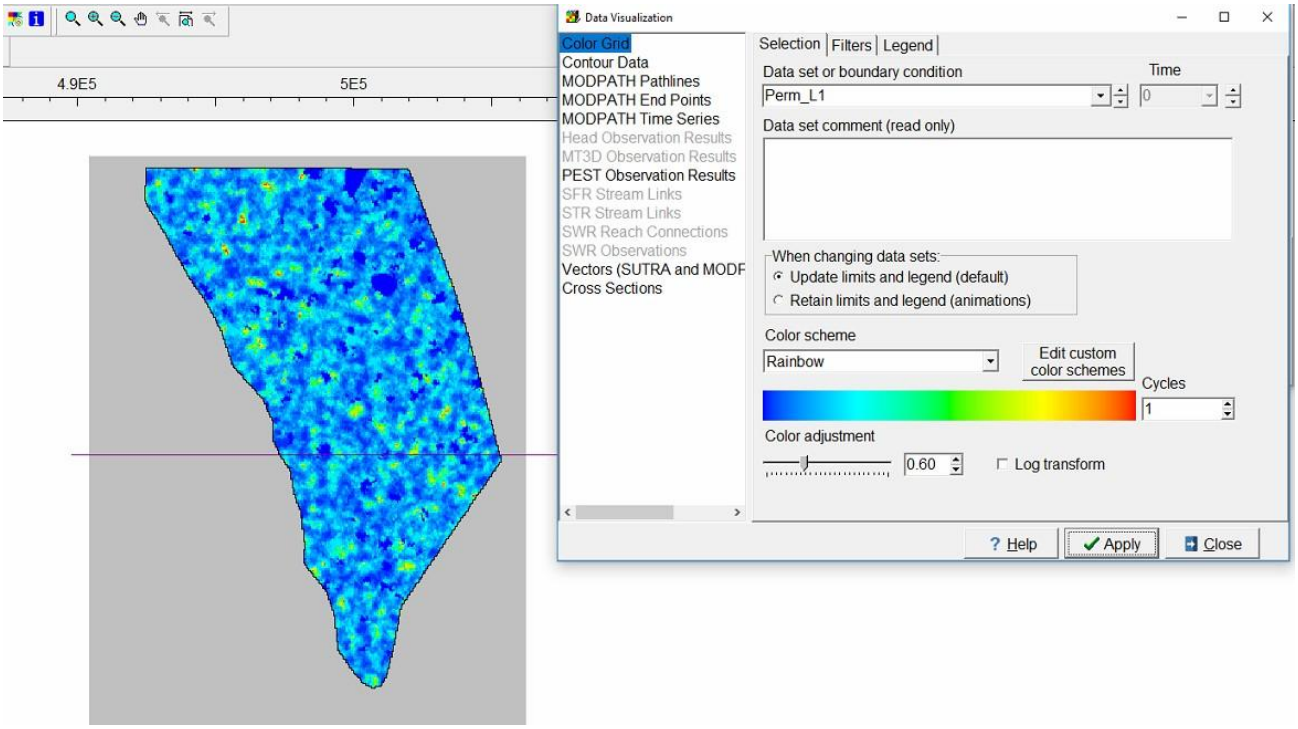

Figure 9. Display of hydraulic conductivity distribution using "Data Visualization."

5. Boundary conditions

Once the numerical flow model was developed, it was set up to simulate a medium-high groundwater heads scenario. "MODFLOW Time" is the panel where you can set the starting time, ending time, and specify whether the model is in a steady state (figure 10).

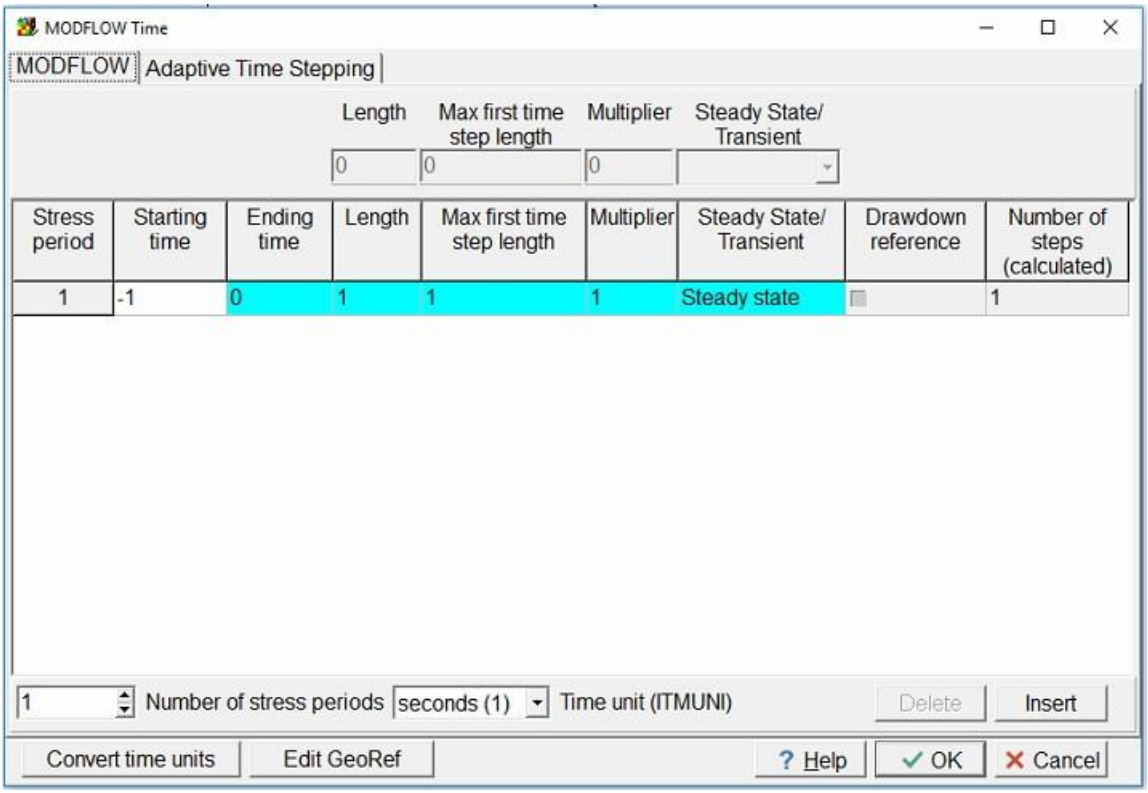

Figure 10. Panel necessary for setting the model type and time.

By selecting the "MODFLOW Packages and Programs" section from the "Model" panel, it was possible to choose which “Flow packages” and “boundary conditions” to activate. The following packages were selected: Ghost-Node Correction package (GNC), Constant Head (CHD), Well packages (WEL), Recharge packages (RCH) and the Observation utility (OBS) (figure11).

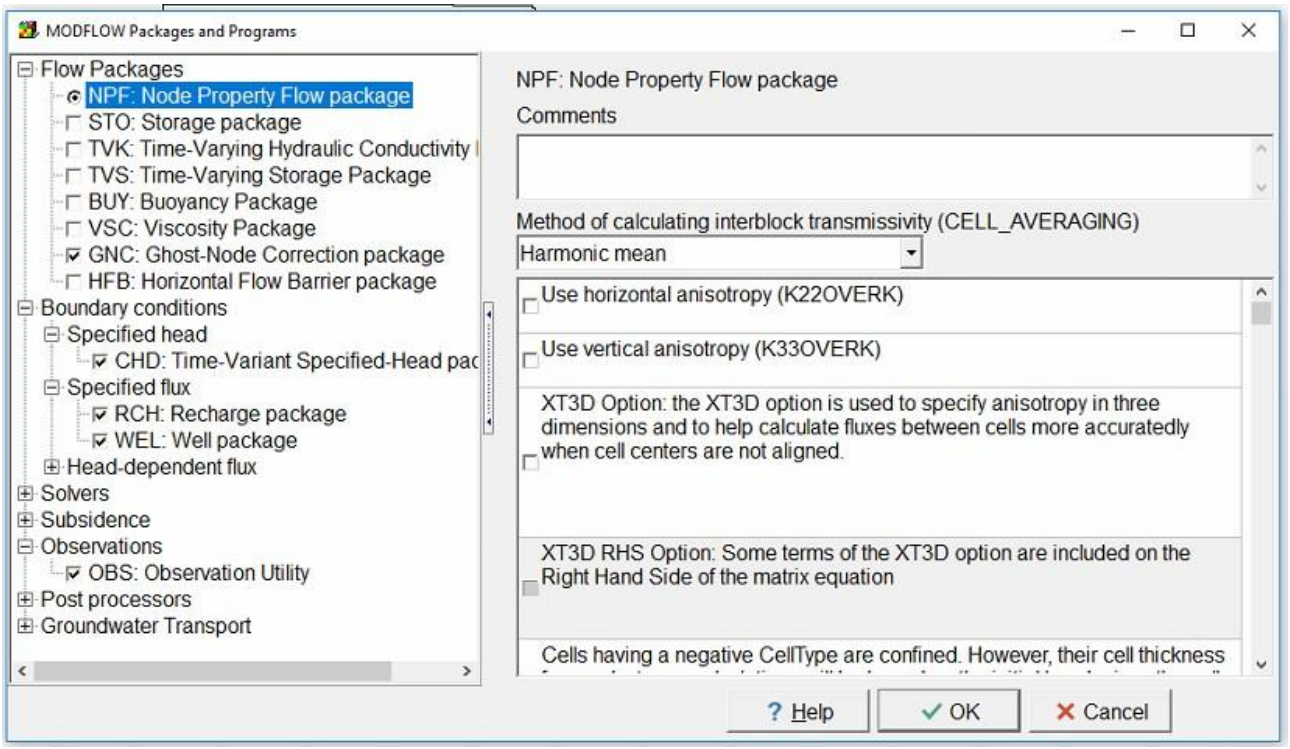

Figure 11. MODFLOW Packages and Programs choice.

Boundary conditions were introduced by drawing lines corresponding to the selected areas using the "Create Polyline Object" tool. Once plotted, these lines were interpolated across all layers (figure 12). In the "MODFLOW Features" panel, the "CHD Package" was activated, and the starting time, ending time, and values were defined (figure 13).

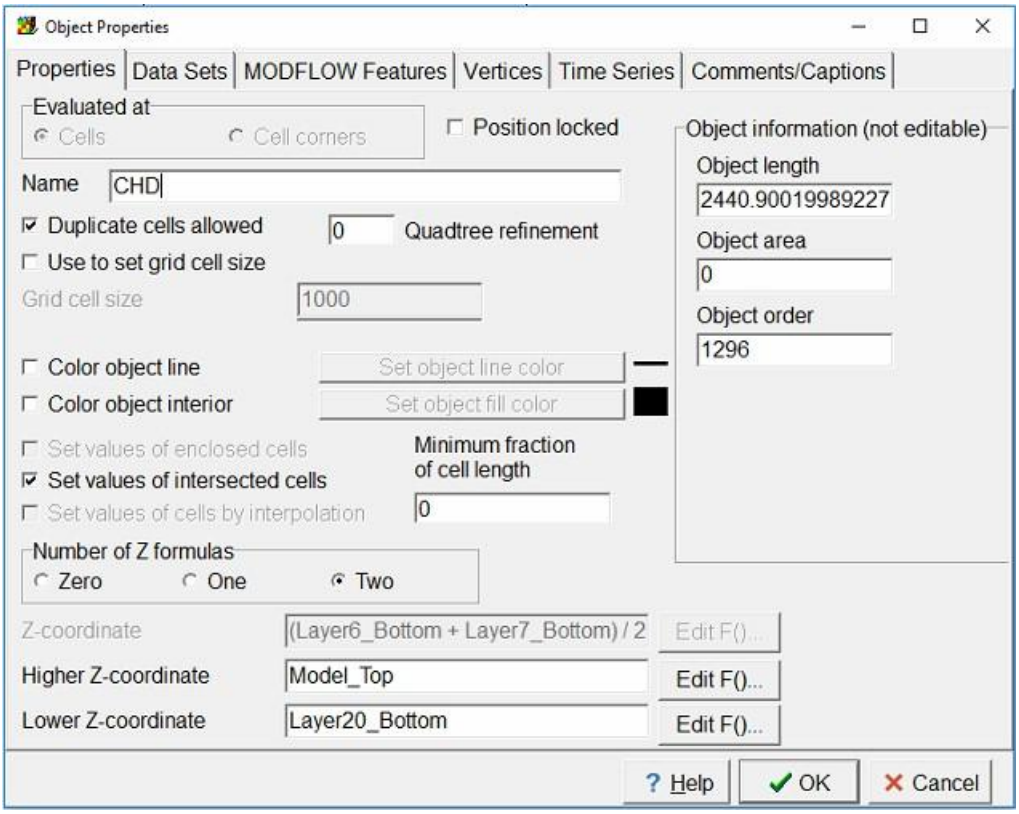

Figure 12. Panel displaying the application of the intersection process across all layers.

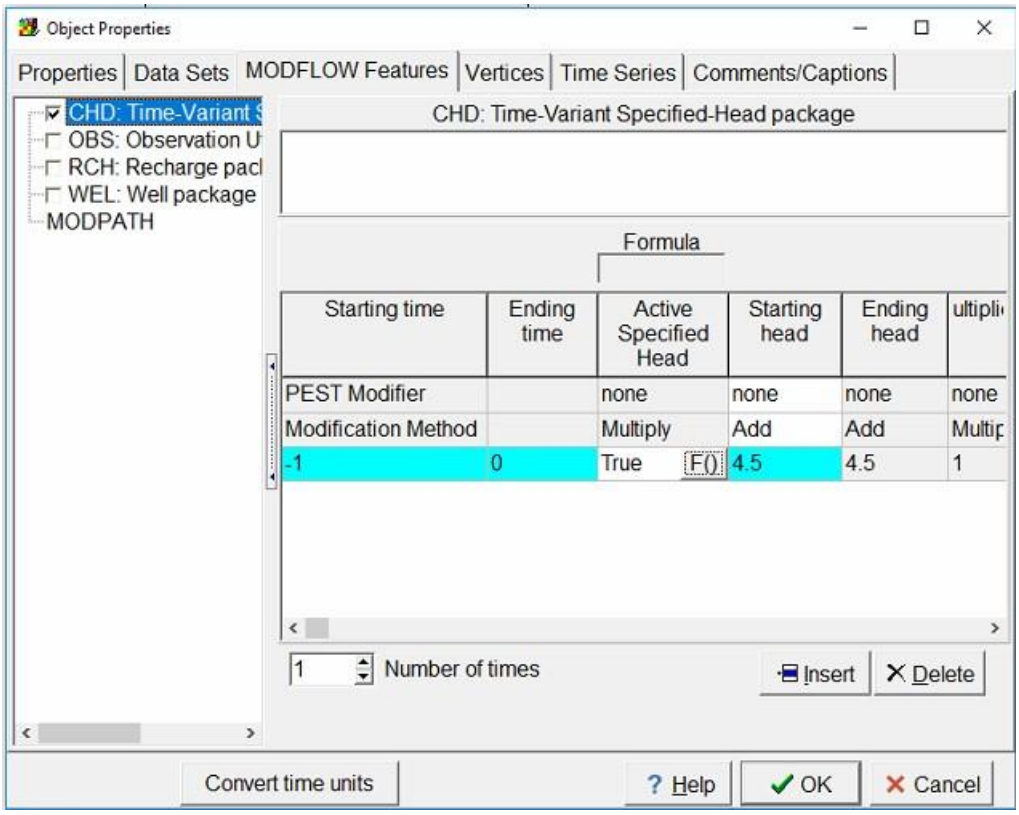

Figure 13. Panel displaying the activation of the CHD package.

Recharge (RCH) value was introduced using a polygon. Once plotted, the polygon has been set as enclosed cells and applying on the surface of the model (figure 14). In the "MODFLOW

Features" panel, the "RCH Package" was activated, and the starting time, ending time, and values were defined (figure 15).

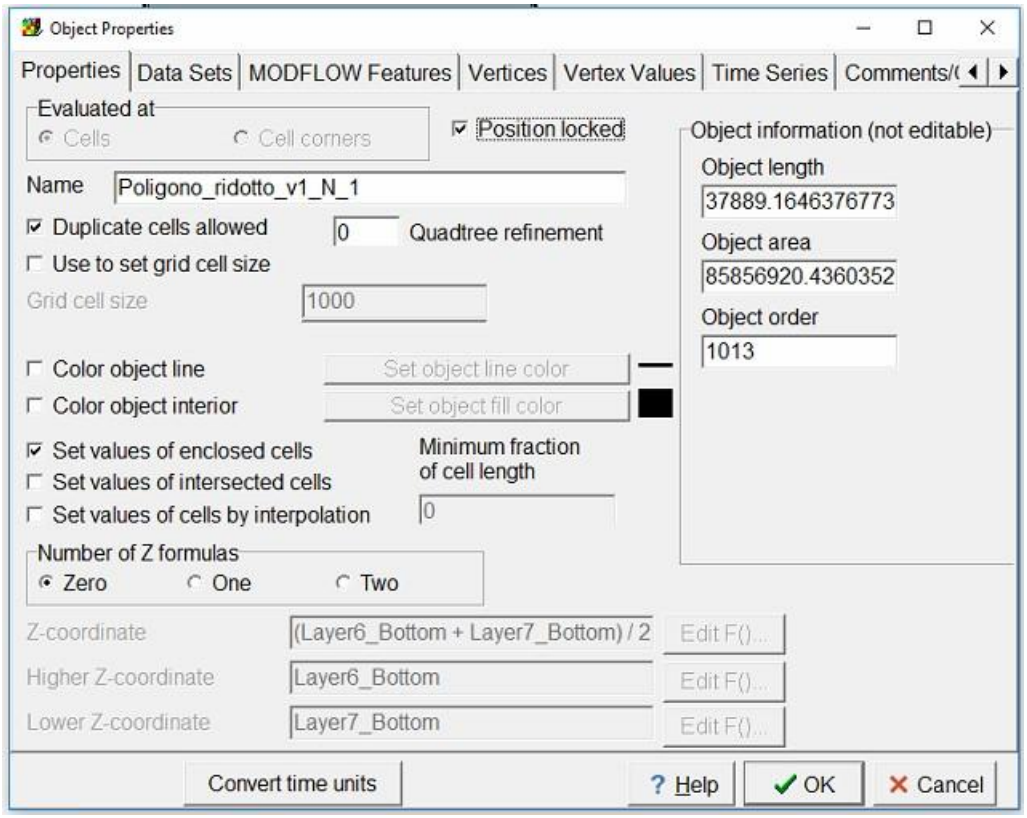

Figure 14. Panel displaying the application of the enclosed cells to the surface of the model.

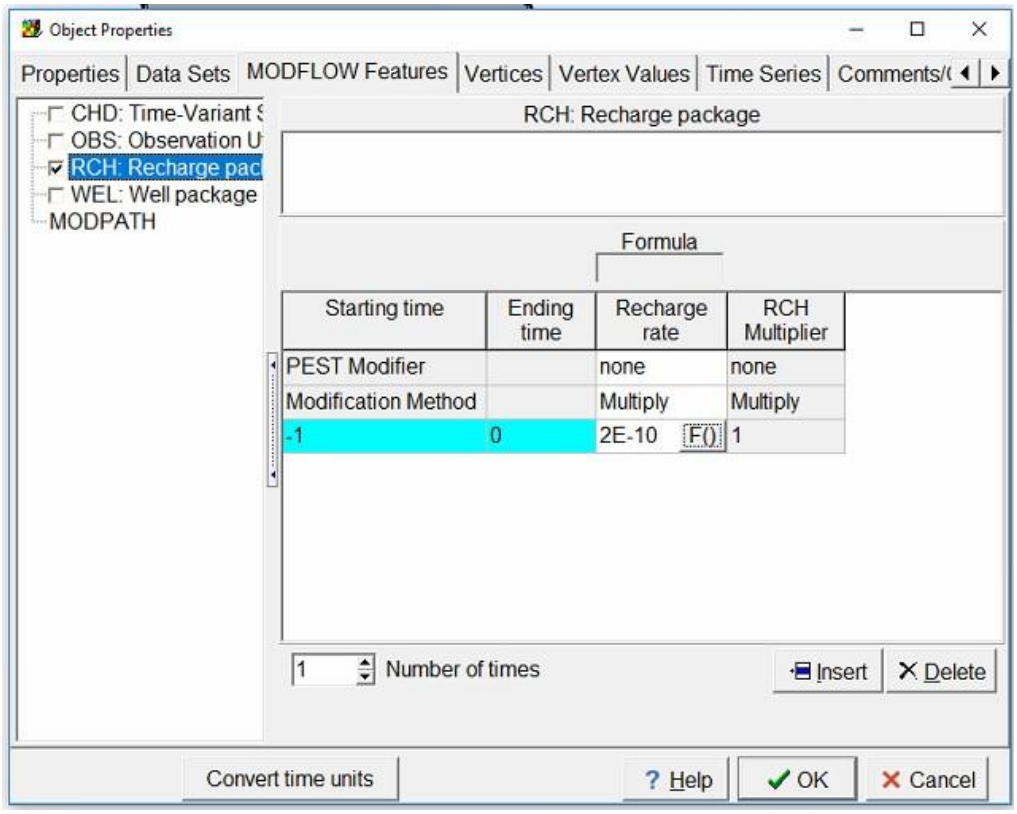

Figure 15. Panel displaying the activation of the RHD package.

The WEL data package was implemented by assigning a specific pumping rate to each active well using intersection. (approximately 150) (figure16). For this purpose, an Excel file was created containing the well coordinates, well bottom depth (m a.s.l.), starting time, ending time and the pumping rate (m^3/s) (Figure17).

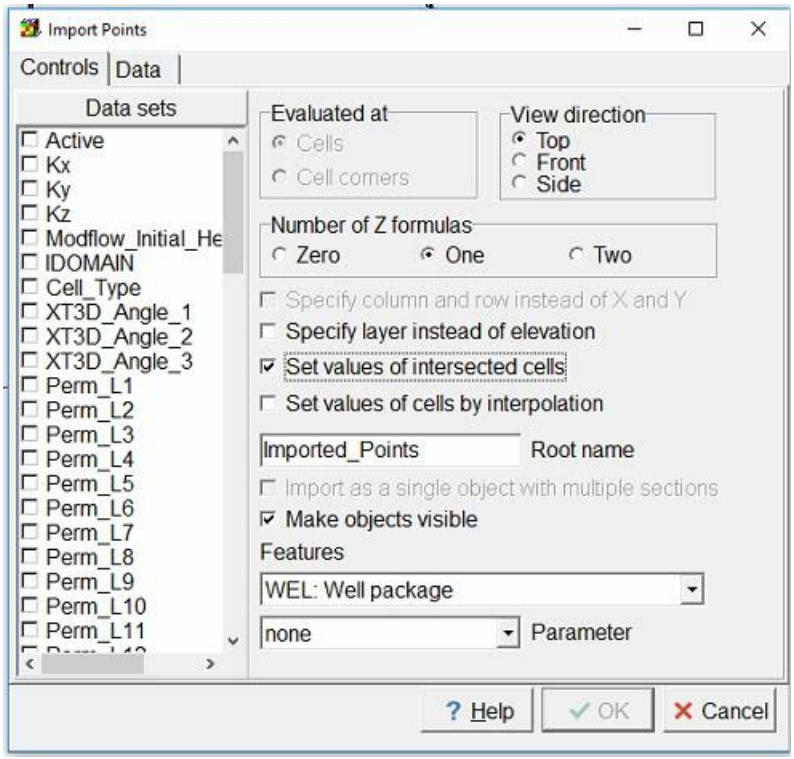

Figure 16. Panel displaying the application of the WEL package.

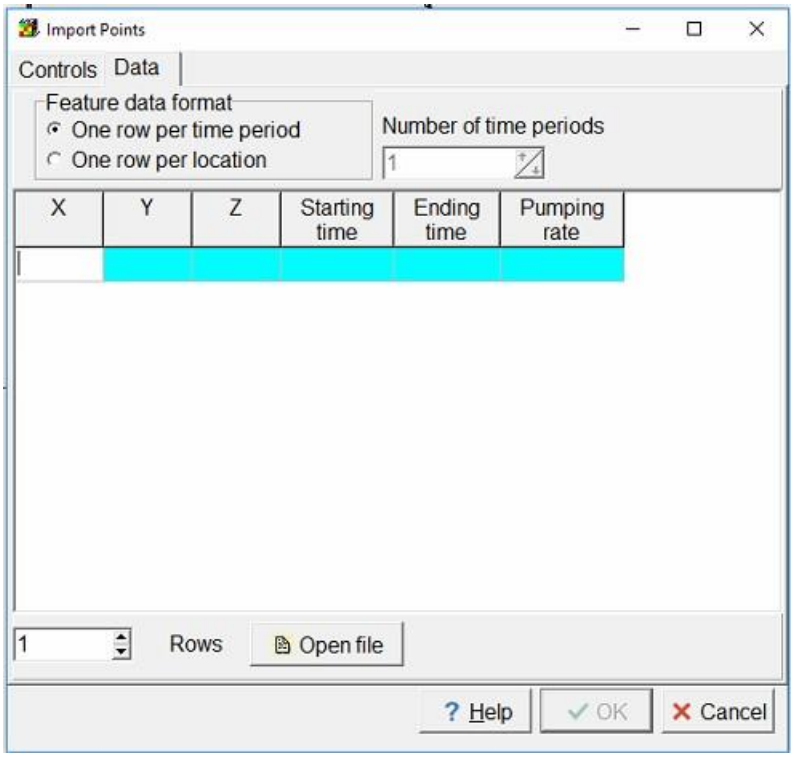

Figure 17. Panel displaying the required data for the well import file.

Groundwater heads measured at approximately 300 monitoring wells were imported using the Observation Package (OBS). A shapefile was created containing the coordinates of each piezometer, the mid-screen elevation (m a.s.l.), and the groundwater head value (figure18, figure 19 and figure 20).

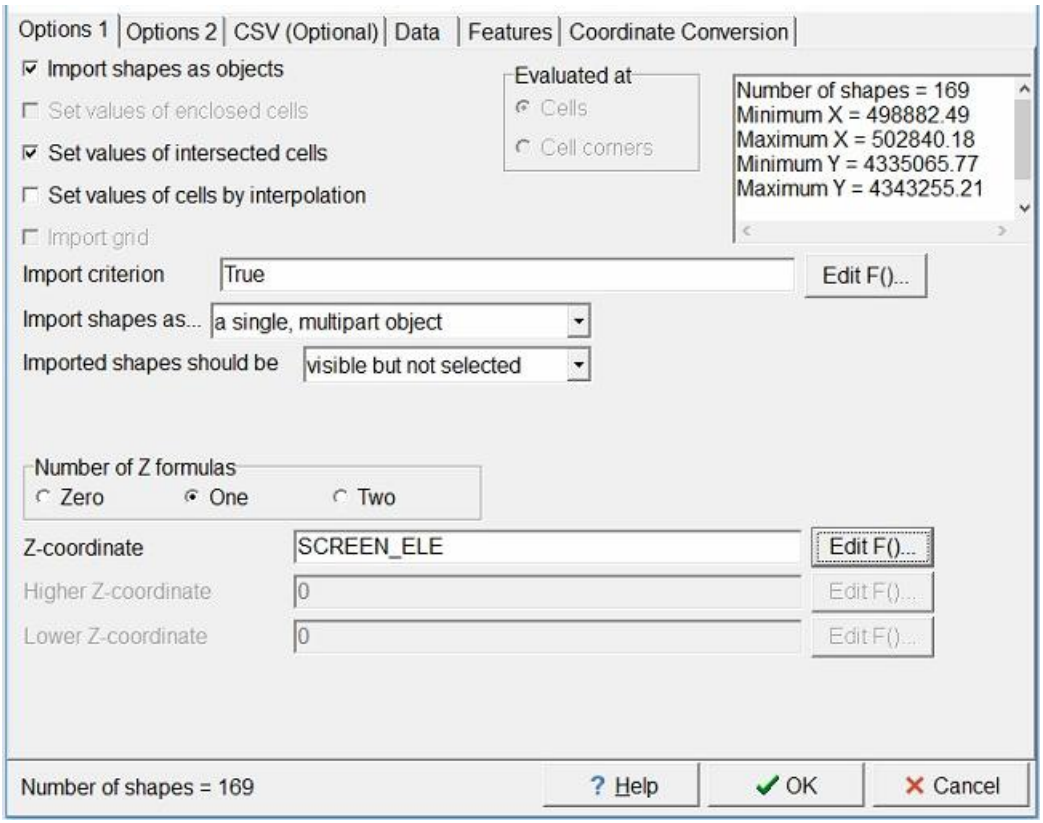

Figure 18. Window displaying the import process for monitoring wells, where values are set by intersection, with the mid-screen value assigned as the Z coordinate.

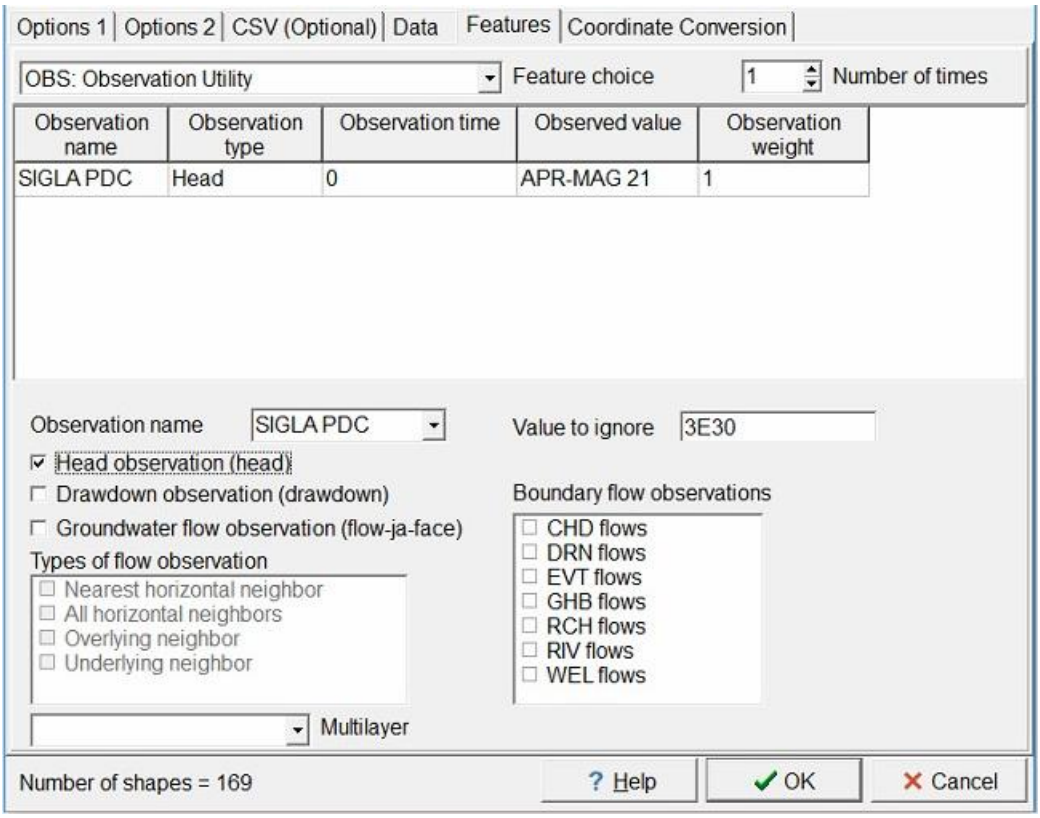

Figure 19. Panel displaying the activation of the OBS package.

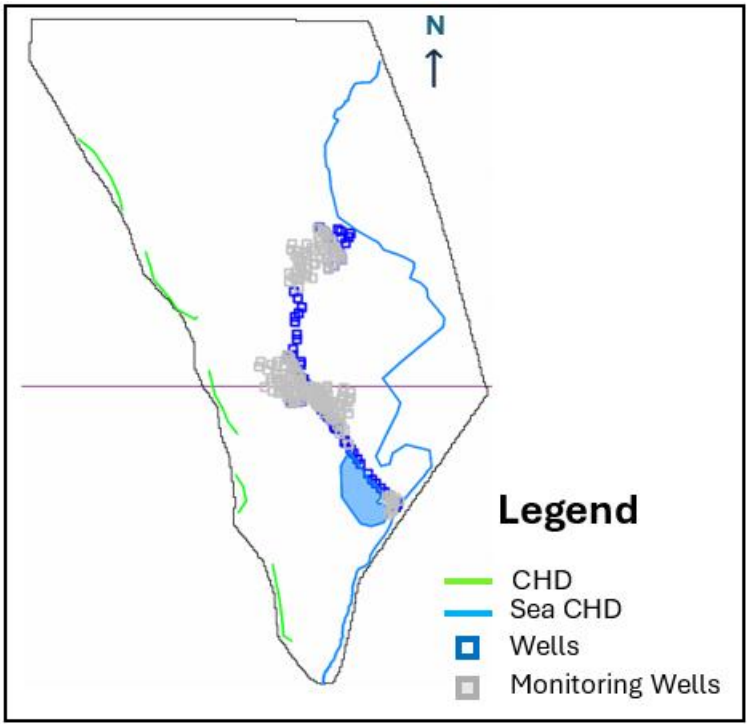

Figure 20. It shows the model after all boundary conditions have been defined.

6. Model running

After setting up the numerical flow model with boundary conditions, we proceeded to the run phase. By clicking on "Run MODFLOW 6," a window opens allowing the creation of a new folder

where all model run files will be saved. Among these files, those used include the hydrogeological balance output (mfsim.lst) and the excel file containing groundwater head values for the monitoring wells (....ob_gw_out_head).

he calibration phase was performed by entering the simulated groundwater head values into an Excel sheet, where they were plotted on a cross plot alongside the measured groundwater heads. Figure 21 displays this cross plot, with measured groundwater heads plotted on the X-axis and simulated groundwater heads on the Y-axis. The purpose of this graph is to illustrate how the plotted values of individual monitoring wells deviate from the bisector of the second and fourth quadrants.

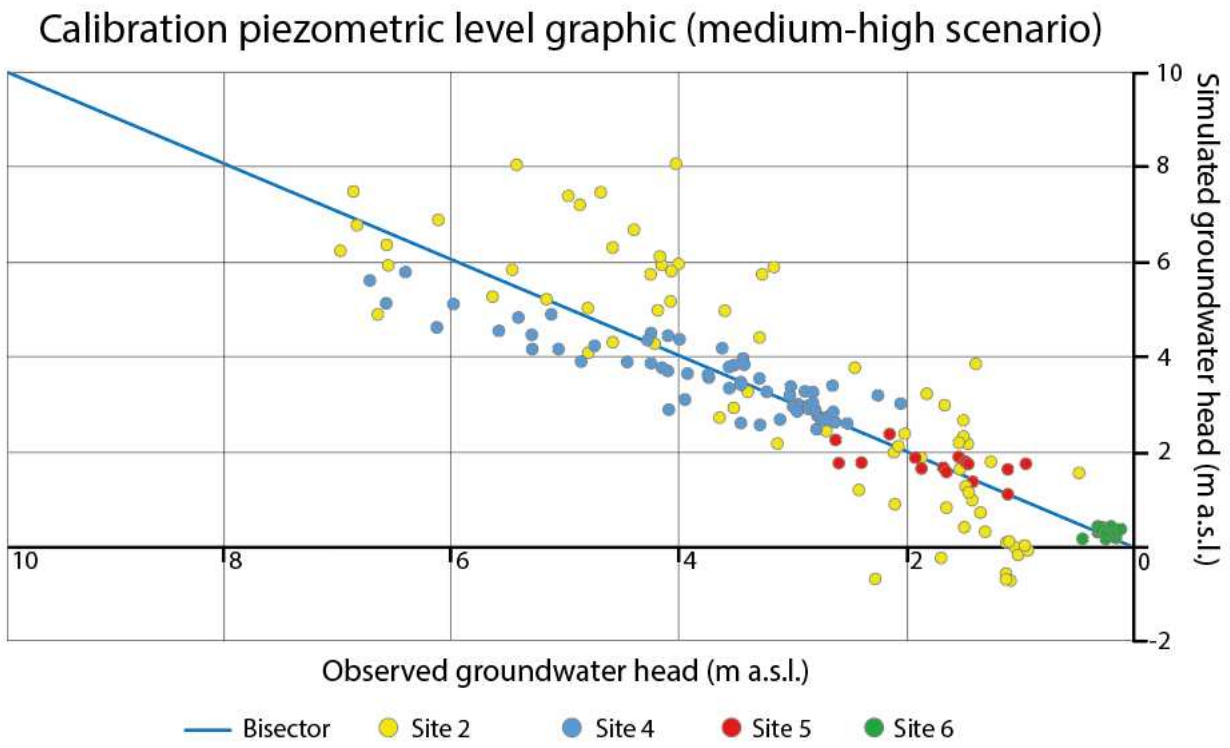

Figure 21. Graph represented a medium-high scenario, where the difference between the measured groundwater heads (X-axis) and the simulated groundwater head (Y-axis) is plotted. The plot represents the groundwater flow direction having the highest groundwater head placed west (left side of the plot).

7. Particle tracking

To perform particle tracking, it was necessary to activate "MODPATH" in the "MODFLOW Packages and Programs" section. The opening window allows you to choose whether to track particles in a forward or backward direction and to specify the desired output type (figure 22).

In this project, particle tracking was conducted in the forward direction. Using the "Create Polylines" tool, points were established from which to start the particles. In the panel that opens, you can select the intersection and layer from which to start the particles (figure 23). In the "MODFLOW

Features" section, MODPATH is activated, allowing you to define the number of particles to be released from each cell intersected by the line and their distribution within the cell (figure24).

To run the particle tracking, select "Export MODPATH Input File" and then choose the folder created during the running phase. Once the particle tracking is complete, you can open the "Data Visualization" window and select the generated file in the "MODPATH" section to view the results.

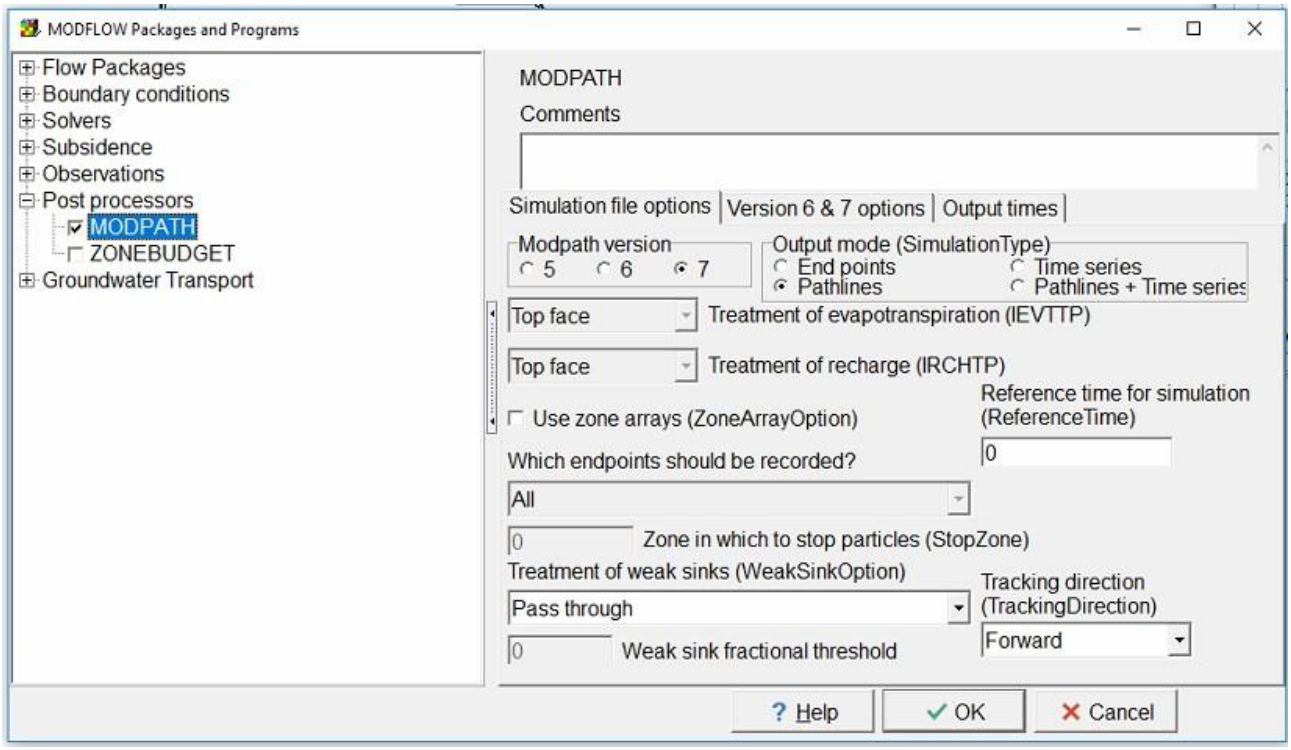

Figure 22. “MODFLOW Packages and Programs” panel where the MODPATH package for particle tracking is activated.

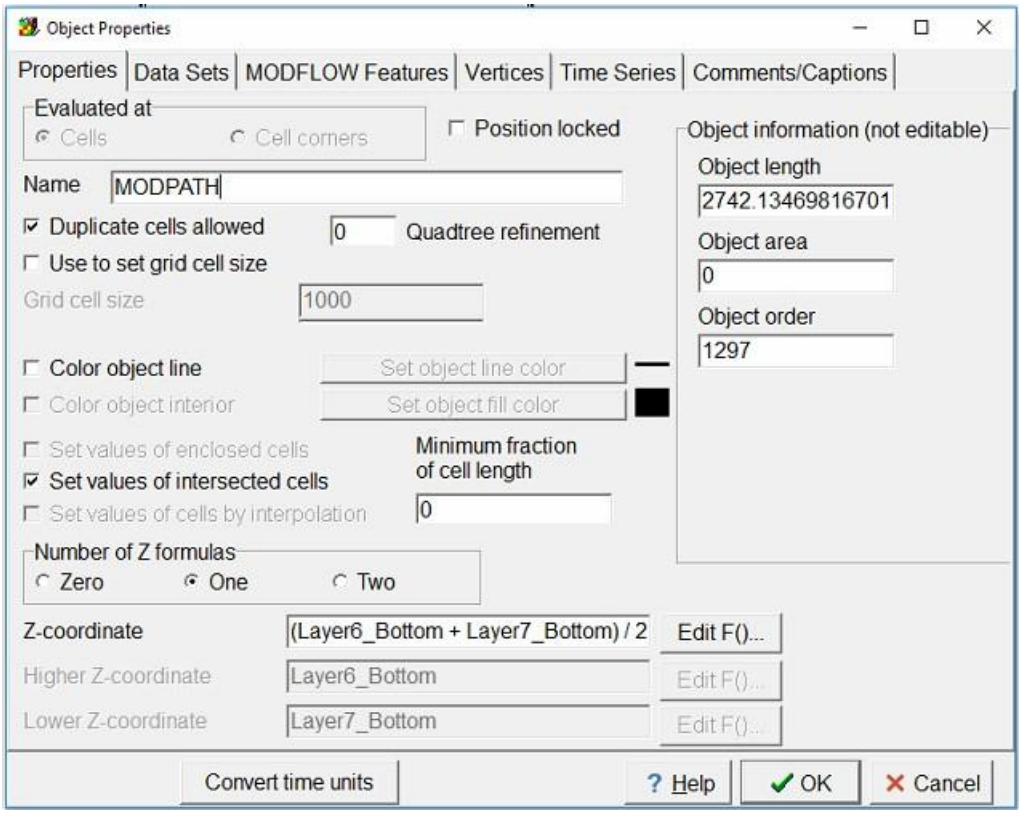

Figure 23. Window displaying options to select the intersection and layer where the particle tracking starts.

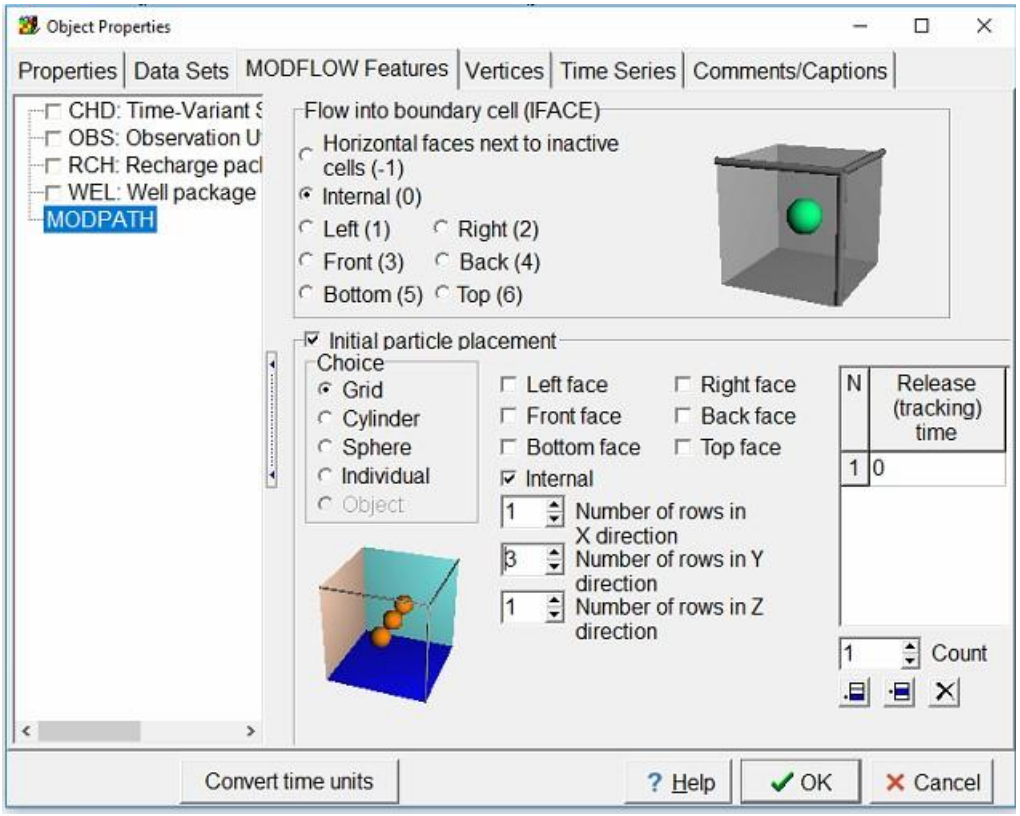

Figure 24. Windows allowing you to define the number of particles and their distribution within the cell.